

Bistability and Phase Synchronisation in Coupled Quantum Systems

Matthew Jessop



University of
Nottingham

UK | CHINA | MALAYSIA

Thesis submitted to the University of Nottingham
for the degree of Doctor of Philosophy

25 August 2020

“Coffee’s ready.”

- Numerous sources

Supervisors: Prof. Andrew Armour and Dr. Weibin Li

Examiners: Dr. Alexander Balanov
Dr. Beatriz Olmos Sanchez

Submitted: 25 August 2020

Examined: 12 November 2020

Final version: 15 February 2021

Abstract

In this work, we investigate novel phase synchronisation features that occur in bistable oscillators, explored with trapped ions and oscillator-only systems, as well as in networks of spin-1 oscillators of varying size and geometry. We begin with two coupled trapped ions each driven by a two-quanta gain process whose dynamical states heavily influence the emergent relative phase preference. Large gain rates produce limit-cycle states where photon numbers can become large with relative phase distributions that are π -periodic with peaks at 0 and π , as extensively discussed in the literature. When the gain rate is low, however, the oscillators have very low photon occupation numbers which produces π -periodic distributions with peaks at $\frac{\pi}{2}$ and $\frac{3\pi}{2}$. We find bistability between these limiting cases with a coexistence of limit-cycle and low-occupation states where the relative phase distribution can have $\frac{\pi}{2}$ -periodicity. These results reveal that synchronisation manifests differently in quantum oscillators outside of the limit-cycle regime. Next, we investigate the origin of these features by proposing a minimal oscillator-only model that also exhibits bistability but with reduced complexity. Our model of two 321 oscillators is purely dissipative, with a two-photon gain balanced by single- and three-photon loss processes. Perturbation theory reveals that the values of $\frac{\pi}{2}$ and $\frac{3\pi}{2}$ are due to the form of the number distribution that is produced by the two-quanta gain, unseen in thermal and van der Pol oscillators. Moving away from exploring bistability, we turn our attention to synchronisation in spin-1 oscillators which allows for the simulation of large networks. We derive an analytic form of the relative phase distribution of two spin-1 oscillators in a network that depends on only two complex values. The size and geometry of the network greatly affects the strength and form of synchronisation in the system. A strengthening of the synchronisation between next-nearest neighbours, compared to neighbours, is observed in chain and ring networks of three and four spins.

Acknowledgements

Foremost, I would like to thank Andrew Armour and Weibin Li, whose support and guidance was invaluable. It was an absolute pleasure being a part of the Condensed Matter Theory group at the University of Nottingham; every lecture and meeting was inspirational.

A huge thank you to my work colleagues- no, work *friends*. The countless coffees, lunches, pints, in-jokes, holiday-conferences, wine nights, lake walks, and coffees have made the past four years a truly unforgettable time.

I would also like to thank my family for always being supportive and feigning interest in theoretical physics.

Contents

List of Figures	vii
1 Introduction	1
1.1 The Outline of the Thesis	3
2 Synchronising oscillators	6
2.1 Synchronisation	6
2.1.1 Classical Synchronisation	7
2.1.2 Quantum Synchronisation	10
2.2 The van der Pol oscillator	15
2.2.1 The classical van der Pol oscillator	16
2.2.2 The quantum van der Pol oscillator	18
2.3 Summary	24
3 Quantum Synchronisation in Trapped Ion Systems	25
3.1 Introduction	25
3.2 Spin-oscillator model	26
3.2.1 Trapped ions	26
3.2.2 Two-phonon driving	27
3.2.3 Two oscillators	28
3.3 Bistability of a single oscillator	29

3.3.1	Numerical results	29
3.3.2	Mean field theory	32
3.3.3	Linear stability analysis of mean field solutions	34
3.4	Synchronisation of coupled oscillators	35
3.4.1	Relative phase distribution	35
3.4.2	Mean field theory for high driving	39
3.4.3	Asymmetrically coupled oscillators	41
3.4.4	Strong coupling	42
3.4.5	Spin covariance	44
3.5	Conclusion	45
4	321 Oscillator	47
4.1	Model	48
4.2	Steady state properties	51
4.2.1	Overview	51
4.2.2	Mean-field theory	52
	Least terms variant	53
	Normal ordered variant	54
4.3	Phase diagram	55
4.3.1	Peak at origin	57
4.3.2	Bistability contrast	59
4.4	Dynamics	61
4.4.1	Metastability	61
4.4.2	Quantum jump trajectories	63
4.5	Synchronisation of two coupled 321 oscillators	64
4.6	Conclusion	69

5 Synchronisation in spin-1 networks	71
5.1 The spin-1 oscillator	72
5.1.1 The smallest limit-cycle	73
5.2 Coupled spin-1 oscillators	76
5.2.1 Coupling geometries	76
5.2.2 Husimi-Q relative phase distribution	77
5.3 Spin-1 networks	80
5.3.1 Two oscillators	81
5.3.2 Three oscillators	86
5.3.3 Larger networks	91
5.4 Conclusion	97
6 Summary	99
Appendices	101
A Two-phonon resonant driving	101
B Perturbation theory for coupled 321 oscillators	102
B.1 General Method	102
B.2 Low Occupation-Number Regime	104
C Phase diffusion of a 321 oscillator	105
D Analytic form of spin-1 relative phase distribution	109
Bibliography	110

List of Figures

2.1	Original drawing by Christiaan Huygens of two pendulum clocks with a common support.	8
2.2	(a) The observed frequency difference of two coupled oscillators against the difference in natural frequencies. The region of frequency locking (b) depends on the strength of the coupling between oscillators.	9
2.3	The position x of two synchronised pendula (red and blue) as they oscillate in time t . The relative phase, $\phi = \varphi_1 - \varphi_2$, of two synchronised oscillators can lock to any value, for example (a) $\phi = 0.6\pi$. Two notable cases are that of (b) in-phase $\varphi_1 = \varphi_2$ and (c) anti-phase $\varphi_1 = \varphi_2 + \pi$ synchronisation.	10
2.4	An illustrative example of the relative phase distribution $P(\phi)$. Unsynchronised oscillators and produce (red line) a flat, uniform relative phase distribution with value $\frac{1}{2\pi}$. Two synchronised limit-cycle oscillators produce (blue line) a distribution with peaks indicating a relative phase preference of 0 and π	12

2.5	Multiple trajectories of the classical vdP oscillator showing (a) different initial conditions reaching the same limit-cycle, (b) the effect of the nonlinearity strength on the shape of the limit-cycle, and (c) the effect of the drive-damp ratio on the amplitude of the circular limit-cycle of the weakly nonlinear vdP oscillator.	17
2.6	The Wigner distribution of steady states of the QvdP oscillator (and trajectories of a classical analogue): (a) the ground state $ 0\rangle\langle 0 $, (b) the quantum regime limit-cycle, and (c) the classical regime limit-cycle.	22
3.1	(a) The two-phonon resonance transition induced by a driving laser of strength Ω that couples the n phonon ground state with the $n + 2$ phonon excited state. (b) Two identical harmonic oscillators with frequency ω_0 are driven at a strength Ω , cooled at a rate κ , undergo spontaneous emission at a rate γ , and are linearly coupled with strength J	27

- 3.2 (a) Phonon occupation probabilities P_n . As the driving strength Ω/Ω_c is increased, the oscillator transitions from a non-lasing state, to a bistable state, and finally to a lasing state. The P_n distribution consequently has different forms with a single sharp peak at $n = 0$ for low driving, a single, Gaussian peak at $n > 0$ for high driving, and coexistence of both at intermediate driving. Average phonon number $\langle \hat{n} \rangle$ from the numerical (dotted) and mean-field (solid) calculation are shown; the mean-field calculation indicates that the mean phonon number jumps from zero (not shown in the figure) to a non-zero value at the critical driving Ω_c . (b) The second moment μ_2 (solid blue, Eq. 3.7) and Mandel-Q parameter Q (dashed red, Eq. 3.6) are seen to rise significantly in the bistable region, where there are 2 coexisting peaks in P_n (shaded region). Here $\kappa/\gamma = 0.05$. 30
- 3.3 The Wigner distribution plotted as a function of the real and imaginary parts of the complex amplitude α for the phonons of a single oscillator at (a) low driving ($\Omega/\Omega_c = 0.2$), showing a non-lasing state, (b) critical driving ($\Omega/\Omega_c = 1.16$), showing a bistability in the phonon number, and (c) high driving ($\Omega/\Omega_c = 6$), showing a limit-cycle state (with $\kappa/\gamma = 0.15$). 31

3.4 (a) The relative phase distribution $2\pi P(\phi)$ for two coupled oscillators for a range of driving strengths spanning a range that includes the bistability (with $J/\gamma = 0.03$, $\kappa/\gamma = 0.15$). (b) The visibility V (black solid), the dominant Fourier coefficient F_2 (orange dashed), and the second relevant Fourier coefficient F_4 (cyan dotted) which has a small positive value. (c) The relative phase distributions for low ($\Omega = 0.7\Omega_c$, red dotted), intermediate ($\Omega = 0.815\Omega_c$, black solid), and high ($\Omega = 0.9\Omega_c$, blue dashed) driving. These driving strengths are highlighted in the panel above with a red square, black circle, and blue triangle, respectively. Also included is the relative phase distribution for two asymmetrically driven oscillators (see Sec. 3.4.3, magenta dash-dot), with $\Omega_1/\Omega_c = 0.5$ and $\Omega_2/\Omega_c = 2$ 37

3.5 The Wigner distributions for one of the oscillators with extremely low driving strength ($\Omega = 0.1\Omega_c$) obtained using (a) the full density matrix $\hat{\rho}$, (b) the excited state projection $\langle e, e | \hat{\rho} | e, e \rangle$, and (c) the ground state projection $\langle g, g | \hat{\rho} | g, g \rangle$ 39

3.6 (a) Phonon state occupation probabilities for low (red squares), bistable (black circles), and high (blue triangles) driving of the strongly coupled oscillators, where $\kappa/\gamma = 0.15$, $J/\gamma = 0.5$. (b) The relative phase distribution, $P(\phi)$ for a range of driving strengths spanning the bistability. (c) The relative phase distribution for low driving (red dotted), intermediate driving (black solid), and high driving (blue dashed). (d) The visibility V (black solid), F_2 Fourier coefficient (orange dashed), F_4 (cyan dotted), the spin correlation $C_{xx} = C(\sigma_1^x, \sigma_2^x)$ (magenta dash-dot). 43

- 4.1 (a) The three dissipative processes of the oscillator: two-phonon gain, single-phonon loss, and three-phonon loss, at rates κ_2 , κ_1 , and κ_3 , respectively. (b) Steady state properties as a function of κ_1/κ_2 for fixed $\kappa_3 = \kappa_2 \times 10^{-2}$. The colour scale shows the phonon-number distribution P_n (for $n > 0$), with the average phonon number $\langle n \rangle$ calculated numerically (white line), location of the peak in P_n away from $n = 0$ where it exists (black line), and the mean-field prediction n_+ (grey diamonds), superposed. Large phonon number states are occupied when the gain is sufficiently large (black cross), the fixed point state is predominantly occupied if the loss dominates (black circle), and a bimodal distribution appears in an intermediate region (black star). Also shown is the second moment $\mu_{(2)}$ (magenta line). The corresponding Wigner functions, $W(\alpha_r, \alpha_i)$, are for (c) limit-cycle ($\kappa_1/\kappa_2 = 10^{0.5}$), (d) bistability ($\kappa_1/\kappa_2 = 10^{1.25}$) and (e) fixed point ($\kappa_1/\kappa_2 = 10^2$). 49

- 4.2 Steady state behaviour of (a) the second moment $\mu_{(2)}$ and (b) average occupation number $\langle n \rangle$ overlaid with boundaries between the fixed point (FP), limit-cycle (LC), and bistable (B) regimes obtained by analysing the peaks in the radial Wigner distribution $W(r = |\alpha|)$. The FP-B boundary (upper dashed curve) agrees well with the appearance of the stable nonzero mean field solution, n_+ (full line). The LC-B boundary is shown using two different approaches: the dotted line indicates where the peak at the origin of the Wigner function disappears entirely, whilst the (lower) dashed line indicates the edge of a bistable region in which the Wigner peak at the origin remains *non-negligible* in size. The second moment is maximal within the bistable region where the corresponding LC contains a large occupation number (i.e. $\kappa_2 \gg \kappa_3$), elsewhere it is rather smooth. The average phonon number distribution $\langle n \rangle$ is largest deep within the LC regime (red), and lowest for the fixed point regions (white), but does not provide any direct indication of bistability. 56

- 4.3 Steady state phase diagram with the contrast of the bistability with a log scale and a series of contours at $10^{-[18:2]}$. The white regions indicate Wigner functions with only a single maximum, for example; (blue cross) a fixed-point (ci) has a single peak at $r = 0$ and (green cross) a limit-cycle (ciii) has a single peak at $r \geq 0$. The sign of (b) the second derivative of the Wigner distribution at $r = 0$ is used to determine if there is a maximum at the origin; i.e. a stable, $n_0 = 0$ solution ($\kappa_3 = \kappa_2 \times 10^{-1.5}$) and the locus where $W''|_{r=0} = 0$ is shown with the dotted line. The contrast is shown (red cross) for a strong bistability (cii) with a contrast of $C \approx 10^{-2}$. The solid black line shows the mean-field boundary. 60
- 4.4 (a) The slowest timescales τ_k of the oscillator for $k = 0, 1, 2$ with $\kappa_3 = \kappa_2 \times 10^{-2}$ and (b) the metastability M plotted on a logarithmic scale. The phase boundaries obtained using Wigner functions (dashed lines) and the mean field calculation (full line) are shown. . 62
- 4.5 Reproduced from Jessop et al. [53]. Sample quantum trajectories for each of the oscillator states illustrating the frequency of the different jump processes for (top) limit-cycle ($\kappa_1 = \kappa_2 \times 10^{1/2}$), (middle) bistable ($\kappa_1 = \kappa_2 \times 10^{5/4}$), and (bottom) fixed-point ($\kappa_1 = \kappa_2 \times 10^{7/4}$) states (with $\kappa_3 = \kappa_2 \times 10^{-7/4}$ throughout). The individual jump processes involving one-phonon loss (rate κ_1), two-phonon gain (rate κ_2), and three-phonon loss (rate κ_3) are indicated. The bistable oscillator can be seen to flip intermittently between LC-like and FP-like behaviour. In the FP state, the one-phonon loss jumps occur in pairs soon after each two-phonon gain jump (see magnified portion of the lower panel). 64

- 4.6 (a) The predominantly π -periodic relative phase distribution of the two-oscillator system with weak coherent coupling ($J/\kappa_2 = 10^{-2}$) and three-phonon loss $\kappa_3 = \kappa_2 \times 10^{-1}$, spanning the three motional states (FP, B, and LC) calculated with perturbation theory. Weak single-phonon loss ($\kappa_1 < \kappa_2$) produces the case of coupled limit-cycles and has peaks at 0 and π . As the single-phonon loss rate is increased, the pattern vanishes then reappears with peaks at $\frac{\pi}{2}$ and $\frac{3\pi}{2}$. Very strong single-phonon loss ($\kappa_1 \gg \kappa_2$) suppresses synchronisation. (b) The dominant Fourier coefficient F_2 (red) that accounts for the π -periodic form and whose sign determines the peak position. The fourth Fourier coefficient F_4 (blue) is the next largest, though is negligible in comparison for all parameter regimes except for the region in which $F_2 \approx 0$ where a four-peak, $\frac{\pi}{2}$ -periodic distribution can be observed. 65
- 4.7 (a) F_2/J^2 and (b) F_4/J^4 , the two most dominant Fourier coefficients of the relative phase distribution scaled with coupling strength (Eq. 3.23) showing the parameter regimes that have a π -periodic form where positive F_2 (red) produces peaks at 0 and π and negative F_2 produces peaks at $\frac{\pi}{2}$ and $\frac{3\pi}{2}$. When F_2 switches from positive to negative, it travels through zero and the small but nonzero F_4 becomes the dominant term producing a $\frac{\pi}{2}$ -periodic relative phase distribution with peaks at 0, $\frac{\pi}{2}$, π , and $\frac{3\pi}{2}$ 66

5.1 The Husimi-Q function acting as a phase portrait of the (a) $|-\rangle\langle-|$, (b) $|0\rangle\langle 0|$, and (c) $|+\rangle\langle+|$ states represented using the Winkel tripele earth projection. For $\hat{\rho} = |0\rangle\langle 0|$, it takes the form in Eq. 5.3 showing a φ independence and a maximal value of $\theta = \frac{\pi}{2}$. (d) The dissipative processes (see Eq. 5.5) that drive our spin-1 oscillator from the extremal states, $|+\rangle$ and $|-\rangle$, to the limit-cycle state $|0\rangle$, at rates γ^d and γ^g , respectively. 74

5.2 (a) A schematic showing the chain, ring, and all-to-all geometries possible with a network of N subsystems, and (b) corresponding coupling matrix. 77

5.3 (a) Relative phase distributions (scaled with visibility) of two weakly coupled ($\epsilon = 0.1$) spin-1 oscillators. (b) The visibility (Eq. 2.3) of distributions for a range of coupling strengths ϵ . (c) Husimi-Q functions of both oscillators with (ci) $R_1 = R_2 = 1$, (cii) $R_1 = R_2 = 10$, and (ciii) $R_1 = R_2^{-1} = 10$ which correspond to the curves in (a) and (b) in solid black, dashed blue, and dotted red, respectively. 78

5.4 The nonzero Fourier coefficients (a) A_{12}^i and (b) B_{12}^r that determine the relative phase distribution of two weakly coupled ($\epsilon = 0.1$), spin-1 oscillators. (c) The relative phase distributions corresponding to the parameters indicated by a black cross ($R_1 = R_2 = 1$), blue plus ($R_1 = R_2 = 10$), and red star ($R_1 = 10, R_2 = 1$). (d) The logarithmic negativity (Eq. 2.6) acting as an entanglement witness and (e) the limit-cycle deformation measure Eq. 5.6 with contours at $p_{max} = 0.1$ (black, also shown on other figures), 0.01 (grey), and 0.001 (white). (f) For the identical oscillator case ($R = R_1 = R_2$), the synchronisation strength (B_{12}^r red) and entanglement Eq. 2.6 (blue) are shown to appear before the limit-cycle deformation Eq. 5.6 (black) is large. The strongly deformed regime $p_{max} \geq 0.1$ is highlighted in grey. 82

5.5 Two coupled spin-1 oscillators with the second dissipation ratio fixed to $R_2 = 1$. The nonzero Fourier coefficients (a) A_{12}^i and (b) B_{12}^r that determine the relative phase distribution in Eq. 5.18. (c) The entanglement (logarithmic negativity) and (d) limit-cycle deformation measures are also included. All figures have the contour of 10% deformation in black. 84

5.6 (a) The only nonzero Fourier coefficient B_{12}^r of the relative phase distribution Eq. 5.19 of two identical spin-1 oscillators, with common oscillator ratio $R = R_1 = R_2$ coherently coupled with strength ϵ . (b) The logarithmic negativity (entanglement witness) showing some correspondence with the emergence of synchronisation, though certainly not identical. The solid line indicates the 10% limit-cycle deformation contour (Eq. 5.6). 86

- 5.7 The (a) all-to-all (or ring), and (b) chain geometries of the three spin-1 oscillator network. The coloured lines indicate which of the oscillators are directly coupled by the interaction Hamiltonian in Eq. 5.9. The only nonzero terms in the coupling matrix are (a) the upper triangle ($\epsilon_{12} = \epsilon_{23} = \epsilon_{13} = \epsilon$) or (b) the first off diagonal ($\epsilon_{12} = \epsilon_{23} = \epsilon$). 87
- 5.8 The nonzero Fourier coefficients (a) $A_{12}^r = A_{23}^r = A_{13}^r$ and (b) $B_{12}^r = B_{23}^r = B_{13}^r$ of the relative phase distribution Eq. 5.20 between any two spin-1 oscillators in a three spin-1, all-to-all (or ring) network with common dissipation ratios R and coupling strengths ϵ . (c) Example relative phase distributions for parameters given by (black solid curve) star, (red dashed curve) plus, and (blue dotted curve) star. Also shown is (d) the logarithmic negativity Eq. 2.6 which predicts entanglement when $E_N > 0 \forall \epsilon, R$ and (e) the limit-cycle deformation Eq. 5.6 with contour at 0.1. 89
- 5.9 Three spin-1, chain coupled network. The nonzero Fourier coefficients (a) $A_{12}^i = -A_{23}^i$, (b) $B_{12}^r = B_{23}^r$, (c) A_{13}^i , (d) B_{13}^r . (e) Shows example relative phase distributions (black solid curve) P_{12} , (red dashed curve) P_{23} , and (blue dotted curve) P_{13} of two spin-1 oscillators with common dissipation ratios R and coupling strengths ϵ with parameters indicated with (ei) a cross, (eii) a star, and (eiii) a plus. The entanglement (Eq. 2.6) between (fi) nearest neighbours $E_N^{12} = E_N^{23}$, and (fii) chain ends E_N^{13} , along with (fiii) the largest limit-cycle deformation in the network (Eq. 5.6) with contour at 0.1. 90

5.10 Schematic of an $N = 4$ network configured with (a) all-to-all, (b) ring, or (c) chain geometry. The coloured lines indicate which oscillators are directly coupled; just the red lines for the chain, add the blue line for the ring, and finally include the green lines for the all-to-all. 91

5.11 The only unique, nonzero Fourier components (a) $A_{j,k} = A_{12}$ and (b) $B_{j,k} = B_{12}$ for the four spin-1, all-to-all network. Each pair of oscillators has the same relative phase distribution, Eq. 5.23, with peaks at either $\phi = 0$ or at 0 and π , depending on which component dominates. Also shown are (c) the logarithmic negativity and (d) limit-cycle deformation with contour at 0.1. 92

5.12 The four spin-1, ring coupled network has a relative phase distribution between two neighbouring oscillators (Eq. 5.24) with nonzero Fourier coefficients (a) A_{12}^r and (b) B_{12}^r . Between next-nearest neighbours, the relative phase distribution is given by Eq. 5.25 with (c) A_{13}^r and (d) B_{13}^r 93

5.13 Four spin-1, chain coupled network. There are many nonzero Fourier components corresponding to many different relative phase distributions P_{jk} in Eq. 5.15. 94

5.14 Five spin-1, all-to-all coupled network. Any two oscillators have identical relative phase distributions (Eq. 5.23) with peaks at either 0 or 0 and π , depending on which of the two nonzero components, (a) A_{12}^r or (b) B_{12}^r , dominates. 95

5.15	Relative phase distributions for the five spin-1 ring network, between two neighbouring oscillators have the form Eq. 5.24 with (a) A_{12}^r and (b) B_{12}^r . Next-nearest neighbours have a different distribution of Eq. 5.25 with (c) A_{13}^r and (d) B_{13}^r	96
5.16	The maximum magnitude Fourier coefficient A_{jk} or B_{jk} of (blue) the nearest neighbours, $k = j + 1$, and (red) next-nearest neighbours, $k = j + 2$, for networks of N spin-1 oscillators in (a) all-to-all, (b) ring, and (c) chain geometries.	97

Chapter 1

Introduction

Synchronisation has been studied for centuries; from pendulum clocks on a beam that would tick in unison, to the simultaneous rhythms found in swarms of insects [8, 38, 83, 86], it is ubiquitous in nature. The tendency of coupled systems to develop identical frequencies and phases has been studied in seemingly every scientific field. Notable examples include biology, chemistry, ecology, sociology, economics, and, of course, countless branches of physics.

Theoretical physics has changed a lot since the 17th century, when Christiaan Huygens developed the earliest understanding of synchronisation [51]. Research advanced beyond the classical world, and interest turned to exploring the phenomenon in the realm of quantum mechanics [77]. Over the years, a host of theoretical methods and measures have been developed, all with the goal of understanding the similarities and differences between quantum synchronisation and its classical analogue [38, 73]. More recently, advancements in experimental techniques have even led to groups observing this phenomenon among systems such as trapped ions [21, 49].

Theoretical studies of quantum synchronisation often focus on a quantum version of the van der Pol oscillator [61, 65, 66, 118]. This model is chosen because the

quantum features can be directly compared to the widely studied, and better understood, classical model [115]. Synchronisation in other quantum systems that go beyond this simple model, however, remains relatively unexplored. This thesis aims to theoretically investigate quantum synchronisation in models such as trapped ions and simpler oscillator models that are driven to bistability, as well as spin-1 networks with varying size and geometry.

We began our work exploring trapped ions with a two-quanta gain process that can be driven to a bistable state. We found interesting synchronisation features in the system of two coupled bistable ions, and, from this, developed a useful measure based on a Fourier decomposition of the relative phase distribution. Though trapped ions are experimentally realisable, the full spin-oscillator model made analysis difficult and the origin of the interesting synchronisation features was unclear. To address this, we went on to develop a minimal oscillator-only model that was also capable of being driven to the bistable state: the 321 oscillator. Its mathematical simplicity allowed for the exploration of an extensive range of parameters which ultimately led to our understanding of the synchronisation regimes.

This simplification of the trapped ion model to the 321 oscillator inspired a further simplification which allowed us to model many coupled oscillators; our research moved from considering two subsystems based on harmonic oscillators to networks of up to 5 spin-1 oscillators. With the previous systems, modelling more than two oscillators was only possible with extremely high powered computers. With spin-1 oscillators, however, the much smaller state space allowed for a larger number of systems to be explored. We went on to extend our relative phase distribution deconstruction to an exact description that revealed synchronisation features that strongly depend on the network size and geometry. Understanding how quantum synchronisation emerges in networks of spin-1 oscillators is vital for the advance-

ment of fields such as quantum information and quantum technology. This thesis details features of quantum synchronisation in a range of novel contexts that are not present in the “standard” models in the literature.

1.1 The Outline of the Thesis

Chapter 2 introduces the focus of the thesis: synchronisation, describes the widely studied van der Pol oscillator, and outlines recent results in the field. Synchronisation is discussed, first, in a classical context, beginning with the observation of simultaneously ticking clocks by Christiaan Huygens. Then, quantum synchronisation is explained, where phase-locking is observed in quantum systems through analysis of measures such as relative phase distributions and quasiprobabilities. Next, an important model often used to study synchronisation, the van der Pol oscillator, is introduced in both its classical and quantum forms. This provides the reader with the features of synchronisation that are typically found in the literature that will be used to contrast our results found in bistable oscillator models.

Chapter 3 begins by describing a spin-oscillator model that can be realised in trapped ions, a novel two-phonon gain process, and the exchange process used to couple two oscillators. While previous work has utilised this ion model, the inclusion of the two-phonon drive results in a bistability in the phonon state of the ion. This bistability is shown to appear in the steady state numerics of the system and is predicted with mean field theory. Next, synchronisation features of two coupled ions are explored with a relative phase distribution that is decomposed into Fourier coefficients. Familiar results are found for ions driven to limit-cycle states and a mean field argument explains this. Weakly driven oscillators, however, produce entirely different synchronisation patterns, similar to what occurs

in asymmetrically driven ions. Finally, a method for resolving the phonon state of the ions by simply counting emitted photons is discussed.

Chapter 4 seeks to describe, in detail, exactly how the new synchronisation patterns form. A minimal model, the 321 oscillator, is proposed which simplifies the system whilst reproducing the bistable state with another two-phonon gain process. The steady state and dynamical properties of the 321 oscillator are explored both numerically and with mean field theory to produce a phase diagram of the different possible states of the system. A thorough discussion on the definition of the bistable state is included along with a proposed measure, the bistability contrast, to quantify bistableness. Next, dynamical properties of the bistable state are explored, including a metastability prediction from eigenvalue analysis as well as observed intermittency in quantum jump simulations. Finally, the synchronisation features of two coupled 321 oscillators are discussed, again with the relative phase distribution decomposed into Fourier coefficients. A perturbative calculation is then carried out in the weak driving regime, and the interesting synchronisation patterns are explained to be due to the phonon distribution whose particular form is a direct result of the two-phonon gain.

Chapter 5 makes a departure from bistability and instead focuses on minimising the size of the oscillator state space so that the number of oscillators can be increased beyond two. A spin-1 model is introduced; equivalent to a heavily truncated van der Pol oscillator with only three energy levels. A simple Lindblad master equation is introduced that gives rise to a limit-cycle in the spin-1 oscillator which is visualised with the Husimi-Q function. The formalism of the network geometry is described for any number of oscillators, specifically considering all-to-all, ring, and chain networks. Next, an exact measure that describes the relative phase distribution is derived from the Husimi-Q function which consists

of only two complex values. This novel approach allows for easy visualisation of the phase locking phenomena in a range of parameter regimes, initially shown for the two-spin network with varying oscillator driving-damping ratios and coupling strengths. Analysis of larger networks reveals different synchronisation phenomena for different network sizes and geometries. Specifically, a strengthening of the synchronisation is seen between next nearest neighbours compared to nearest neighbours in networks of 3 or more oscillators.

The two-phonon driving of the spin-oscillator model, and subsequent synchronisation patterns of the bistable state in Chapter 3, as well as the entirety of Chapters 4 and 5 are from original research undertaken in collaboration with Andrew Armour and Weibin Li. The key results in Chapter 4 are published in [53]. The results in Chapters 3 and 5 are currently being prepared for future publications.

Chapter 2

Synchronising oscillators

In this Chapter, we will discuss the background material necessary to understand quantum synchronisation in novel coupled oscillator models. First, in Sec. 2.1, we explain synchronisation in the context of classical systems (Sec. 2.1.1), starting with Christiaan Huygens and his pendulum clocks. We then explore how the concept changes in the quantum regime (Sec. 2.1.2) and introduce the specific measures that are used to study synchronisation. In Sec. 2.2, we introduce an important model system, the van der Pol oscillator, and describe the self-sustained oscillations that develop in it. We start by discussing the classical regime (Sec. 2.2.1) before going on to describe synchronisation in a quantum version of the van der Pol oscillator (Sec. 2.2.2).

2.1 Synchronisation

Synchronisation is ubiquitous in nature and emerges in countless fields of study [5, 83, 86]. In biological research, there has been significant interest in describing synchronisation in neuronal networks of the brain [18, 19, 26, 32, 44, 48, 108, 111] as well as in networks of cells that mediate the heartbeat [74, 113], insulin secretion

in the pancreas [59, 107], and processes in the small intestine [28]. Synchronisation is also observed in the behaviour exhibited by swarms of fireflies [15, 16] and crickets [117], various circadian rhythms [33, 86], as well as in animal populations [12, 91]. Even sociological and economic systems synchronise, from opinions forming in crowds [90] and rhythmically tapping at musical performances [95], to the chaos of the stock market [82], and the flow of global trade [36].

In physics, research into synchronisation began classically [86], with pendulum clocks [51], organ pipes [94], and radios [4, 115]. Research eventually evolved to explore how synchronisation changes for classical systems operating in the quantum regime, such as the maser [25] as well as van der Pol [61, 118], Kerr [66], and optomechanical [68, 118, 120] oscillators. Different physical systems are proposed to explore quantum synchronisation in individual oscillators and complex many-body realisations [31, 92, 99, 124]. Examples of this are atomic ensembles [122, 126], trapped ions [49, 61], and superconducting circuits [78], as well as precisely engineered nonlinear oscillators [30, 80, 81, 119]. This list of studies is far from exhaustive and merely highlights interesting examples whilst reminding the reader that synchronisation is a universal phenomenon and not confined to the precisely engineered pendula or the specific models explored in this work.

2.1.1 Classical Synchronisation

In the 17th century, Christiaan Huygens noticed a peculiar effect when working on naval pendulum clocks [51]; two pendula with a common support would develop perfectly identical swings (Fig. 2.1).

“It is quite worth noting that when we suspend two clocks so constructed from two hooks imbedded in the same wooden beam, the motions of each pendulum in

opposite swings were so much in agreement that they never receded the least bit from each other and the sound of each was always heard simultaneously.” [123]

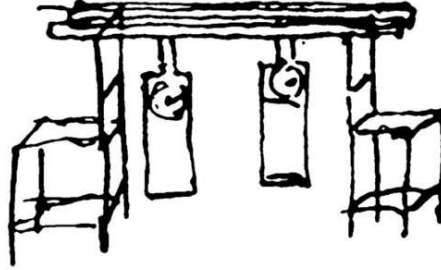


Figure 2.1: Original drawing by Christiaan Huygens of two pendulum clocks with a common support. Taken from [51].

This was the first time synchronisation had been described in a scientific way. Synchronisation is an effect that adjusts the motion of oscillating objects that interact weakly. Although the clocks seemed isolated, Huygens realised that they must have been interacting somehow. The pendula were passing imperceptible amounts of energy through the common support and so became coupled. Though this coupling was extremely weak, it still had the ability to alter the oscillatory motion of the pendula. Figure 2.2a shows schematically that, for similar oscillators with small detuning $\Delta f = f_1 - f_2 \approx 0$ between the oscillator frequencies $f_{1,2}$, the observed frequencies $F_{1,2}$ become identical, $\Delta F = F_1 - F_2 = 0$. This is known as *frequency locking* and is the first indication of synchronisation in a system.

In this scenario, the frequency locking is facilitated by a coupling interaction that is incredibly weak when compared to the the processes that govern the dynamics of the individual oscillators. This was possible because the clocks were designed to have identical frequencies, though engineering limitations at the time would have produced discrepancies. Synchronisation is not, however, found only in this near-identical oscillator regime. Instead, even oscillators with natural frequencies that differ considerably can synchronise provided that the interaction is sufficiently strong.

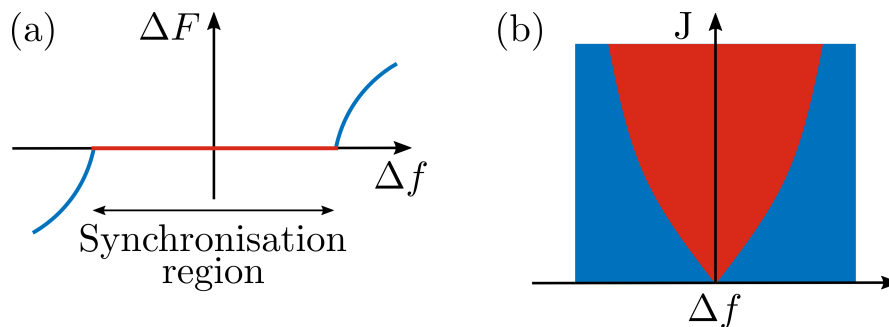


Figure 2.2: (a) The observed frequency difference of two coupled oscillators, $\Delta F = F_1 - F_2$, against the difference in frequency of the oscillators if they were uncoupled, $\Delta f = f_1 - f_2$, in arbitrary units. The synchronisation region shows how different the natural frequencies can be, whilst still facilitating synchronisation $\Delta F = 0$. (b) The strength of the coupling between oscillators J , increases the width of the synchronisation region, shown here with the Arnold tongue [6].

The regimes of synchronisation can be visualised with the Arnold tongue [6] shown in Fig. 2.2b, where the red region indicates the frequency locked regime, $\Delta F = 0$, for a range of coupling strength J and natural frequency differences Δf .

Frequency locking accounts for the identical frequencies of the oscillators, but this does not explain why Huygens heard simultaneous ‘ticks’. For this to occur, both pendula must reach the same point in its motion (in this case, the point where the mechanism audibly clicks) at the same time. This reveals that oscillators can synchronise in different ways and we distinguish between these types of synchronisation by introducing the concept of phase. The phase of a simple harmonic oscillator φ grows uniformly with time and increases by 2π after each oscillation. If the relative phase of any two oscillators $\phi = \varphi_1 - \varphi_2$ becomes fixed, the system exhibits synchronisation in the form of *phase locking*, as shown in Fig. 2.3a.

If both pendula swing in a similar manner, as depicted in Fig. 2.3b, the oscillators would be described as being *in phase* with relative phase $\phi = 0$. Oscillators that oppose each other’s motion, shown in Figure 2.3c, are described as *anti-phase* with $\phi = \pi$. Huygens observed anti-phase synchronisation between his clocks, but a

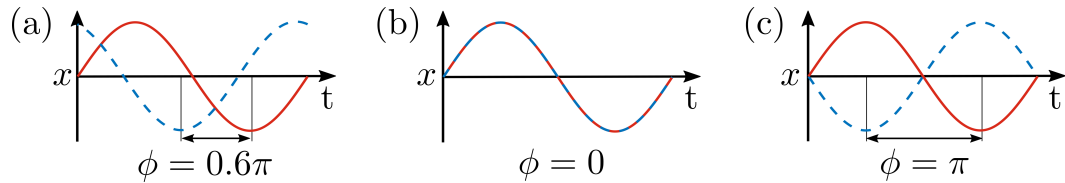


Figure 2.3: The position x of two synchronised pendula (red and blue) as they oscillate in time t . The relative phase, $\phi = \varphi_1 - \varphi_2$, of two synchronised oscillators can lock to any value, for example (a) $\phi = 0.6\pi$. Two notable cases are that of (b) in-phase $\varphi_1 = \varphi_2$ and (c) anti-phase $\varphi_1 = \varphi_2 + \pi$ synchronisation.

range of relative phase relations are possible. This rather simple model of two coupled pendula with locked phases has been generalised to explain a huge variety of different systems.

It is important to note that synchronisation only occurs in oscillating systems that are driven and damped in such a way that their motion has a well-defined amplitude and free phase; systems of this kind are known as limit-cycle oscillators [86]. We will now turn our attention to how we describe synchronisation in quantum systems.

2.1.2 Quantum Synchronisation

Though classical synchronisation has been understood for some time, the systematic study of synchronisation in quantum oscillators, outside the regime where semiclassical approximations work well [23], is quite recent [61, 68, 72, 73, 118, 125]. This research has already uncovered many differences to the classical studies of synchronisation [25, 61, 65, 66]. In quantum systems, motional energy of an oscillator can be quantised into phonons and the position and velocity are described by operators; phase, however, is not so easily translated. Many have attempted to describe a quantum phase operator $\hat{\phi}$ and the endeavour proved to be rather problematic. A historical review by Nieto [77] is particularly interesting along with a review of the mathematical formalism by Gerry and Knight [38].

Initial attempts by Dirac [29] assumed a hermitian $\hat{\phi}$ which was impossible to achieve when considering the lower-bounded number operator and periodicity requirement of an angle operator [38, 77]. Later, this problem was addressed by Pegg and Barnett with a truncated Hilbert space with (non-physical) negative number states [10, 11]. In a different approach, Susskind and Glogover proposed an exponential operator whose eigenstates were phase states [110] $|\varphi\rangle = \sum_{n=0}^{\infty} e^{in\varphi} |n\rangle$ (with $|n\rangle$ a Fock state) that could be used to define a phase distribution [2] $P(\varphi) = \frac{1}{2\pi} \langle \varphi | \hat{\rho} | \varphi \rangle$ where $\hat{\rho}$ is the density matrix. This approach is particularly fruitful as it produces phase distributions, also found with the Pegg-Barnett approach [85], whilst avoiding the problem of defining a phase operator altogether. Quantum mechanics introduces Heisenberg uncertainty to a system [46, 47], leading to a broadening of the relative phase, similar to a classical system with noise [86]. Because of this, it is natural to seek to characterise synchronisation in quantum systems with something like a probability distribution. There are a number of distributions that can be used to study synchronisation; we will focus on the Wigner function and the relative phase distribution. Classical systems of coupled limit-cycle oscillators typically relax to (or, in some cases, oscillate near) discrete relative phase values [58, 86]. The relative phase distribution of two quantum oscillators [9, 11, 25, 49, 66, 69] is defined by;

$$P(\phi) = \iint_0^{2\pi} d\varphi_1 d\varphi_2 \delta(\varphi_1 - \varphi_2 - \phi) \langle \varphi_1, \varphi_2 | \hat{\rho} | \varphi_1, \varphi_2 \rangle \quad (2.1)$$

$$= \frac{1}{2\pi} + \frac{1}{\pi} \operatorname{Re} \left[\sum_{k=1}^{\infty} e^{ik\phi} \sum_{n,m=0}^{\infty} \langle n+k, m | \hat{\rho} | n, m+k \rangle \right], \quad (2.2)$$

where $\phi = \varphi_1 - \varphi_2$ is the relative phase, $|\varphi_j\rangle = (2\pi)^{-1/2} \sum_{n=0}^{\infty} e^{i\varphi_j n} |n\rangle$ is a phase state of oscillator j , and $|n, m\rangle$ are the number states with n (m) phonons for oscillator 1 (2).

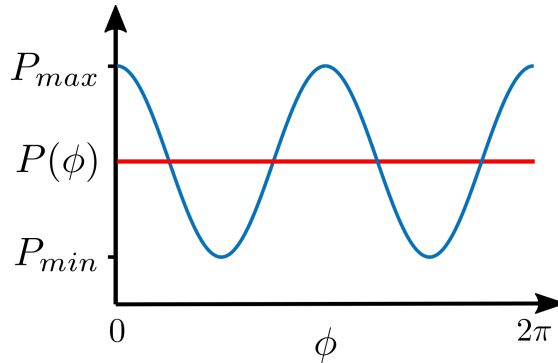


Figure 2.4: An illustrative example of the relative phase distribution $P(\phi)$. Unsynchronised oscillators produce (red line) a flat, uniform relative phase distribution with value $\frac{1}{2\pi}$. Two synchronised limit-cycle oscillators produce (blue line) a distribution with peaks indicating a relative phase preference of 0 and π .

If two oscillators are unsynchronised, their phases are independent of each other and so exhibit a uniform relative phase distribution, $P(\phi) = \frac{1}{2\pi}$, as shown in red in Fig. 2.4. The relative phase of two coupled limit-cycle oscillators is illustrated in blue with a continuous distribution with maxima at 0 and π corresponding to in-phase and anti-phase synchronisation respectively [25, 61, 104]. In fact, any non-flat $P(\phi)$ reveals a connection between the phases and is thus an indication that the oscillators are synchronised. A useful measure of synchronisation strength based on the relative phase distribution (Eq. 2.2) is the visibility [49, 66];

$$V = \frac{(P_{max} - P_{min})}{(P_{max} + P_{min})} \quad (2.3)$$

which quantifies the deviation from a flat distribution.

A particularly fruitful method of describing a quantum state is achieved by expressing the density matrix in terms of functions of coherent states [41];

$$|\alpha\rangle = e^{-\frac{|\alpha|^2}{2}} \sum_{n=0}^{\infty} \frac{\alpha^n}{\sqrt{n!}} |n\rangle \quad (2.4)$$

that have the property $\hat{a}|\alpha\rangle = \alpha|\alpha\rangle$. The coherent state is a state of minimum

uncertainty and can be thought of as the state with dynamics most similar to a classical state.

Expressing the density matrix of a quantum oscillator system in terms of a complex phase variable α allows us to visualise the oscillator state in phase-space with quasi-probability functions such as the Husimi-Q and Wigner distributions [35, 50, 101]. Here, we will focus on the Wigner function as it has been used to investigate phase synchronisation in coupled oscillator systems [61].

The Wigner function is a joint distribution for any canonically conjugate variables, such as position x and momentum p ,

$$W(x, p) = \frac{1}{2\pi\hbar} \int_{-\infty}^{\infty} dx \left\langle q + \frac{x}{2} \left| \hat{\rho} \right| q - \frac{x}{2} \right\rangle e^{\frac{ipx}{\hbar}} \quad (2.5)$$

where $|q \pm \frac{x}{2}\rangle$ are the eigenstates of the position operator [38]. In what follows, we will consider it in the form $W(\alpha)$ (sometimes written as $W(\alpha, \alpha^*)$ or $W(\alpha_r, \alpha_i)$) and will visualise states of the system $\hat{\rho}$ in phase-space with the real and imaginary parts of the complex amplitude $\alpha = x + ip$. A different change of variables $\alpha = re^{i\varphi}$ and an integration over amplitude (r) reveals something similar to a phase (φ) distribution $P_W(\varphi) = \int_0^\infty dr rW(r, \varphi)$. Furthermore, the Wigner function can be calculated for a system of coupled oscillators to explore synchronisation. A two-mode Wigner distribution can be calculated, $W(\alpha_1, \alpha_2)$ with complex amplitudes α_1 and α_2 corresponding to two subsystems. Then, by integrating out both amplitudes as well as the sum of the phases $\varphi_1 + \varphi_2$, something like a relative phase distribution can be obtained $P_W(\varphi_1 - \varphi_2)$. Such a two-oscillator Wigner function has been used to show that phase locking can be more robust in quantum models than in classical models [61].

It is important to note that, as these distributions are calculated from the Wigner function (a *quasi*probability distribution that can become negative in quantum

systems [61]), it cannot be considered as a true phase distribution and may behave differently to classical intuition in the quantum regime. Because of this, we will use the relative phase distribution calculated from phase states (in Eq. 2.2) to quantify synchronisation in what follows. Additionally, the Wigner function will be used to categorise the dynamical states of individual oscillators, as we discuss in Sec. 2.2.2.

Many researchers have sought to understand the connection between synchronisation and entanglement in coupled quantum oscillator systems [3, 25, 34, 60, 63, 72, 73, 100, 101, 118]. The most commonly used measure for entanglement in the driven and damped systems that display synchronisation is the logarithmic negativity [116];

$$E_N(\hat{\rho}) = \log_2 \|\hat{\rho}^{TA}\|_1, \quad (2.6)$$

where $\hat{\rho}^{TA}$ is the partial transpose (of a subsystem A) and $\|\square\|_1$ denotes the trace norm. However, this measure should not be thought of as a quantifier of entanglement strength, but instead merely a witness; if a bipartite system is entangled, the logarithmic negativity will be nonzero.

Recent studies of coupled quantum systems have shown that synchronisation and entanglement can both exist in the same system [60] and that synchronisation can be a witness to entanglement survival in networks of oscillators [72]. Though the two phenomena may be linked, they seem to describe different aspects of the synchronised system [25]. However, systems displaying synchronisation can be devoid of entanglement entirely [3, 73]. In continuous variable systems [14], calculating the phase and amplitude quadratures from canonical position and momentum operators has also been used to indicate synchronisation [63, 73].

Additionally, entropic measures can reveal interesting features of coupled systems, such as the mutual information $I(\hat{\rho}) = S(\hat{\rho}_1) + S(\hat{\rho}_2) - S(\hat{\rho})$, where the von Neuman

entropy $S(\hat{\rho}) = -\text{Tr}[\hat{\rho} \log \hat{\rho}]$ is calculated for the system $\hat{\rho}$ and the partially traced subsystems $\hat{\rho}_j = \text{Tr}_j[\hat{\rho}]$ for $j = 1, 2$. Mutual information can indicate synchronisation in any bipartite system such as coupled van der Pol oscillators and qubits in cavities [3, 25]. Much like the logarithmic negativity, the mutual information cannot be used as a synchronisation measure [40].

Much of the work on quantum synchronisation has involved simple models such as the quantum van der Pol (QvdP) oscillator [61, 65, 66, 118] and spin-1 particles [57, 100, 101]. However, a range of other systems have also been considered including atomic ensembles [122, 126] and optomechanical systems [68, 73, 120]. Significant efforts have also been devoted to proposing ways in which the behaviour could be probed in experiment using systems such as trapped ions [49, 61] or superconducting circuits [78].

Depending on the system, quantum noise has been shown to suppress synchronisation [68] or to strengthen it [61]. Quantum anharmonic oscillators have more phase locking and frequency locking resonances [65] than classical counterparts. Conversely, introducing quantisation to energy levels can completely suppress phase locking leading to a synchronisation blockade [66]. Our research will focus on oscillators that are not too dissimilar to the quantum van der Pol oscillator. We will now explain the details of this paradigmatic model, starting with its classical origins.

2.2 The van der Pol oscillator

Harmonic oscillators have played a pivotal role in the history of theoretical physics, from the classical experiments of Galileo's pendula [87] to the birth of quantum mechanics with Planck's black body radiation [88]. The most commonly studied oscillator model that displays a limit-cycle, is the van der Pol (vdP) oscillator [4,

115] due to its relative simplicity.

2.2.1 The classical van der Pol oscillator

The van der Pol (vdP) oscillator was devised by Balthasar van der Pol [4, 115] while working on the first radios to explain the self-sustained oscillation of the current of a triode circuit. An oscillator can be described as self-sustained if it maintains a periodic motion with a stable amplitude and frequency. Physically, this implies that it has access to a supply of energy as well as being subject to damping. The mathematical simplicity of the vdP oscillator and the complexity of the behaviours it exhibits has made it the paradigmatic nonlinear oscillator to study self-sustained oscillations, also known as limit-cycles states [1, 86].

In this section, we will describe various methods that have been used to study the vdP oscillator which we will later apply and adapt to our novel oscillator models. The classical equation of motion for the van der Pol oscillator takes the form;

$$\ddot{x} + x + \tilde{\epsilon} \left(-\tilde{R} + x^2 \right) \dot{x} = 0, \quad (2.7)$$

where we work in dimensionless units of time with $\square = \frac{d}{d\tau} = \frac{1}{\omega_0} \frac{d}{dt}$ and ω_0 is the natural frequency. This describes a harmonic oscillator with nonlinearity introduced with strength $\tilde{\epsilon} > 0$; note that $\tilde{\epsilon} = 0$ recovers the equation for simple harmonic motion. The vdP oscillator has a negative damping (or dissipative driving) term $(-\dot{x})$, and a nonlinear damping term $(x^2\dot{x})$, with relative strengths controlled by $\tilde{R} > 0$. Regimes in which the driving or damping term is dominant can therefore be reached with $\tilde{R} > 1$ or $1/\tilde{R} > 1$ respectively.

The vdP oscillator can be simplified by considering the weakly nonlinear regime $\tilde{\epsilon} \ll 1$. It is then useful to change our coordinate system to a complex amplitude $\alpha = x + i\dot{x}$, such that $x = \text{Re}(\alpha) = \alpha_r$ and $\dot{x} = \text{Im}(\alpha) = \alpha_i$. Moving to a rotating

frame using $\tilde{\alpha} = \alpha e^{i\tau}$ and dropping rapidly oscillating terms, which can be applied in the limit of weak nonlinearities, means that Eq. 2.7 becomes

$$\dot{\tilde{\alpha}} \approx \tilde{\alpha} \epsilon \left(\frac{R}{2} - |\alpha|^2 \right), \quad (2.8)$$

where we have rescaled $\epsilon = \tilde{\epsilon}/8$ and $R = 8\tilde{R}$.

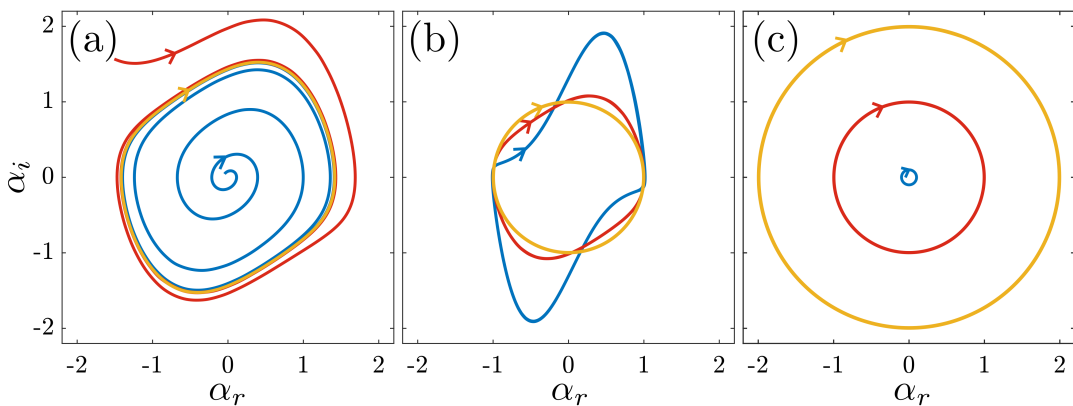


Figure 2.5: Multiple trajectories of the classical vdP oscillator (Eq. 2.8) with a range of (a) initial conditions $\alpha(t=0)$, (b) nonlinearity strength ϵ , and (c) drive-damp ratio R . (a) All trajectories eventually reach the same limit-cycle (yellow curve) with fixed $\epsilon = 0.1$ and $R = 4$. (b) The nonlinearity acts to deform the limit-cycle from the circular orbit of a simple harmonic oscillator ($\epsilon = 1, 0.2$, and 10^{-5} shown in blue, red, and yellow, respectively, with $R = 2$). (c) In the weakly nonlinear regime (e.g. $\epsilon = 10^{-5}$), the limit-cycle is circular with radius determined by $\sqrt{R/2} = 0.1, 1$, and 2 shown in blue, red, and yellow, respectively.

Solving Eq. 2.8 numerically reveals the trajectories in Fig. 2.5a that eventually reach a closed loop, regardless of the initial conditions and therefore indicate self-sustained oscillations. This oscillatory path (the yellow curve in Fig. 2.5a) is the limit-cycle of the vdP oscillator and has different forms depending on the parameters in Eq. 2.8. Changing the strength of the nonlinearity ϵ affects the shape of the limit-cycle, shown in Fig. 2.5b. As the nonlinearity is decreased, the limit-cycle becomes almost circular and the amplitude of the oscillation $|\alpha|$

becomes stationary. In the weakly nonlinear limit, the amplitude depends only on the ratio R , as shown in Fig. 2.5c; stronger driving (or weaker damping) leads to larger amplitude limit-cycles.

To explain the system analytically in the weakly nonlinear regime, we explicitly write the complex amplitude as $\tilde{\alpha} = Ae^{i\varphi}$ such that Eq. 2.8 becomes equations of motion for the (real) amplitude and phase;

$$\dot{A} = \frac{1}{2A} (\dot{\alpha}\alpha^* + \alpha\dot{\alpha}^*) = \epsilon A \left(\frac{R}{2} - A^2 \right) \quad (2.9)$$

$$\dot{\varphi} = \frac{i}{2A^2} (\dot{\alpha}\alpha^* - \alpha\dot{\alpha}^*) = -1. \quad (2.10)$$

In the steady state, $\dot{A} = 0$, Eq. 2.9 produces a stable solution of

$$A = \sqrt{\frac{R}{2}}, \quad (2.11)$$

which predicts the trajectories in Fig. 2.5c. Note that there is a zero amplitude solution, $A = 0$, but it is unstable and therefore any perturbation grows. The phase in Eq. 2.10 simply winds around at the natural frequency ($\frac{d\varphi}{dt} = \omega_0\dot{\varphi} = -\omega_0$), similar to the trajectories in Fig. 2.5c.

This approximation accurately describes the dynamics found numerically in the classical limit; the vdP model with weak nonlinearity is a self sustained oscillator with a limit-cycle of fixed amplitude and freely oscillating phase.

2.2.2 The quantum van der Pol oscillator

This section will explain how to find a quantum counterpart to the van der Pol oscillator [61, 65, 66, 118]. The criteria of a quantum van der Pol (QvdP) oscillator is that it reproduces the same results as the classical van der Pol oscillator when in the classical limit.

In open quantum systems, a Lindbladian [64] (or Gorini-Kossakowski-Sudarshan-Lindblad [43]) master equation is often used to describe the evolution of a density matrix in the presence of an environment with which a system can exchange energy. Such master equations can be derived from microscopic models [17].

Consider the Lindblad master equation describing two processes of energy exchange between an oscillator and its surroundings: single-phonon gain, or dissipative drive, and two-phonon loss, or nonlinear damping, at rates κ_1 and κ_2 , respectively [35, 61, 64]

$$\dot{\hat{\rho}} = -i [\hat{H}, \hat{\rho}] + 2\kappa_1 D[\hat{a}^\dagger](\hat{\rho}) + 2\kappa_2 D[\hat{a}^2](\hat{\rho}), \quad (2.12)$$

where natural units ($\hbar = 1$) will be used throughout. Details of how this dynamics could be realised in a trapped ion system are given in [61]. The commutator in Eq. 2.12 describes coherent evolution of the system under the Hamiltonian $\hat{H} = \omega_0 \hat{a}^\dagger \hat{a}$ where ω_0 is the natural frequency of the oscillator. The remaining terms are Lindblad dissipators of the form $D[\hat{C}](\hat{\rho}) = \hat{C} \hat{\rho} \hat{C}^\dagger - \frac{1}{2} \{ \hat{C}^\dagger \hat{C}, \hat{\rho} \}$ where \hat{C} is the jump operator. These processes describe the dissipative terms in the evolution of the QvdP oscillator and correspond to the negative damping, or driving (with \hat{a}^\dagger), and nonlinear damping (with \hat{a}^2) terms of the vdP. The bosonic creation and annihilation operators \hat{a} and \hat{a}^\dagger [13, 112] act on the Fock states $|n\rangle$

$$\hat{a} |n\rangle = \sqrt{n} |n-1\rangle \quad (2.13)$$

$$\hat{a}^\dagger |n\rangle = \sqrt{n+1} |n+1\rangle \quad (2.14)$$

and obey the commutation relation $[\hat{a}, \hat{a}^\dagger] = 1$. The Fock state $|n\rangle$ describes an eigenstate of the number operator \hat{n} with n phonons and $|0\rangle$ is the vacuum state. To establish whether the system produces the same results in the classical limit,

we can employ a mean field (MF) theory approach to probe the large amplitude regime [1, 24, 96]. Since we are working in the Schrödinger picture, we can find an equation of motion for expectation values of operators with $\frac{d}{dt}\langle\hat{C}\rangle = \text{Tr}[\hat{C}\dot{\hat{\rho}}]$. From Eq. 2.12, we find for the expectation value of operator \hat{a}

$$\frac{d}{dt}\langle\hat{a}\rangle = \kappa_1\langle\hat{a}\rangle - 2\kappa_2\langle\hat{a}^\dagger\hat{a}^2\rangle \quad (2.15)$$

In this case, the MF theory neglects correlations between operators and so in the classical limit, we can replace the operator \hat{a} with the complex amplitude α so Eq. 2.15 becomes

$$\frac{d\alpha}{d\tau} = \frac{\kappa_1}{\omega_0}\alpha \left(1 - \frac{2\kappa_2}{\kappa_1}|\alpha|^2\right) \quad (2.16)$$

where we have used $\tau = \omega_0 t$. This clearly maps onto Eq. 2.8 (with $\frac{\kappa_1}{\omega_0} \rightarrow \frac{\bar{\epsilon}R}{2}$ and $\frac{2\kappa_2}{\kappa_1} = \frac{1}{R}$) and therefore, the mean field limit of the QvdP oscillator (Eq. 2.12) recovers the classical vdP oscillator in Sec. 2.2.1 with amplitude given by Eq. 2.11. It is important to note that, in the QvdP model, the amplitude of the limit-cycle corresponds to the square root of the average phonon number of the system $\langle\hat{n}\rangle = \langle\hat{a}^\dagger\hat{a}\rangle = |\alpha|^2 = A^2$. Thus, in the steady state, where $\dot{\hat{\rho}} = 0$ and therefore $\frac{d\alpha}{d\tau} = 0$, the phonon number of the QvdP oscillator in the classical limit is given by

$$\langle\hat{n}\rangle_{cl} \approx \frac{\kappa_1}{2\kappa_2}, \quad (2.17)$$

which from the correspondence principle, can be expected to apply when $\kappa_1 \gg \kappa_2$ so that $\langle\hat{n}\rangle \gg 1$.

Outside of the classical regime (for example $\kappa_2 \gg \kappa_1$), the QvdP oscillator retains its limit-cycle and the phase remains free (the steady state of $\hat{\rho}$ has no off-diagonals in the number-state basis). In the extreme quantum limit, the QvdP oscillator

can be truncated to the two lowest levels, and the steady state becomes [61]

$$\hat{\rho} \xrightarrow[\kappa_2 \rightarrow \infty]{} \frac{1}{3} (2 |0\rangle\langle 0| + |1\rangle\langle 1|). \quad (2.18)$$

The features of the limit-cycle are most clearly revealed by calculating the Wigner distribution of the steady state density matrix of a QvdP oscillator. An undriven QvdP oscillator, $\kappa_1 = 0$, stays in the ground state $|0\rangle\langle 0|$ with steady state Wigner distribution shown in Fig. 2.6a. This is equivalent to the zero amplitude solution $A = 0$ of the classical vdP in Sec. 2.2.1 with $R = 0$, a classical trajectory that reaches this state is shown in black.

The Wigner distribution of Eq. 2.18 is shown in Fig. 2.6b revealing the existence of a limit-cycle in the quantum limit of the QvdP oscillator: the peak in the Wigner function occurs along a ring with fixed amplitude. The large amplitude limit-cycle (see Eq. 2.17) of the strongly driven QvdP oscillator is shown in Fig. 2.6c with the corresponding classical limit-cycle overlaid (see Eq. 2.11). Very similar states are found above threshold for a conventional laser and we will refer to states like that shown in Fig. 2.6b as lasing states in the following. Neither the classical nor quantum calculations predict a preferred phase.

In the semiclassical regime, where the density matrix is tightly peaked around a large (but finite) average phonon occupation number [25, 105], the strength of phase synchronisation is found to be determined by a rate of phase diffusion in the individual oscillators, with slower phase diffusion leading to stronger phase preferences [25]. This is very similar to what is found in the case of noisy classical oscillators [86]. In the following, we show how a phase diffusion rate can be derived for the QvdP system in the semiclassical regime.

The phase distribution for a single oscillator (Eq. 2.2) can be written in the

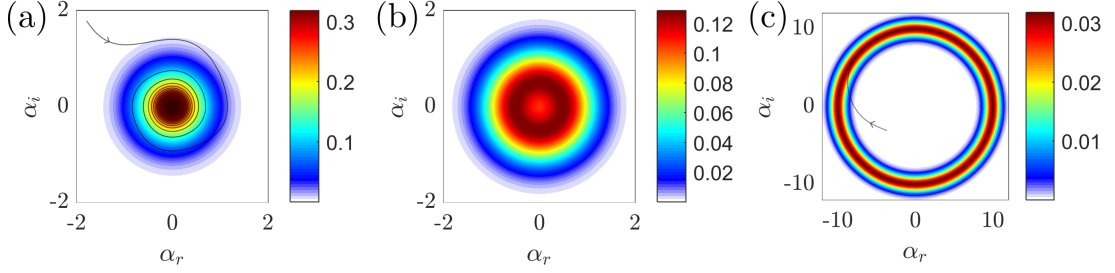


Figure 2.6: The Wigner distribution of steady states of the QvdP oscillator: (a) the ground state $|0\rangle\langle 0|$ reached with zero driving, (b) the limit-cycle in the quantum limit (i.e. lasing state) given by Eq. 2.18, and (c) a large amplitude limit-cycle in the classical regime. Trajectories of a classical analogue system are overlaid showing (a) a decay to zero amplitude and (c) the large amplitude limit-cycle with parameters chosen to match the quantum results.

form [11, 25, 38]

$$P(\varphi) = \frac{1}{2\pi} + \frac{1}{\pi} \operatorname{Re} \left[\sum_{k=1}^{\infty} e^{ik\varphi} \Phi^{(k)} \right] \quad (2.19)$$

with

$$\Phi^{(k)} = \sum_n \rho_n^{(k)} \quad (2.20)$$

where $\rho_n^{(k)} = \langle n | \hat{\rho} | n+k \rangle$. Although the behaviour is in general quite complex, we obtain a simple approximate description in the semiclassical limit. The steady state properties of this system are found by exploiting the purely dissipative form of Eq. 2.12 in the interaction picture such that the dynamics of the diagonal and off-diagonal parts of the density operator are decoupled [102, 105]. Therefore, the master equation can be rewritten as a coupled set of equations

$$\dot{\rho}_n^{(k)} = -G_n^{(k)} \rho_n^{(k)} + A_{n-1}^{(k)} \rho_{n-1}^{(k)} + B_{n+2}^{(k)} \rho_{n+2}^{(k)} \quad (2.21)$$

where

$$G_n^{(k)} = \kappa_1 [(n+1) + (n+k+1)] + \kappa_2 [n(n-1) + (n+k)(n+k-1)] \quad (2.22)$$

$$A_n^{(k)} = 2\kappa_1 \sqrt{(n+1)(n+k+1)} = 2\kappa_1 n \sqrt{1 + \frac{1}{n}} \sqrt{1 + \frac{k+1}{n}}, \quad (2.23)$$

$$B_n^{(k)} = 2\kappa_2 \sqrt{n(n-1)(n+k)(n+k-1)} \quad (2.24)$$

$$= 2\kappa_2 n^2 \sqrt{1 - \frac{1}{n}} \sqrt{1 + \frac{k}{n}} \sqrt{1 + \frac{k-1}{n}}. \quad (2.25)$$

In the semiclassical limit, i.e. the gain process is dominant over the loss $\kappa_1 \gg \kappa_2$, the phonon number saturates to a large value (see Eq. 2.17) so that we can expand the square roots in orders of $\frac{1}{n}$

$$A_n^{(k)} = \kappa_1 \left[2n + (k+2) - \frac{k^2}{4n} + \frac{(k+2)k^2}{8n^2} + \mathcal{O}(n^{-3}) \right] \quad (2.26)$$

$$B_n^{(k)} = \kappa_2 \left[2n^2 + 2(k-1)n - k + \frac{k^4 - 2k^3 + k^2 - 2k + 1}{8n^2} + \mathcal{O}(n^{-3}) \right] \quad (2.27)$$

We make the assumption that $n \rightarrow \langle \hat{n} \rangle = \frac{\kappa_1}{2\kappa_2}$ with the number distribution strongly peaked about this value and neglect small quantities [25, 103, 105] which leads to a simplified equation of motion for $\Phi^{(k)}$ in Eq. 2.20 through using Eq. 2.21

$$\dot{\Phi}^{(k)} = \sum_{n=0}^{\infty} [-G_n^{(k)} + A_n^{(k)} + B_n^{(k)}] \rho_n^{(k)} = \left[-\frac{3\kappa_2 k^2}{4} + \mathcal{O}(\langle \hat{n} \rangle^{-2}) \right] \Phi^{(k)}. \quad (2.28)$$

Therefore, to leading order, the relaxation timescale for the k^{th} component, $\Phi^{(k)}$, is simply proportional to $1/\kappa_2$. Finally, using the definition Eq. 2.19 and Eq. 2.28, we find that within this approximation, the phase distribution obeys a diffusion equation [25, 103]

$$\dot{P}(\varphi) = \frac{3\kappa_2}{4} \frac{\partial^2 P(\varphi)}{\partial \varphi^2}. \quad (2.29)$$

Hence, for the QvdP oscillator, increasing the phonon number by decreasing the damping rate κ_2 leads to slower diffusion of the phase and consequently synchronisation effects are strengthened [61]. Similar results are also obtained for the laser [105].

2.3 Summary

In this Chapter, we introduced the background material necessary to adapt a classical description of synchronisation to be applicable to quantum systems. We described the relevant concepts such as oscillation phase and amplitude as well as phase-space trajectories and limit-cycles. We also outlined specific synchronisation measures including the relative phase distribution, Wigner distribution, and visibility. Finally, we explained how to model quantum oscillators with phonon operators and a master equation as well as mean-field methods which are used to predict behaviour in classical limits.

Chapter 3

Quantum Synchronisation in Trapped Ion Systems

3.1 Introduction

In this chapter, we theoretically investigate quantum synchronisation in a system of two quantum harmonic oscillators, each coupled to a spin via a *two-phonon* resonant interaction. The two oscillators, which are linearly coupled to each other through a phonon exchange process, are cooled to the nonclassical, few phonon regime. We show that such a model can be realised in a trapped ion system where unprecedented control and accessible spin correlation measurements make it an ideal candidate.

We find that increasing the driving strength of an oscillator allows it to transition from a zero-phonon state to a lasing state via a *bistable* state. This bistability in the phonon distribution is found by solving the respective quantum master equation and via a mean field description. This is followed by an exploration of quantum synchronisation between two such oscillators that have been weakly coupled. The literature [49, 58, 61, 86] predicts that two oscillators driven to

lasing states synchronise trivially such that their relative phase distribution has peaks at 0 and π . However, we show that for our system, weakly driven and therefore *non-lasing* oscillators first develop a nontrivial phase relation with phase probability peaks at $\frac{\pi}{2}$ and $\frac{3\pi}{2}$. In the bistable region, the relative phase displays peaks at both integers and half-integers of π . We investigate the origins of such phase distributions through a variety of numerical and mean-field calculations.

Section 3.2 begins by introducing our coupled spin-oscillator model explaining the connection to trapped ion systems and describing the master equation we use to explore its properties, including the two-phonon resonance driving, dissipative processes and linear coupling. Then, we show that the oscillators can be driven to a bistable state in Sec. 3.3. In Sec. 3.4, we explore synchronisation between weakly and strongly coupled, bistable oscillators through features of the Fourier coefficients of the relative phase and reinforce the results with a mean field analysis. Finally, we summarise our results and propose possible future work in Sec. 3.5.

3.2 Spin-oscillator model

Our study is based on a spin-oscillator model using a quantum master equation in which the spins and phonons (vibrational quanta) of a quantum harmonic oscillator are driven via an anti-Jaynes-Cummings [45] type two-phonon process (see Fig. 3.1a).

3.2.1 Trapped ions

The coupled spin-oscillator system can be realised using cold trapped ions [21, 49] (Fig. 3.1b). Consider an ion which is tightly confined in a Paul trap such that the vibrational state is a ladder of evenly spaced energy levels typical of a harmonic

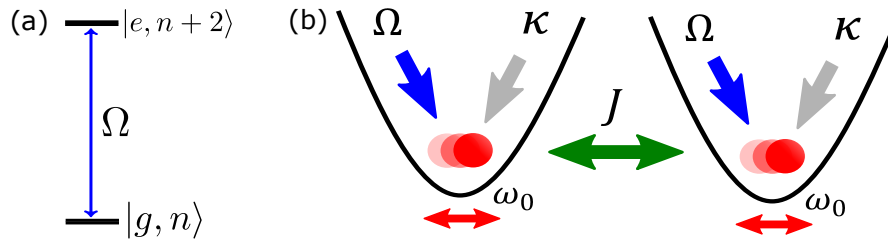


Figure 3.1: (a) The two-photon resonance transition induced by a driving laser of strength Ω that couples the n phonon ground state with the $n+2$ phonon excited state. (b) Two identical harmonic oscillators with frequency ω_0 are driven at a strength Ω , cooled at a rate κ , undergo spontaneous emission at a rate γ , and are linearly coupled with strength J .

potential. The vibrational term in the Hamiltonian is $\hat{H}_v = \omega_0 \hat{a}^\dagger \hat{a}$, where ω_0 is the trapping frequency. The electronic state of each charged ion can be modelled as a two-level system with a ground $|g\rangle$ and excited state $|e\rangle$. The electronic Hamiltonian is then $\hat{H}_e = \frac{\omega_e}{2} \hat{\sigma}^z$, where ω_e is the energy spacing and $\hat{\sigma}^z = 2\hat{\sigma}^+ \hat{\sigma}^- - 1$ is the Pauli spin matrix and $\hat{\sigma}^- = |g\rangle\langle e|$.

3.2.2 Two-phonon driving

The electronic and vibrational states of the ions are coupled (Fig. 3.1a) by a standing wave laser (see also [21]). The full Hamiltonian for the single ion, within a frame rotating at the laser frequency (using a unitary transformation of $\hat{U} = e^{-it\omega_l \hat{\sigma}^z/2}$), is found to be

$$\hat{H}_s = \omega_0 \hat{a}^\dagger \hat{a} + \frac{\Delta}{2} \hat{\sigma}^z + \frac{\tilde{\Omega}}{2} \cos \left[\eta (\hat{a}^\dagger + \hat{a}) + \chi \right] (\hat{\sigma}^+ + \hat{\sigma}^-) \quad (3.1)$$

where $\Delta = \omega_e - \omega_l$, $\tilde{\Omega}$ is the Rabi frequency set by the strength of the laser drive, and χ accounts for the phase of the laser at the position of the ion. The Lamb-Dicke parameter $\eta = k(2m\omega_0)^{-1/2}$ is defined for an ion of mass m in a trap of frequency ω_0 interacting with laser light of wavevector k . We explain in App. A

that a detuning of $\Delta = -2\omega_0$ and the rotating wave approximation allows us to reduce Eq. 3.1 to a two-phonon resonance Hamiltonian

$$\hat{H} = -\frac{\Omega}{4} \left[(\hat{a}^\dagger)^2 \hat{\sigma}^+ + \text{h.c.} \right], \quad (3.2)$$

where the driving strength has been rescaled $\Omega = \eta^2 \tilde{\Omega}$. Note that similar methods can produce a variety of different light-ion interactions, such as the single phonon resonance Hamiltonian [49].

3.2.3 Two oscillators

We now consider two identical oscillators, with the Hamiltonian of the j^{th} ($j = 1, 2$) spin-oscillator subsystem in the interaction picture given by,

$$\hat{H}_j = -\frac{\Omega}{4} \left[(\hat{a}_j^\dagger)^2 \hat{\sigma}_j^+ + \hat{a}_j^2 \hat{\sigma}_j^- \right], \quad (3.3)$$

where \hat{a}_j^\dagger (\hat{a}_j) and $\hat{\sigma}_j^+$ ($\hat{\sigma}_j^-$) are phonon creation (annihilation) and spin raising (lowering) operators of the j^{th} ion. The driving strength Ω is assumed to be equal for each spin-oscillator and couples the spin and phonon degrees of freedom as shown in Fig. 3.1a.

The ions are coupled via the Coulomb interaction [52] which, to lowest order, leads to an interaction between the phonons described by the Hamiltonian [49]

$$\hat{H}_c = J \left(\hat{a}_1^\dagger \hat{a}_2 + \hat{a}_2^\dagger \hat{a}_1 \right), \quad (3.4)$$

with coupling strength J . In addition, we take into account the dissipative processes of the spin and phonon; each spin undergoes spontaneous emission at a rate γ , and the phonons are cooled via an additional laser at a rate κ , which leads

to damping [21]. Combining the coherent and dissipative interactions (phonon damping due to the cooling laser and spontaneous emission from the excited electronic state at a rate γ), the dynamics of this coupled system is governed by a Lindblad master equation

$$\dot{\hat{\rho}} = -i [\hat{H}, \hat{\rho}] + \sum_j (\kappa \mathcal{L}[\hat{a}_j](\hat{\rho}) + \gamma \mathcal{L}[\hat{\sigma}_j^-](\hat{\rho})), \quad (3.5)$$

with the total Hamiltonian $\hat{H} = \sum_{j=1,2} \hat{H}_j + \hat{H}_c$.

3.3 Bistability of a single oscillator

Our work focuses on steady states of the system attained either through time evolving the master equation for a sufficiently long period with a numerical integration method [27] or, for a small number of phonons, by direct diagonalisation of the Lindbladian [75]. For convenience, we scale energy in units of γ and time with $1/\gamma$ in the numerical calculation. In a critical region of the driving strength, the phonon distribution of the oscillator exhibits a bistable configuration; a coexistence of a non-lasing and lasing state.

3.3.1 Numerical results

We start by characterising stationary states of individual oscillators through phonon probability distributions $P_n = \langle n | \tilde{\hat{\rho}} | n \rangle$ where $|n\rangle$ is the number state with n phonons and the reduced density matrix of the phonons is found by tracing over all possible spin states $\tilde{\hat{\rho}} = \text{Tr}_s[\hat{\rho}]$.

We explore the relationship of different driving strengths Ω on the phonon distribution P_n of the two-phonon driven oscillator in Fig. 3.2a. Without driving, the stationary state is the ground state of the oscillator. Weakly driven oscillators

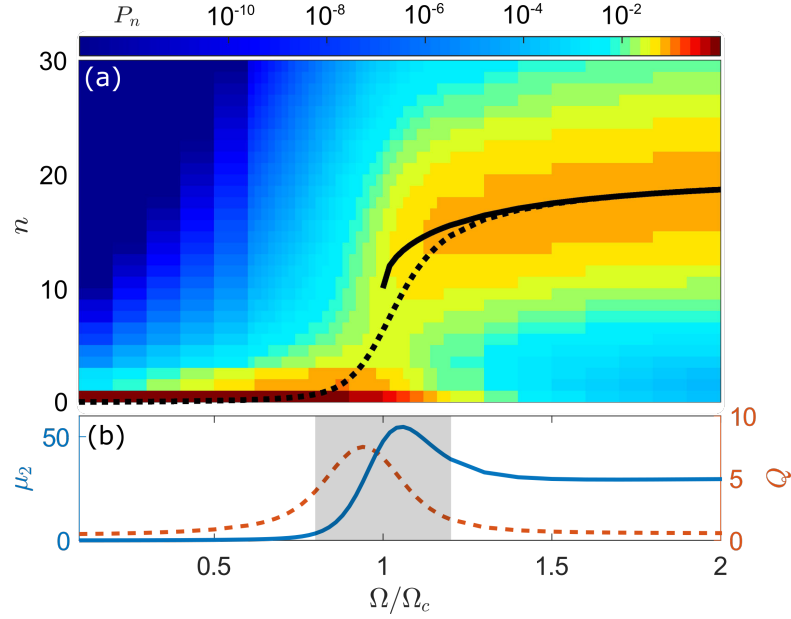


Figure 3.2: (a) Phonon occupation probabilities P_n . As the driving strength Ω/Ω_c is increased, the oscillator transitions from a non-lasing state, to a bistable state, and finally to a lasing state. The P_n distribution consequently has different forms with a single sharp peak at $n = 0$ for low driving, a single, Gaussian peak at $n > 0$ for high driving, and coexistence of both at intermediate driving. Average phonon number $\langle \hat{n} \rangle$ from the numerical (dotted) and mean-field (solid) calculation are shown; the mean-field calculation indicates that the mean phonon number jumps from zero (not shown in the figure) to a non-zero value at the critical driving Ω_c . (b) The second moment μ_2 (solid blue, Eq. 3.7) and Mandel-Q parameter Q (dashed red, Eq. 3.6) are seen to rise significantly in the bistable region, where there are 2 coexisting peaks in P_n (shaded region). Here $\kappa/\gamma = 0.05$.

remain near this state, with mean phonon number $\langle \hat{n} \rangle \approx 0$. For strong driving, the oscillator reaches a limit-cycle, i.e. the phonon lasing state [37, 55, 114]. In the crossover region, the two states coexist and a bistability emerges.

This change in the phonon distribution is accompanied by a similar change in the Wigner distributions, shown in Fig. 3.3. In the low (and zero) driving regime, the oscillator exhibits a non-lasing state and the Wigner distribution has a single peak at the centre (Fig. 3.3a). For the high driving, limit-cycle state, the distribution is a ring (Fig. 3.3c). The emergence of the bistability at intermediate driving strengths gives rise to both the central peak and an outer ring (Fig. 3.3b). It is

important to note that the bistability only appears for the two-phonon resonance, it is absent in cases of single-phonon resonance [49].

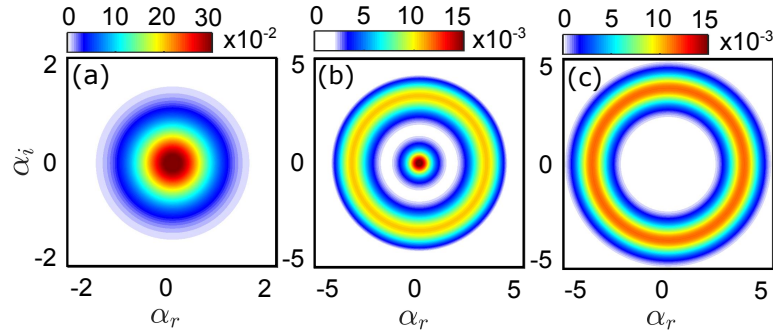


Figure 3.3: The Wigner distribution plotted as a function of the real and imaginary parts of the complex amplitude α for the phonons of a single oscillator at (a) low driving ($\Omega/\Omega_c = 0.2$), showing a non-lasing state, (b) critical driving ($\Omega/\Omega_c = 1.16$), showing a bistability in the phonon number, and (c) high driving ($\Omega/\Omega_c = 6$), showing a limit-cycle state (with $\kappa/\gamma = 0.15$).

We quantify the strength of the bistability with different measures such as simply counting maxima in the phonon distribution and Wigner distribution or more complicated statistical measures such as the Mandel-Q parameter or the second moment, as shown in Fig. 3.2b. The simplest, a search for P_n with two maxima, is shown as a shaded area and spans the transitional region. The Mandel-Q parameter,

$$Q = \frac{\langle \hat{n}^2 \rangle - \langle \hat{n} \rangle^2}{\langle \hat{n} \rangle} - 1, \quad (3.6)$$

which is plotted in dashed orange has a peak around the transitional region. A similar statistical quantity, the second moment,

$$\mu_2 = \langle \hat{n}^2 \rangle - \langle \hat{n} \rangle^2, \quad (3.7)$$

is also shown in solid blue and has a peak around Ω_c . Both of these measures can be used to quantify the departure of a distribution from Poissonian statistics as would occur if a bimodality appears.

3.3.2 Mean field theory

To understand how the system transitions from the zero-phonon number state to the limit-cycle state, we consider a mean field (MF) approach. The equations of motion that describe the expectation values of the system are calculated from the master equation, Eq. 3.5, as shown in Sec. 2.2.2 for the QvdP oscillator. For the trapped ion model, these are found to be

$$\frac{d}{dt}\langle\hat{n}\rangle = -\kappa\langle\hat{n}\rangle + \frac{i\Omega}{2}\left(\langle(\hat{a}^\dagger)^2\hat{\sigma}^+\rangle - \langle\hat{a}^2\hat{\sigma}^-\rangle\right), \quad (3.8)$$

$$\frac{d}{dt}\langle\hat{a}\rangle = -\frac{\kappa}{2}\langle\hat{a}\rangle + \frac{i\Omega}{2}\langle\hat{a}^\dagger\hat{\sigma}^+\rangle, \quad (3.9)$$

$$\frac{d}{dt}\langle\hat{\sigma}^-\rangle = -\frac{\gamma}{2}\langle\hat{\sigma}^-\rangle - \frac{i\Omega}{4}\langle(\hat{a}^\dagger)^2\hat{\sigma}^z\rangle, \quad (3.10)$$

$$\frac{d}{dt}\langle\hat{\sigma}^z\rangle = -2\gamma\langle\hat{\sigma}^+\hat{\sigma}^-\rangle + \frac{i\Omega}{2}\left(\langle(\hat{a}^\dagger)^2\hat{\sigma}^+\rangle - \langle\hat{a}^2\hat{\sigma}^-\rangle\right). \quad (3.11)$$

Transient dynamics of a system can be interesting to explore, but a lot can be understood by calculating the steady state of the system. This is achieved by taking $\dot{\rho} = 0$ equivalent to setting the left hand side of Eqs. 3.8-3.11 to zero. Solving these equations, we find the stationary solutions,

$$\langle\hat{n}\rangle = \frac{i\Omega}{2\kappa}\left(\langle(\hat{a}^\dagger)^2\hat{\sigma}^+\rangle - \langle\hat{a}^2\hat{\sigma}^-\rangle\right), \quad (3.12)$$

$$\langle\hat{a}\rangle = \frac{i\Omega}{\kappa}\langle\hat{a}^\dagger\hat{\sigma}^+\rangle, \quad (3.13)$$

$$\langle\hat{\sigma}^-\rangle = -\frac{i\Omega}{2\gamma}\langle(\hat{a}^\dagger)^2\hat{\sigma}^z\rangle, \quad (3.14)$$

$$\langle\hat{\sigma}^z\rangle = \frac{\kappa}{\gamma}\langle\hat{n}\rangle - 1. \quad (3.15)$$

We simplify these relations by factorising the expectation value of two operators via a mean field approximation, e.g. $\langle\hat{A}\hat{B}\rangle \approx \langle\hat{A}\rangle\langle\hat{B}\rangle$.

There is a trivial solution that follows immediately from Eq. 3.12 by considering

the case of $\langle \hat{\sigma}^- \rangle = 0$; the zero-phonon solution

$$\langle \hat{n} \rangle_0 = 0. \quad (3.16)$$

More solutions are found by substituting Eq. 3.15 and the complex conjugate of Eq. 3.13 into Eq. 3.14 to find

$$\begin{aligned} \langle \hat{\sigma}^- \rangle &= -\frac{i\Omega}{2\gamma} \langle \hat{a}^\dagger \rangle \langle \hat{a} \rangle^* \langle \hat{\sigma}^z \rangle, \\ &= -\frac{i\Omega}{2\gamma} \langle \hat{a}^\dagger \rangle \left(-\frac{i\Omega}{\kappa} \langle \hat{a} \rangle \langle \hat{\sigma}^- \rangle \right) \left(\frac{\kappa}{\gamma} \langle \hat{n} \rangle - 1 \right), \end{aligned} \quad (3.17)$$

where the star denotes the complex conjugate. Since this approach approximates $\langle \hat{n} \rangle = \langle \hat{a}^\dagger \hat{a} \rangle \approx \langle \hat{a}^\dagger \rangle \langle \hat{a} \rangle$, we can rewrite Eq. 3.17 as a quadratic equation

$$-\frac{\Omega^2}{2\gamma^2} \left[\langle \hat{n} \rangle^2 - \frac{\gamma}{\kappa} \langle \hat{n} \rangle + \frac{2\gamma^2}{\Omega^2} \right] \langle \hat{\sigma}^- \rangle = 0. \quad (3.18)$$

In the case of $\langle \hat{\sigma}^- \rangle \neq 0$, Eq. 3.18 leads to the quadratic

$$\langle \hat{n} \rangle^2 - \frac{\gamma}{\kappa} \langle \hat{n} \rangle + \frac{2\gamma^2}{\Omega^2} = 0 \quad (3.19)$$

with two non-zero solutions

$$\langle \hat{n} \rangle_\pm = \frac{\sqrt{2}\gamma}{\Omega_c} \left[1 \pm \sqrt{1 - \left(\frac{\Omega_c}{\Omega} \right)^2} \right], \quad (3.20)$$

where $\Omega_c = 2\sqrt{2}\kappa$ is the critical driving strength at which Eq. 3.20 becomes real, and therefore physical. We expect this result to be most accurate in the large phonon number regime, where the oscillator behaves rather classically. This regime is reached with large driving strengths $\Omega \gg \Omega_c$ such that Eq. 3.20 predicts

a nonzero phonon number of

$$\langle \hat{n} \rangle_{\text{cl}} = \frac{2\sqrt{2}\gamma}{\Omega_c} = \frac{\gamma}{\kappa}. \quad (3.21)$$

Comparing the mean field results with the numerics in Sec. 3.3.1 reveals that the peaks in the P_n distribution follows the mean field solutions $\langle \hat{n} \rangle_0$ and $\langle \hat{n} \rangle_+$ in both the low and high driving regimes, respectively (See Fig. 3.2). Furthermore, the bistable region coincides with the transition predicted by the critical driving strength Ω_c . The numerical results seem to avoid $\langle \hat{n} \rangle_-$ altogether; this is explained through linear stability analysis.

3.3.3 Linear stability analysis of mean field solutions

To understand which of the three mean field solutions are stable, linear stability analysis is used [71]. If a state is stable, a small perturbation will be countered by a decay back to the state, and if unstable, the perturbation will grow resulting in an evolution away from the state. We construct the Jacobian \mathcal{D} for Eq. 3.9, Eq. 3.10, and their complex conjugates,

$$\mathcal{D} = \begin{bmatrix} -\frac{\kappa}{2} & \frac{i\Omega}{2} \langle \hat{\sigma}^+ \rangle & 0 & \frac{i\Omega}{2} \langle \hat{a}^\dagger \rangle \\ -\frac{i\Omega}{2} \langle \hat{\sigma}^- \rangle & -\frac{\kappa}{2} & -\frac{i\Omega}{2} \langle \hat{a} \rangle & 0 \\ -\frac{i\Omega\kappa}{4\gamma} \langle (\hat{a}^\dagger)^3 \rangle & -\frac{i\Omega}{4} \left(\frac{3\kappa}{\gamma} \langle (\hat{a}^\dagger)^2 \hat{a} \rangle - 2 \langle \hat{a}^\dagger \rangle \right) & -\frac{\gamma}{2} & 0 \\ \frac{i\Omega}{4} \left(\frac{3\kappa}{\gamma} \langle \hat{a}^\dagger \hat{a}^2 \rangle - 2 \langle \hat{a} \rangle \right) & \frac{i\Omega\kappa}{4\gamma} \langle \hat{a}^3 \rangle & 0 & -\frac{\gamma}{2} \end{bmatrix}, \quad (3.22)$$

and evaluate its eigenvalues for each steady state; negative (positive) real parts of eigenvalues indicate stability (instability) (if $\text{Re}[\lambda_i] = 0$, higher order analysis is required). We find that $\langle \hat{n} \rangle_-$ is never stable, $\langle \hat{n} \rangle_0$ is always stable, and $\langle \hat{n} \rangle_+$ is stable for $\Omega \geq \Omega_c$; therefore, the mean field analysis predicts a bistability for

$\Omega \geq \Omega_c$. In contrast, the full master equation calculation (see Fig. 3.2) produces P_n distributions with two peaks, and therefore suggests the system is bistable, for a small range of $\Omega \approx \Omega_c$. Although the zero-phonon solution is always stable in the mean field calculation, increasing Ω drives the system to large phonon numbers and the peak at $n = 0$ disappears.

3.4 Synchronisation of coupled oscillators

Now that we have an understanding of the bistability found in the phonon state of the two-phonon resonantly driven spin-oscillator, we can begin to explore the synchronisation effects that emerge when two oscillators are coupled together by the Hamiltonian \hat{H}_c (Eq. 3.4).

A key finding of this work is that two coupled, bistable oscillators (Fig. 3.3b) display interesting and unusual behaviour in their relative phase distribution. In particular, the maximal values of the phase probability are centred at $\frac{\pi}{2}$ and $\frac{3\pi}{2}$ for very weak driving, and shift to 0 and π in the lasing regime. Additionally, all four peaks exist simultaneously in an intermediate region. This is in sharp contrast to monostable systems [49], where the phase preference at 0 and π in the lasing state appears immediately from the flat distribution of the undriven, non-lasing state.

3.4.1 Relative phase distribution

As discussed in Sec. 2.1.2, coupled limit-cycle oscillators typically display a preference for one or more relative phase values [58, 86]. The behaviour of the relative phase, $\phi = \varphi_1 - \varphi_2$, for the coupled spin-oscillator system is described by the

probability distribution [9, 11, 25, 49, 66, 69];

$$P(\phi) = \frac{1}{2\pi} + \frac{1}{\pi} \operatorname{Re} \left[\sum_{k=1}^{\infty} F_k e^{ik\phi} \right], \quad (3.23)$$

where

$$F_k = \operatorname{Re} \left[\sum_{n,m=0}^{\infty} \langle n+k, m | \tilde{\rho} | n, m+k \rangle \right] \quad (3.24)$$

are the Fourier coefficients, $\tilde{\rho} = \operatorname{Tr}_s[\hat{\rho}]$ is the reduced density matrix for the phonons of both oscillators after tracing out the spins, with phonon number states $|k, l\rangle$.

As discussed in Sec. 2.1.2, two unsynchronised oscillators exhibit a uniform relative phase distribution. Therefore, any non-flat $P(\phi)$ reveals a connection between the phases and is thus an indication that the oscillators are synchronised. The strength of the synchronisation is characterised by the magnitude of the deviation from a flat distribution with the visibility defined in Eq. 2.3.

We start with a situation where the two oscillators are weakly coupled. In this regime, the properties of the P_n distribution will only be slightly affected by the presence of the coupling. Figure 3.4a shows the relative phase distribution $P(\phi)$ for weakly coupled ($J/\gamma = 0.03$) oscillators for a range of driving strengths around the bistability transition. It is clear that the phase distribution is almost completely flat in the limit of small Ω . When we increase the driving, non-trivial structures appear in the phase distribution. These structures are often smooth curves with two peaks that correspond to the system developing two phase preferences as a consequence of synchronisation.

As shown in Fig. 3.4b (solid black), the visibility first increases to a maximal value then decreases to zero at $\Omega/\Omega_c \approx 0.8$, where Ω_c is the critical driving strength found in Sec. 3.3.2. Further increasing Ω , V increases again to a second local

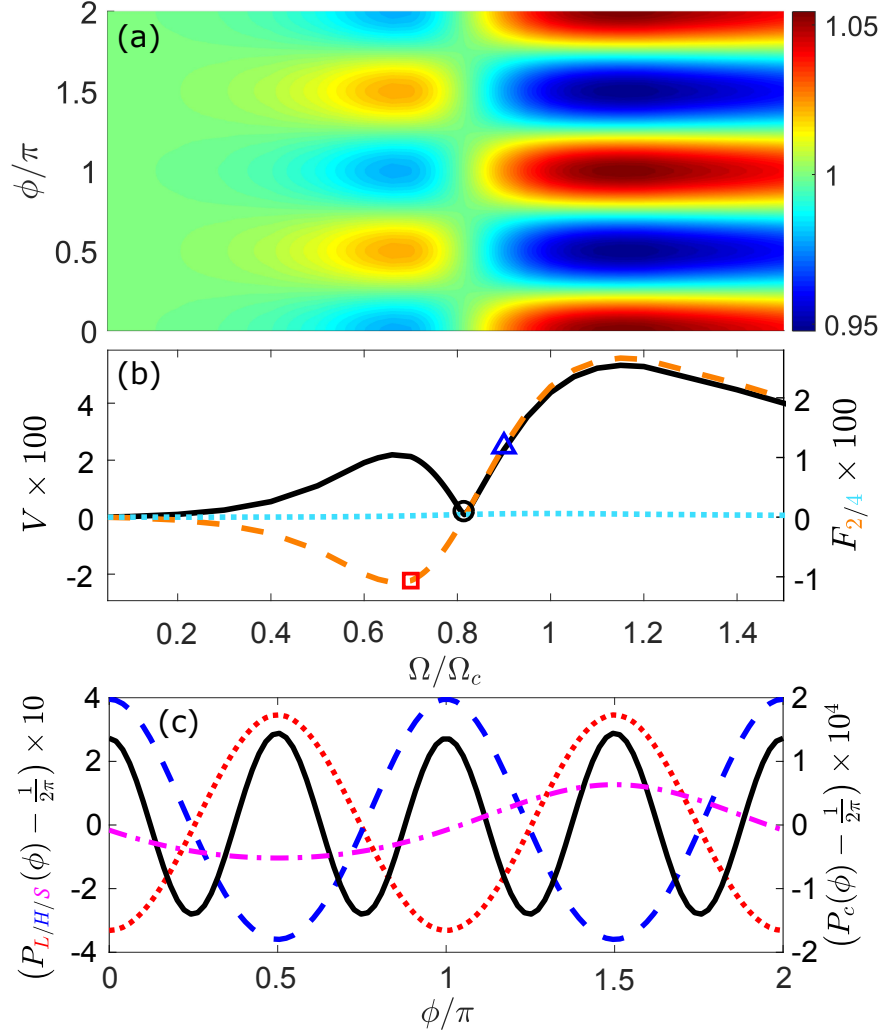


Figure 3.4: (a) The relative phase distribution $2\pi P(\phi)$ for two coupled oscillators for a range of driving strengths spanning a range that includes the bistability (with $J/\gamma = 0.03$, $\kappa/\gamma = 0.15$). (b) The visibility V (black solid), the dominant Fourier coefficient F_2 (orange dashed), and the second relevant Fourier coefficient F_4 (cyan dotted) which has a small positive value. (c) The relative phase distributions for low ($\Omega = 0.7\Omega_c$, red dotted), intermediate ($\Omega = 0.815\Omega_c$, black solid), and high ($\Omega = 0.9\Omega_c$, blue dashed) driving. These driving strengths are highlighted in the panel above with a red square, black circle, and blue triangle, respectively. Also included is the relative phase distribution for two asymmetrically driven oscillators (see Sec. 3.4.3, magenta dash-dot), with $\Omega_1/\Omega_c = 0.5$ and $\Omega_2/\Omega_c = 2$.

maximum. Upon closer inspection, we find that these two local maxima in the visibility correspond to different relative phase distributions. The relative phase has peaks at $\frac{\pi}{2}$ and $\frac{3\pi}{2}$ for low driving strengths and 0 and π for large driving

strengths. When driven around the critical point, where the visibility nears 0, all four peaks are present (0 , $\frac{\pi}{2}$, π , and $\frac{3\pi}{2}$).

To understand what determines the form of the relative phase distribution, we consider the individual Fourier coefficients of Eq. 3.23. Figure 3.4b shows that at zero-driving, all of the Fourier coefficients are zero, leading to a flat relative phase distribution. Note that the form of the coupling term (Eq. 3.4) ensures that the odd Fourier coefficients, F_{odd} , are zero for any driving strength. F_2 (orange dashed) dominates for the majority of the non-zero driving strengths leading to the π -periodicity of the relative phase seen in Fig. 3.4c (red dotted and blue dashed). The sign of F_2 dictates the position of the peaks before (red square) and after (blue triangle) the bistability. Though F_4 (dotted cyan in Fig. 3.4b) is always small, it becomes the dominant term as F_2 passes through zero (black circle). This results in a relative phase distribution with a $\frac{\pi}{2}$ -periodic structure, shown as the solid black curve in Fig. 3.4c.

The zero driving result, a flat distribution, is expected for ground state oscillators. We are also not surprised by the high driving results, with relative phase peaks of 0 and π , as in this regime the ions driven strongly enough to be described as coupled limit-cycle oscillators [25, 61, 104]. These results are well understood and are derived with a mean field calculation in Sec. 3.4.2. The low driving features, however, are unexpected and cannot be explained through simple mean field arguments. Similar relative phases, of $\frac{\pi}{2}$ or $\frac{3\pi}{2}$, are observed for the case of a non-lasing state being driven by a lasing state, as explained with asymmetrically driven oscillators in Sec. 3.4.3. Though the complexity of the trapped ion system makes it difficult to draw any conclusions from this result.

In the low driving region, the full Wigner distribution of the uncoupled ion (Fig. 3.5a) suggests an almost ground state oscillator. However, exploring the components of

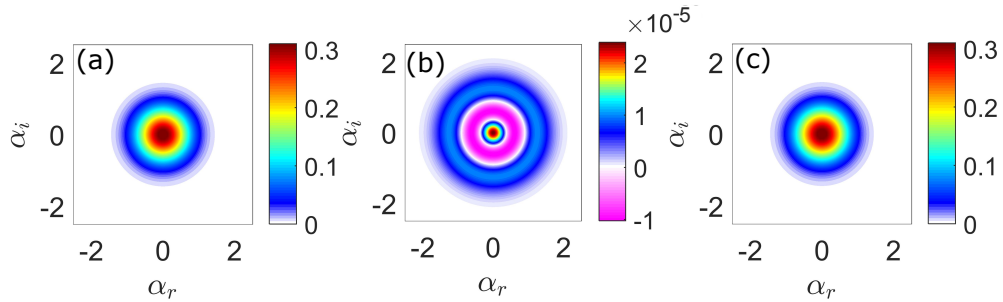


Figure 3.5: The Wigner distributions for one of the oscillators with extremely low driving strength ($\Omega = 0.1\Omega_c$) obtained using (a) the full density matrix $\hat{\rho}$, (b) the excited state projection $\langle e, e | \hat{\rho} | e, e \rangle$, and (c) the ground state projection $\langle g, g | \hat{\rho} | g, g \rangle$.

this Wigner distribution reveals a more complex story. The excited state projection ($\langle e, e | \hat{\rho} | e, e \rangle$, Fig. 3.5b) shows that the bistability exists for arbitrarily low driving strengths. Though the excited state contribution is small compared to the ground state contribution ($\langle g, g | \hat{\rho} | g, g \rangle$, Fig. 3.5c), it seems to have a significant effect on the relative phase distribution. For this reason, there may be certain similarities between the bistable state and an oscillator operating in the low driving regime. However, the negativity in the Wigner distribution projections make the results difficult to interpret and any attempt to find concrete parallels would require a simpler model than the trapped ion.

3.4.2 Mean field theory for high driving

The location of the peaks in the relative phase distribution $P(\phi)$ for strongly driven oscillators can be accurately predicted by a mean field approach, as has been studied previously to describe the coupling of two limit-cycles [25, 61, 104]. Here, we explain the relative phase values of 0 and π for the coupled, limit-cycle trapped ions with mean field arguments. For the coupled spin-oscillator system described

by Eq. 3.5, equations of motion for the spin operators follow from Eq. 3.10,

$$\frac{d}{dt}\langle\hat{\sigma}_j^-\rangle = -\frac{\gamma}{2}\langle\hat{\sigma}_j^-\rangle - \frac{i\Omega}{4}\left\langle\left(\hat{a}_j^\dagger\right)^2\hat{\sigma}_j^z\right\rangle. \quad (3.25)$$

for each oscillator, $j \in \{1, 2\}$. The phonon Eq. 3.9, however, becomes a pair of coupled equations, due to the form of Eq. 3.4

$$\frac{d}{dt}\langle\hat{a}_j\rangle = -\frac{\kappa}{2}\langle\hat{a}_j\rangle + \frac{i\Omega}{2}\left\langle\hat{a}_j^\dagger\hat{\sigma}_j^+\right\rangle - iJ\langle\hat{a}_k\rangle, \quad (3.26)$$

where $k \neq j$. For each oscillator, $\langle\hat{a}_j\rangle = \sqrt{n_j}e^{i\varphi_j}$, where n_j and φ_j are the classical number and phase variables for the j^{th} oscillator, respectively.

We can then study the dynamics of the relative phonon number $n = n_1 - n_2$ and relative phase $\phi = \varphi_1 - \varphi_2$ of the two oscillators by considering approximations.

For the strongly driven, but weakly coupled, system, we expect the two oscillators to be in lasing states (limit-cycles) such that the total phonon number $N = n_1 + n_2$ can be approximated as a constant and much larger than the relative phonon number $N \gg n$. In this regime, with the substitution $n_j = \langle\hat{a}_j^\dagger\hat{a}_j\rangle$, we find equations of motion for the relative quantities

$$\dot{n} \approx -\kappa n - 2NJ \sin \phi, \quad (3.27)$$

$$\dot{\phi} \approx \frac{2J}{N}n \cos \phi. \quad (3.28)$$

Weakly coupled oscillators (small J) produce low phonon numbers in each oscillator and, consequently, a low relative phonon number. Therefore, the phase (Eq. 3.28) can be seen to relax far slower than the phonon number (Eq. 3.27). This separation of timescales between \dot{n} and $\dot{\phi}$, allows us to substitute the steady state value of the relative phonon number, $n_{ss} = -\frac{2NJ}{\kappa} \sin \phi$, into Eq. 3.28. Rewriting

it as an effective potential [58], $\frac{d\phi}{dt} = -\frac{\partial U(\phi)}{\partial \phi}$, produces

$$U(\phi) = \frac{J^2}{\kappa} \cos 2\phi + \text{const.} \quad (3.29)$$

The minima of this potential, and thus the steady values of the relative phase, are found to be 0 and π . This result accurately predicts the location of the high driving peaks in $P(\phi)$ (Fig. 3.4). This solution only holds under the assumption of a limit-cycle and is therefore unable to describe the low driving peaks.

3.4.3 Asymmetrically coupled oscillators

To understand how phase preferences of $\frac{\pi}{2}$ and $\frac{3\pi}{2}$ can arise outside the limit-cycle regime, we consider the coupled dynamics of two oscillators with asymmetric driving $\Omega_1 \neq \Omega_2$. In the extreme case of heavily asymmetric driving, $\Omega_j \gg \Omega_k$ (where $j \in \{1, 2\}$ and $k \neq j$), this results in a non-lasing oscillator coupled to a limit-cycle oscillator. Numerical results for this system reveal relative phase distributions with a single peak at either $\frac{\pi}{2}$ or $\frac{3\pi}{2}$, as shown in magenta in Fig. 3.4c (where $\Omega_1 \ll \Omega_2$).

For the asymmetrically driven oscillators, we can use similar methods to those used in Sec. 3.4.2 to derive equations for the phases (defined in $\langle \hat{a}_j \rangle = \sqrt{n_j} e^{i\varphi_j}$),

$$\dot{\varphi}_j = -J \sqrt{\frac{n_k}{n_j}} \cos(\varphi_1 - \varphi_2), \quad (3.30)$$

for oscillators $j \in \{1, 2\}$ and $k \neq j$, where we explicitly allow for unequal driving, $\Omega_1 \neq \Omega_2$. We then find an equation of motion for the relative phase $\phi = \varphi_1 - \varphi_2$ (with $n = n_1 - n_2$ and $N = n_1 + n_2$),

$$\dot{\phi} = \dot{\varphi}_1 - \dot{\varphi}_2 = J \frac{n_1 - n_2}{\sqrt{n_1 n_2}} \cos \phi. \quad (3.31)$$

We now consider the case where the j^{th} oscillator is given a stronger driving $\Omega_j \gg \Omega_k$ and is therefore driven to the limit-cycle state, $n_j \gg n_k$. This allows us to approximate Eq. 3.31 as

$$\dot{\phi} \approx -(-1)^j \sqrt{\frac{n_j}{N - n_j}} \cos \phi \quad (3.32)$$

where the j^{th} oscillator is in the limit-cycle state, revealing an effective potential of the form

$$U_j(\phi) = (-1)^j J \sqrt{\frac{n_j}{N - n_j}} \sin \phi + \text{const.} \quad (3.33)$$

If the second oscillator is more strongly driven ($j = 2$), then Eq. 3.33 has a minimum at, and consequently reveals a fixed point phase of $\frac{3\pi}{2}$; in the opposite scenario ($j = 1$) a phase of $\frac{\pi}{2}$ is found. Though these values are the same as those found for weakly (symmetrically) driven oscillators, there is no obvious reason why we would be able to use such an argument outside of the asymmetrically driven regime.

3.4.4 Strong coupling

The peculiar 4-peak synchronisation feature present in the critical driving regime (black curve in Fig. 3.4c) is rather small, compared to the low and high driving features (red and blue curves in Fig. 3.4c). To increase the signal to allow for the features to be more readily detected, one would naturally try increasing the coupling strength, J . Figure 3.6a shows the P_n curves for the strongly coupled ($J/\gamma = 0.5$) system. The bistability now appears at a higher driving strength and, instead of a combination of a lasing state and a non-lasing state, we find two lasing states (blue triangles).

The relative phase distributions in Fig. 3.6b and 3.6c are not exactly the same as

in the weak coupling case. One difference being that the peaks are now orders of magnitude larger, as was the desired outcome. A second difference is that the driving strength at which the system transitions between synchronous regimes is shifted higher, as might be expected since the P_n is also shifted. Figure 3.6d makes it clear why the 4-peak feature is so much larger; the F_4 Fourier coefficient (dotted cyan), which is almost negligible in the weak coupling case, is now of comparable magnitude to the, still dominant, F_2 coefficient (dashed orange).

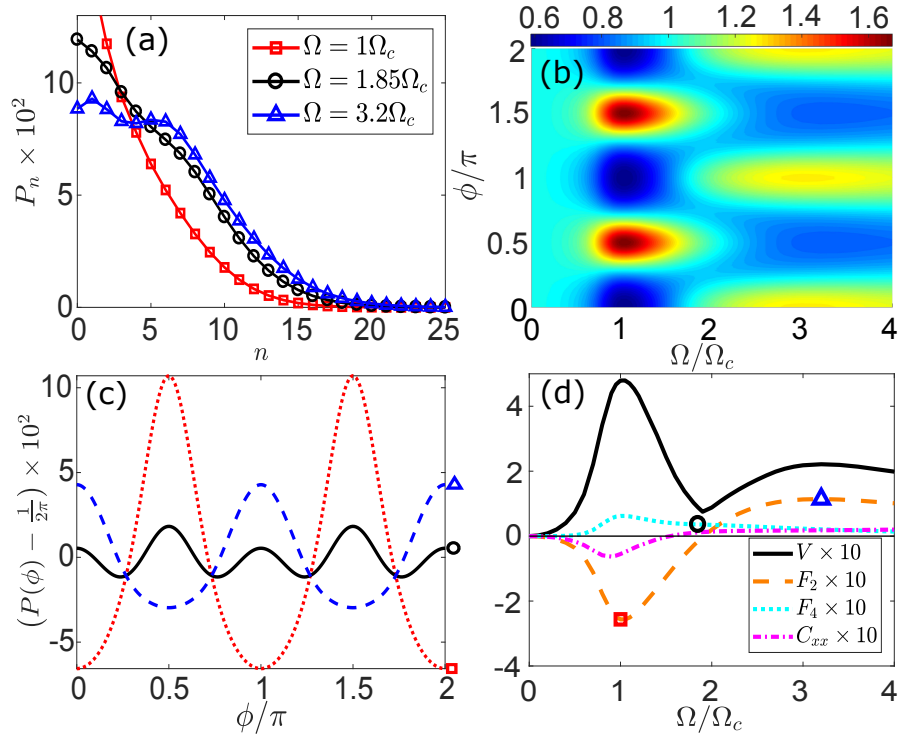


Figure 3.6: (a) Phonon state occupation probabilities for low (red squares), bistable (black circles), and high (blue triangles) driving of the strongly coupled oscillators, where $\kappa/\gamma = 0.15$, $J/\gamma = 0.5$. (b) The relative phase distribution, $P(\phi)$ for a range of driving strengths spanning the bistability. (c) The relative phase distribution for low driving (red dotted), intermediate driving (black solid), and high driving (blue dashed). (d) The visibility V (black solid), F_2 Fourier coefficient (orange dashed), F_4 (cyan dotted), the spin correlation $C_{xx} = C(\sigma_1^x, \sigma_2^x)$ (magenta dash-dot).

3.4.5 Spin covariance

Direct detection any of the relative phase features we have discussed is rather difficult with current technology and requires the complicated process of imaging the phonon state of an oscillator [20, 62]. To circumvent this issue, we can exploit the spin degree of freedom; important information about the phonon state can be inferred from a measurement of the spin state [49]. Due to the strong correlations between the spin and phonon degrees of freedom of each oscillator, a spin measurement can provide a signature of synchronisation in the phonon state. The covariance of two operators is calculated with

$$C(\sigma_1^\alpha \sigma_2^\alpha) = \langle \sigma_1^\alpha \sigma_2^\alpha \rangle - \langle \sigma_1^\alpha \rangle \langle \sigma_2^\alpha \rangle. \quad (3.34)$$

Figure 3.6d shows that the $C_{xx} = C(\sigma_1^x \sigma_2^x)$ (magenta dash-dot) has a qualitative similarity to F_2 (orange dash). This suggests that we can predict the relative phase of the coupled oscillators from the spin measurement; a negative (positive) C_{xx} predicts the relative phase peaks at $\frac{\pi}{2}$ and $\frac{3\pi}{2}$ (0 and π).

To understand the connection between spin and phase, we utilise the mean field approach in Eq. 3.14 to reveal a functional phase dependence of the spin expectation value, $\langle \hat{\sigma}_j^- \rangle \propto i \left\langle \left(\hat{a}_j^\dagger \right)^2 \right\rangle \propto i e^{-2i\varphi_j}$, and consequently, $\langle \hat{\sigma}_j^x \rangle \propto \sin 2\varphi_j$. Based on the fact that we find spin-phase correlations, e.g. $C(\hat{\sigma}^x, \hat{a}^2) \neq 0$, we make the ansatz that this proportionality applies not only to these expectation values, but also to the expectation values of products of operators

$$\hat{\sigma}_1^x \hat{\sigma}_2^x \propto \cos(2(\varphi_1 - \varphi_2)) + \cos(2(\varphi_1 + \varphi_2)), \quad (3.35)$$

which depends on the sum and difference of the phases. We then calculate the correlations using this ansatz and taking an average over the steady state relative

phase distribution in Eq. 3.23 (note that the corresponding “total phase distribution” is flat and the contribution from the phase-sum vanishes) to find

$$C(\sigma_1^x \sigma_2^x) \propto \int d\phi \cos(2\phi) P(\phi) = F_2, \quad (3.36)$$

where F_2 is the second Fourier coefficient (orange dashed), reinforcing its significance in contributing to the relative phase distribution.

3.5 Conclusion

We introduced a novel spin-oscillator system driven with a two-phonon resonant interaction that can be prepared in a bistable state. The model can be realised with highly controllable trapped-ions where the phonon state of the oscillators can be inferred from spin measurements. The high driving regime produces a relative phase preference of 0 and π which corresponds to coupled limit-cycles, as seen in the literature. New results were found in the low driving regime by decomposing the relative phase distribution into Fourier components. In this regime, the coupled ions display a relative phase distribution with peaks at $\frac{\pi}{2}$ and $\frac{3\pi}{2}$ or, for driving strengths that produce a bistability; 0, $\frac{\pi}{2}$, π , and $\frac{3\pi}{2}$. The relative phases of $\frac{\pi}{2}$ and $\frac{3\pi}{2}$ were also observed in asymmetrically driven oscillators that are described by the coupling of a limit-cycle oscillator with a non-lasing oscillator. The Wigner function resolved on the ion state revealed structures that might be associated with bistability in the limit of weak driving, but the negativity in this regime meant that the results were hard to interpret. Though the results suggest a possible link between the two scenarios, the complexity of the oscillator-spin system does not let us draw any clear conclusions. This led us to propose a simpler oscillator-only model that undergoes bistability and is discussed in the

following chapter.

Chapter 4

321 Oscillator

The interesting synchronisation features of the previous chapter arose from the two-phonon drive. The readily realisable but complicated framework of trapped ions may have initially been well motivated, but proved rather unideal both in terms of computationally probing higher driving regimes and fully understanding the phenomena. This motivated us to devise a new model that was still based around a two-quanta drive, in the hopes of again producing a bistable state, but this time we would focus on mathematical simplicity so as to develop a deeper insight into phase synchronisation patterns. In this chapter, we introduce the 321 oscillator: a minimal model without the complexity of a spin degree of freedom but with the two-phonon gain that drives a bistability. Without the spins, we are able to access a much larger region of the oscillator state-space.

Our model involves only dissipative processes in which phonons (quanta) are lost or gained, ensuring that an isolated oscillator never has a preferred phase. The key ingredient of the model responsible for generating bistability is the two-phonon gain process. This is balanced by two channels of phonon loss in which either a single phonon or three phonons are annihilated in the oscillator. Hence, we refer to it as the 321 model. Different dynamical states of the oscillator are achieved

by tuning the relative sizes of the gain and loss rates. Dominant loss leads to the low occupation number regime, dominant gain leads to a limit-cycle, and an intermediate region produces a bistability. In many ways, the model is a logical extension of the much studied Quantum van der Pol (QvdP) oscillator in Sec. 2.2.2 which combines one-phonon gain and two-phonon loss [61, 65, 66, 118]. The QvdP oscillator, however, only ever displays a limit-cycle whose size depends on the ratio of loss and gain rates.

We begin this chapter with an introduction to the 321 model in Sec. 4.1. Next, we look at the steady state and dynamical properties of a single 321 oscillator in Secs. 4.2-4.4. Then, in Sec. 4.5, we investigate in detail the phase synchronisation that occurs when two of the bistable model oscillators are coupled via a weak exchange process. This leads to a rich range of behaviour in the relative phase distribution with a different pattern of phase preferences emerging depending on the underlying dynamical states of the oscillators.

4.1 Model

Our oscillator model, the 321 oscillator, involves three dissipative processes, as illustrated in Fig. 4.1a. A two-phonon gain process with rate κ_2 drives the oscillator to higher phonon numbers, whilst a one-phonon loss process damps it at a rate κ_1 ; an additional three-phonon loss process at rate κ_3 is included to stabilise the system ensuring that it has a steady state for any strength of the gain.

The master equation for a single 321 oscillator in the interaction picture is given by [35, 61, 64]

$$\dot{\hat{\rho}} = \mathcal{L}\hat{\rho} = \kappa_1 \mathcal{D}[\hat{a}](\hat{\rho}) + \kappa_2 \mathcal{D}\left[(\hat{a}^\dagger)^2\right](\hat{\rho}) + \kappa_3 \mathcal{D}[\hat{a}^3](\hat{\rho}), \quad (4.1)$$

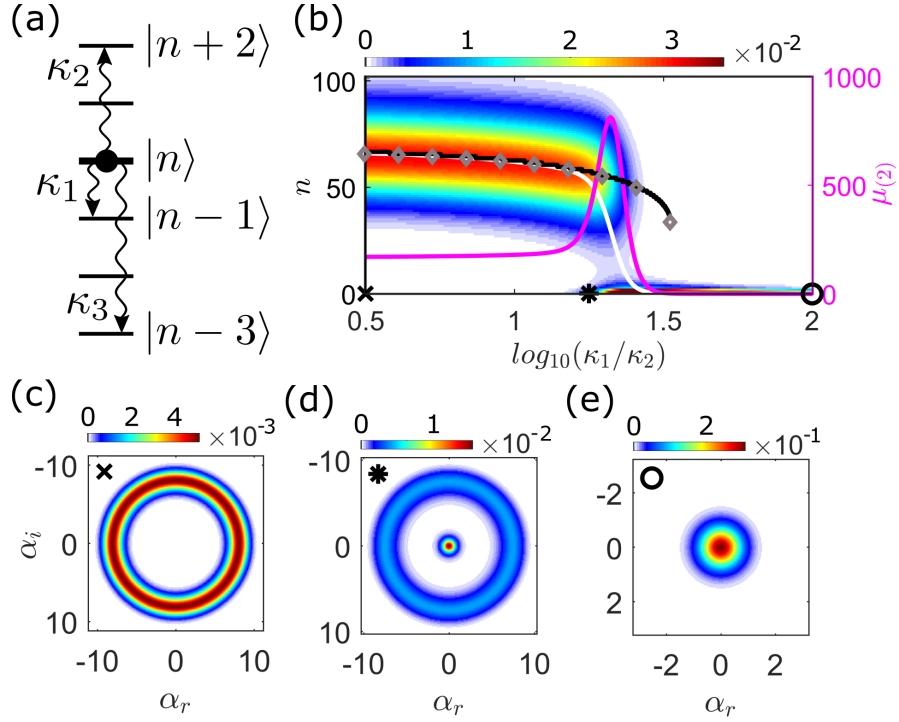


Figure 4.1: Reproduced from Jessop et al. [53]. (a) The three dissipative processes of the oscillator: two-phonon gain, single-phonon loss, and three-phonon loss, at rates κ_2 , κ_1 , and κ_3 , respectively. (b) Steady state properties as a function of κ_1/κ_2 for fixed $\kappa_3 = \kappa_2 \times 10^{-2}$. The colour scale shows the phonon-number distribution P_n (for $n > 0$), with the average phonon number $\langle n \rangle$ calculated numerically (white line), location of the peak in P_n away from $n = 0$ where it exists (black line), and the mean-field prediction n_+ (grey diamonds), superposed. Large phonon number states are occupied when the gain is sufficiently large (black cross), the fixed point state is predominantly occupied if the loss dominates (black circle), and a bimodal distribution appears in an intermediate region (black star). Also shown is the second moment $\mu_{(2)}$ (magenta line). The corresponding Wigner functions, $W(\alpha_r, \alpha_i)$, are for (c) limit-cycle ($\kappa_1/\kappa_2 = 10^{0.5}$), (d) bistability ($\kappa_1/\kappa_2 = 10^{1.25}$) and (e) fixed point ($\kappa_1/\kappa_2 = 10^2$).

where \hat{a} is the oscillator lowering operator and we have defined $\mathcal{D}[\hat{C}](\hat{\rho}) = \hat{C}\hat{\rho}\hat{C}^\dagger - \frac{1}{2}\{\hat{C}^\dagger\hat{C}, \hat{\rho}\}$. The key feature of the 321 oscillator is the two-phonon gain in the second term. Our model makes an interesting contrast with the QvdP oscillator [61, 118] in Eq. 2.12, where one-phonon gain is balanced by two-phonon loss. The presence of this nonlinear gain process in our model leads to important features such as bistability, not seen for the QvdP.

The steady state properties are readily found by exploiting the fact that the system is purely dissipative, so that the dynamics of the diagonal and off-diagonal matrix elements of the density operator in the number (Fock) basis are decoupled [102, 105]. The master equation can be rewritten as a set of k equations

$$\dot{\rho}^{(k)} = \mathcal{M}^{(k)}\rho^{(k)}, \quad (4.2)$$

where $\rho_n^{(k)} = \langle n | \hat{\rho} | n+k \rangle$, with $|n\rangle$ the n -th number state, and $\mathcal{M}^{(k)}$ a matrix. For the diagonal elements $\rho_n^{(0)} = P_n$, writing out Eq. 4.1 explicitly leads to the coupled set of equations for the probability distribution

$$\begin{aligned} \dot{P}_n = & - [\kappa_1 n + \kappa_2 (n+1)(n+2) + \kappa_3 n(n-1)(n-2)] P_n \\ & + \kappa_1 (n+1) P_{n+1} + \kappa_2 n(n-1) P_{n-2} \\ & + \kappa_3 (n+1)(n+2)(n+3) P_{n+3}. \end{aligned} \quad (4.3)$$

In the steady state, the off-diagonal terms $\rho^{(k \neq 0)}$ all go to zero and the eigenvector of $\mathcal{M}^{(0)}$ with zero eigenvalue gives the P_n distribution.

4.2 Steady state properties

4.2.1 Overview

The steady state of the oscillator can be characterised by the behaviour of the P_n distribution along with the Wigner distribution [35], $W(\alpha_r, \alpha_i)$. Figures 4.1b-e show how the state of the system evolves as the ratio κ_1/κ_2 is changed for a small (fixed) value of κ_3/κ_2 . When the nonlinear gain dominates ($\kappa_1/\kappa_2 \ll 1$) the oscillator is driven to large phonon numbers with an almost Gaussian P_n distribution centred at a value $\langle \hat{n} \rangle = \sum_n n P_n \gg 1$ (see Fig. 4.1b). The corresponding Wigner distribution exhibits a ring of maxima (Fig. 4.1c), we classify this as a *limit-cycle* (LC) state, as it has a well-defined average amplitude, but no preferred phase [61]. In the opposite limit of dominant loss ($\kappa_1/\kappa_2 \gg 1$), the oscillator is damped to the lowest phonon number states, leading to a sharp peak in the P_n distribution at $n = 0$. In this regime, the Wigner distribution displays a single maximum at the origin (Fig. 4.1e) and we call this a *fixed point* (FP) state. In between these limits, we find *bistability* (B) where features from both the LC and FP states can be found in the Wigner distribution (see Fig. 4.1d) and two peaks of similar size feature in the P_n distribution [98].

The bimodality of the P_n distribution is captured by a sharp peak in the second moment [76] $\mu_{(2)} = \langle \hat{n}^2 \rangle - \langle \hat{n} \rangle^2$, as shown in magenta in Fig. 4.1b. The distributions with the highest values of $\mu_{(2)}$ are found to be those with the most pronounced bistability, i.e. with two peaks of comparable area that are separated by a significant gap.

4.2.2 Mean-field theory

We use a standard mean-field (or semiclassical) approach to understand the origin of the stationary states. Two physically relevant mean-field solutions for the average phonon number are found: a zero phonon solution $n_0 = 0$ corresponding to the fixed point, and a nonzero solution

$$n_+ = \frac{\kappa_2}{3\kappa_3} \left[1 + \sqrt{1 - \frac{3\kappa_1\kappa_3}{\kappa_2^2}} \right] \quad (4.4)$$

corresponding to the limit-cycle. Linear stability analysis reveals that the zero phonon solution n_0 is always stable yet the nonzero solution n_+ is only real and stable for the parameters

$$3\kappa_1\kappa_3 < \kappa_2^2. \quad (4.5)$$

As such, the mean-field approach predicts a region of bistability associated with the coexistence of two stable solutions in the parameter regime defined by Eq. 4.5. These predictions are compared with the behaviour of the P_n distribution in Fig. 4.1b. The n_+ solution (grey diamonds) agrees remarkably well with the location of the peak away from $n = 0$ that develops in the P_n distribution (solid black line).

It is important to note that the results shown here (in Eq. 4.4 and Eq. 4.5) are not unique to this approach. The mean-field (or semiclassical) calculation we employ involves breaking the correlations between operators, such that $\langle \hat{A}\hat{B} \rangle \rightarrow \langle \hat{A} \rangle \langle \hat{B} \rangle$. We choose to make this break when the equation of motion is in a form with the fewest number of separate expectation values simply because this “least terms” method most accurately predicts the results found numerically. In the following, we outline how this works out in detail before going on to describe an alternative approach that employs normal ordering.

Least terms variant

An equation of motion for the expectation value of the annihilation operator, $\frac{d}{dt} \langle \hat{a} \rangle = \text{Tr} [\hat{a} \dot{\hat{\rho}}]$, is found from the master equation (Eq. 4.1)

$$\frac{d}{dt} \langle \hat{a} \rangle = -\frac{\kappa_1}{2} \langle \hat{a} \rangle + \kappa_2 \langle \hat{a}^2 \hat{a}^\dagger \rangle - \frac{3\kappa_3}{2} \langle (\hat{a}^\dagger)^2 \hat{a}^3 \rangle. \quad (4.6)$$

In this method, the expectation values in Eq. 4.6 are left intact, e.g. $\langle \hat{a}^2 \hat{a}^\dagger \rangle$ is not normal ordered (in which case it would be $2 \langle \hat{a} \rangle + \langle \hat{a}^\dagger \hat{a}^2 \rangle$). We then make the substitution of $\langle \hat{a} \rangle = (\langle \hat{a}^\dagger \rangle)^* = r e^{i\varphi}$ where $r = \sqrt{n}$ and φ are classical number and phase variables, respectively. This allows us to rewrite Eq. 4.6 as

$$\dot{r} + ir\dot{\varphi} = \frac{1}{2} (-\kappa_1 r + 2\kappa_2 r^3 - 3\kappa_3 r^5) \quad (4.7)$$

which, evaluating the real and imaginary parts separately, finds $\dot{\varphi} = 0$ and

$$\dot{r} = -\frac{r}{2} (3\kappa_3 r^4 - 2\kappa_2 r^2 + \kappa_1). \quad (4.8)$$

The steady state solutions can be found by evaluating $\dot{r} = 0$ and rearranging for r . This calculation produces three possible steady state solutions for the phonon number $n = r^2$; the trivial zero phonon solution $n_0 = 0$ and two nonzero solutions from the quadratic formula

$$n_{\pm} = \frac{\kappa_2}{3\kappa_3} \left[1 \pm \sqrt{1 - \frac{3\kappa_1\kappa_3}{\kappa_2^2}} \right], \quad (4.9)$$

the stable branch then becomes Eq. 4.4.

Since these solutions correspond to an observable (the average phonon number), the parameter regimes in which they are physical can be found by constraining

each solution to be both positive and real. The stability of the solutions can be determined through consideration of the Jacobian, $J_{ij} = \frac{\partial \dot{x}_i}{\partial x_j}$, where stability is indicated by the condition that $\text{Re} [J|_{n_{ss}}] < 0$.

The negative branch of the nonzero phonon solution n_- is never both physical and stable whereas the zero phonon solution n_0 is always stable. The positive branch of the nonzero phonon solution n_+ is stable only when it is physical; i.e. for $3\kappa_1\kappa_3 < \kappa_2^2$. This mean-field calculation results in two stable solutions for the average phonon number and therefore a predicted bistability in the phonon number for the parameters where n_+ is stable.

Normal ordered variant

An alternative approach is to carry out the mean-field calculation after ensuring the operators in the expectation values are normal ordered. We rearrange any product of bosonic creation \hat{a} and annihilation \hat{a}^\dagger operators using the commutation relation $[\hat{a}, \hat{a}^\dagger] = 1$ to ensure that the \hat{a}^\dagger operators always precede \hat{a} . The normal ordering of an operator \hat{O} (which is an arbitrary product of bosonic annihilation and creation operators) is denoted as $:\hat{O}:$. In our mean-field calculation, this leads to a rearrangement of the second expectation value in Eq. 4.6,

$$:\hat{a}^2\hat{a}^\dagger: = :\hat{a}(\hat{a}^\dagger\hat{a} + 1): = :\hat{a}\hat{a}^\dagger\hat{a}: + \hat{a} = (\hat{a}^\dagger\hat{a} + 1)\hat{a} + \hat{a} = \hat{a}^\dagger\hat{a}^2 + 2\hat{a} \quad (4.10)$$

so that the correlations are broken when the equation of motion is of the form

$$\frac{d}{dt} \langle \hat{a} \rangle = -\frac{\kappa_1}{2} \langle \hat{a} \rangle + \kappa_2 (2 \langle \hat{a} \rangle + \langle \hat{a}^\dagger \hat{a}^2 \rangle) - \frac{3\kappa_3}{2} \langle (\hat{a}^\dagger)^2 \hat{a}^3 \rangle. \quad (4.11)$$

Using this approach is equivalent to assuming the system is in a coherent state; i.e. the normal-ordered expectation values are $\langle (\hat{a}^\dagger)^j (\hat{a})^k \rangle = \langle \alpha | (\hat{a}^\dagger)^j (\hat{a})^k | \alpha \rangle =$

$\alpha^{*j}\alpha^k$. Continuing the calculation, we find

$$\dot{r} + ir\dot{\phi} = -\frac{3\kappa_3}{2}r^5 + \kappa_2r^3 + \left(2\kappa_2 - \frac{\kappa_1}{2}\right)r \quad (4.12)$$

which, evaluating the real and imaginary parts separately, leads to $\dot{\phi} = 0$ and

$$\dot{r} = \left[-\frac{3\kappa_3}{2}r^4 + \kappa_2r^2 + \left(2\kappa_2 - \frac{\kappa_1}{2}\right)\right]r, \quad (4.13)$$

with steady state solutions $n_0 = 0$ and

$$n_{\pm} = \frac{\kappa_2}{3\kappa_3} \left[1 \pm \sqrt{1 + \frac{3\kappa_3(4\kappa_2 - \kappa_1)}{\kappa_2^2}} \right]. \quad (4.14)$$

As before, the negative branch of the nonzero phonon solution n_- is never both physical and stable. The zero phonon solution n_0 , however, is found to be stable only for $\frac{\kappa_1}{\kappa_2} > 4$. The positive branch of the nonzero phonon solution n_+ is now stable for $\frac{\kappa_1}{\kappa_2} < 4 + \frac{\kappa_2}{3\kappa_3}$. This means that *with this particular mean-field approach*, there is a predicted bistability in the phonon number for the parameter regime

$$0 < \frac{3\kappa_3}{\kappa_2} \left(\frac{\kappa_1}{\kappa_2} - 4 \right) < 1. \quad (4.15)$$

This approach is not used in the following simply because it is less accurate at predicting the location of the nonzero peak in the number distribution, P_n , where it exists.

4.3 Phase diagram

Classifying the oscillator state as either FP, B, or LC, based on the corresponding Wigner function, can produce a ‘phase diagram’ shown with $\mu_{(2)}$ in Fig. 4.2a and

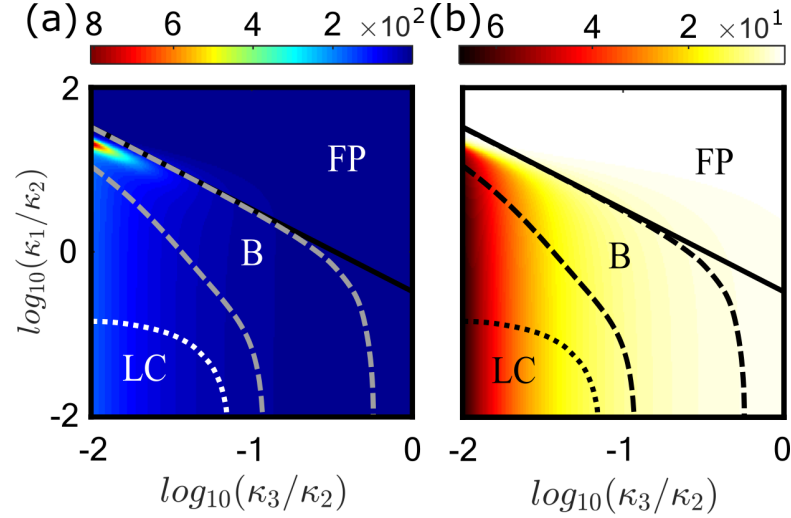


Figure 4.2: Reproduced from Jessop et al. [53]. Steady state behaviour of (a) the second moment $\mu_{(2)}$ and (b) average occupation number $\langle n \rangle$ overlaid with boundaries between the fixed point (FP), limit-cycle (LC), and bistable (B) regimes obtained by analysing the peaks in the radial Wigner distribution $W(r = |\alpha|)$. The FP-B boundary (upper dashed curve) agrees well with the appearance of the stable nonzero mean field solution, n_+ (see Eq. 4.4, full line). The LC-B boundary is shown using two different approaches: the dotted line indicates where the peak at the origin of the Wigner function disappears entirely, whilst the (lower) dashed line indicates the edge of a bistable region in which the Wigner peak at the origin remains *non-negligible* in size. The second moment is maximal within the bistable region where the corresponding LC contains a large occupation number (i.e. $\kappa_2 \gg \kappa_3$), elsewhere it is rather smooth. The average phonon number distribution $\langle n \rangle$ is largest deep within the LC regime (red), and lowest for the fixed point regions (white), but does not provide any direct indication of bistability.

average occupation number in Fig. 4.2b. The three states seem very distinct when considering examples such as Fig. 4.1c-e, and they clearly possess very different features. However, deciding on the boundary where one state transitions to another is far from simple and requires careful treatment so as to produce meaningful boundaries.

There is a very clear boundary between the fixed point and bistable regimes where the second distinct peak appears far from the origin. This phenomenon is easily captured by the mean-field prediction (solid line from Eq. 4.4) over a wide range of parameters and only fails when phonon numbers become small where the two

peaks become indistinguishable.

The transition between the limit-cycle and bistable regimes, however, is far more subtle and the location of the boundary is heavily affected by how we choose to define each state. Along with the upper bound from the mean-field prediction, we use two more methods to define the boundaries of the bistable regime that we believe allows us to produce a meaningful phase diagram. The first method uses an analytic result and acts as an absolute limit (dotted line), below which the state is certainly a limit-cycle. However, labelling any state above this bound as bistable would be inaccurate as many of the technically bimodal distributions include a fixed-point “peak” that is orders of magnitude smaller than the limit-cycle peak. To filter out states with negligible peaks and to produce a more meaningful definition for what should be considered a bistable state, we propose a *bistability contrast* and require that a state only be labelled bistable if this quantity is above a certain threshold. We now explain our approach in detail in the following two subsections.

4.3.1 Peak at origin

The criterion for bistability in the oscillator that we use is the coexistence of two peaks in the Wigner function, one at the origin and another at a nonzero radius [67]. Since the Wigner distribution is radially symmetric, the gradient at the origin must be zero and therefore we can ascertain if the origin is a maximum by analysing the second derivative. We utilise an analytic form of the Wigner distribution as a function of the density operator in the number basis $\rho_{nm} = \langle n | \hat{\rho} | m \rangle$ [39];

$$W(r, \theta) = \frac{2}{\pi} e^{-2r^2} \sum_{m,n=0}^{\infty} (-1)^n \sqrt{\frac{n!}{m!}} e^{i(m-n)\theta} (2r)^{m-n} L_n^{m-n} (4r^2) \rho_{nm} \quad (4.16)$$

where L_n^k are the associated Laguerre polynomials. The density matrix of the 321 oscillator is diagonal so $\rho_{nm} = \delta_{nm}P_n$, leading to a radial Wigner distribution which is a function of the probability distribution P_n [39]

$$W(r) = \frac{2}{\pi} e^{-2r^2} \sum_{n=0}^{\infty} (-1)^n P_n L_n(4r^2), \quad (4.17)$$

where $L_n = L_n^0$ are the Laguerre polynomials.

As we are considering the function at the origin $r = 0$, we can expand the Laguerre polynomials in orders of r and safely neglect high order terms $L_n(4r^2) = 1 - 4r^2 + \mathcal{O}(r^4)$. The approximated Wigner function near $r = 0$ is then

$$W(r) \approx \frac{2}{\pi} e^{-2r^2} \sum_{n=0}^{\infty} (-1)^n P_n (1 - 4r^2 n) \quad (4.18)$$

and the second derivative evaluated at the origin is

$$W''(r)|_{r=0} = -\frac{8}{\pi} \sum_{n=0}^{\infty} (2n+1)(-1)^n P_n, \quad (4.19)$$

shown in Fig. 4.3. The form of the Wigner distribution at the origin can then be easily calculated from the sign of Eq. 4.19: a negative (positive) second derivative indicates a maximum (minimum).

This calculation can be used to determine the parameter regime where there is *technically* a maximum in the Wigner distribution at the origin, acting as an absolute limit for the existence of a bistability (at the LC-B boundary), shown as a dotted black line in Fig. 4.3a. Using this criterion as an actual boundary for the bistable regime, however, would be unwise. The Wigner function at the origin is

calculated from Eq. 4.17 to be

$$W(r = 0) = \frac{2}{\pi} \sum_{n=0}^{\infty} (-1)^n P_n \quad (4.20)$$

and is shown on a log scale in Fig. 4.3c. This approach leads to a very large bistable region (non-white region in Fig. 4.3a) as it includes negligibly small peaks in the Wigner function.

4.3.2 Bistability contrast

To quantify just how small the second peak gets, and to produce meaningful criteria for what makes a state bistable, we must first define a quantifier of *bistableness*. We propose a measure called the *bistability contrast* that would consider distributions with similar peak sizes to be “more bistable” than those with comparatively negligible peaks. We would then be able to “filter out” the distributions with a small peak by altering our definition of a bistability to be dependent on contrast. We explicitly define the bistability contrast as

$$C = \min(W_0, W_+) - W_- \quad (4.21)$$

which compares the smaller of the two local maxima of the Wigner function, W_0 at the origin and W_+ away from the origin, with the minimum value between them, W_- .

Figure 4.3a shows this contrast plotted using a logarithmic scaling over the region where two peaks exist. We note that the Wigner function was found to be positive throughout. The plot shows that, whilst the FP-B boundary is very sharp (especially for $\kappa_2 \gg \kappa_3$), the LC-B boundary is extremely diffuse. There exists a large region of bimodal distributions where the peak at the origin is far too small

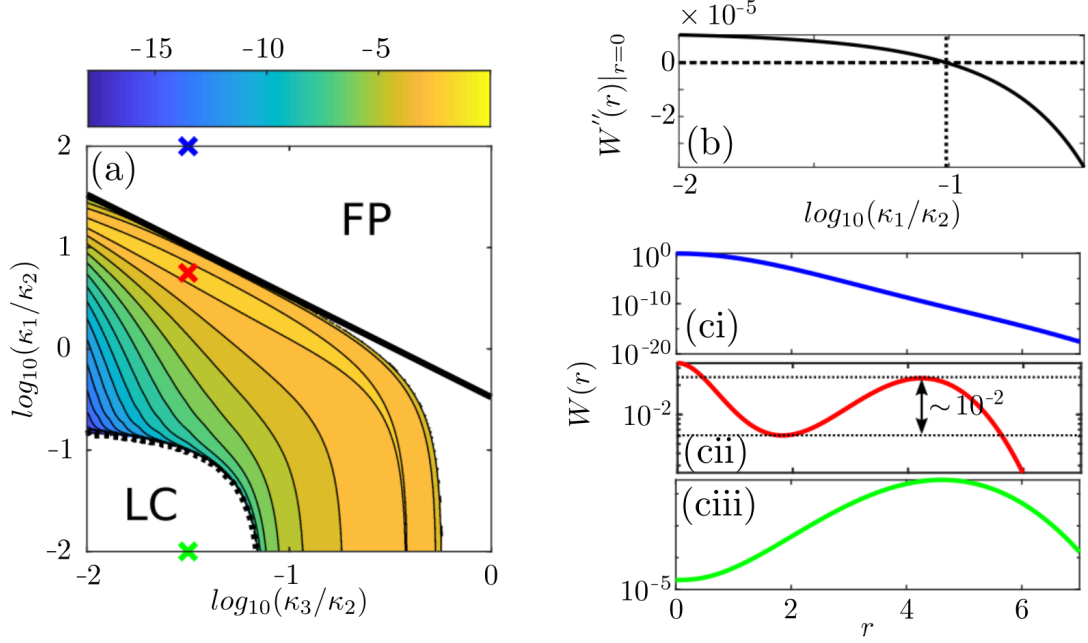


Figure 4.3: Reproduced from Jessop et al. [53]. Steady state phase diagram with the contrast of the bistability with a log scale and a series of contours at $10^{-[18:2]}$. The white regions indicate Wigner functions with only a single maximum, for example; (blue cross) a fixed-point (ci) has a single peak at $r = 0$ and (green cross) a limit-cycle (ciii) has a single peak at $r \geq 0$. The sign of (b) the second derivative of the Wigner distribution at $r = 0$ is used to determine if there is a maximum at the origin; i.e. a stable, $n_0 = 0$ solution ($\kappa_3 = \kappa_2 \times 10^{-1.5}$) and the locus where $W''|_{r=0} = 0$ is shown with the dotted line. The contrast is defined in Eq. 4.21 and an example is shown (red cross) for a strong bistability (cii) with a contrast of $C \approx 10^{-2}$. The solid black line shows the mean-field boundary (Eq. 4.5).

to play a meaningful role in affecting the system's behaviour. It makes sense to set the LC-B boundary at a point where the peak at the origin becomes small, rather than disappearing entirely. The choice of this limit will always be somewhat arbitrary. We decided on a boundary that agrees well with the peak in the second moment: $C = 0.0001$, as seen in Fig. 4.2a.

4.4 Dynamics

So far, only the steady state of the 321 oscillator has been discussed, we now turn our focus to the dynamics. To build an informative picture of the dynamics of the bistable state, we examine the key timescales in the system by looking at eigenvalues of the Liouvillian. To get additional insights into the dynamics, individual quantum trajectories are explored, using a quantum jump or Monte-Carlo wavefunction method [89].

4.4.1 Metastability

Preliminary time evolution of the 321 oscillator revealed a slowing of its relaxation to the bistable state, a feature often associated with metastability [79]. In order to understand whether the bistability found in the steady states of the system is accompanied by metastability, manifest in this system by a slow switching between the two coexisting states, we consider the eigenvalues of the Liouvillian with largest real part [70, 79, 97].

The largest eigenvalue of the matrices $\mathcal{M}^{(k)}$ in Eq. 4.2, $\lambda_1^{(k)}$, can be used to obtain the slowest timescale associated with the dynamics of $\rho^{(k)}$, $\tau_k = -1/\text{Re}[\lambda_1^{(k)}]$, examples of which are shown in Fig. 4.4a.

The $k = 0$ case, τ_0 , describes the relaxation of the diagonal elements and can

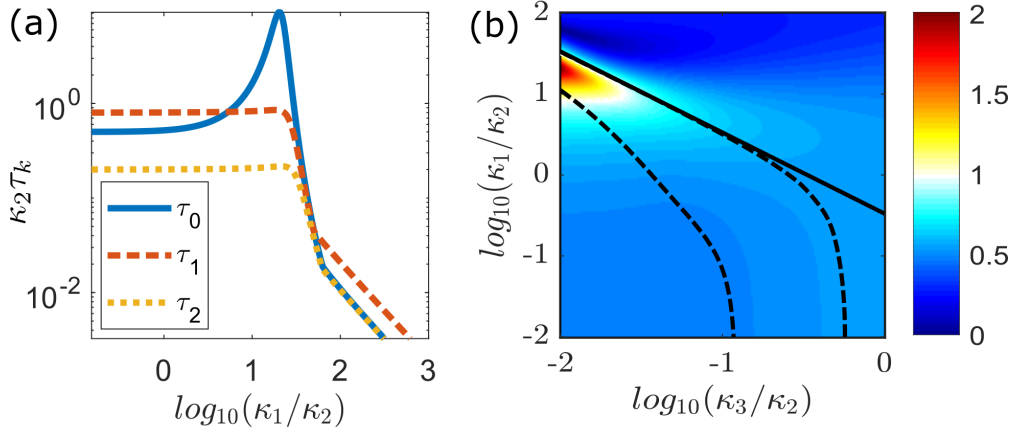


Figure 4.4: Reproduced from Jessop et al. [53]. (a) The slowest timescales τ_k of the oscillator for $k = 0, 1, 2$ with $\kappa_3 = \kappa_2 \times 10^{-2}$ and (b) the metastability M (Eq. 4.22) plotted on a logarithmic scale. The phase boundaries obtained using Wigner functions (dashed lines) and the mean field calculation (full line) are shown.

become very large for certain κ_1/κ_2 values. The other timescales, $\tau_{1,2}$, describe the relaxation of the phase preference of the system. Though they never approach the peak values of τ_0 and display no signature of the bistability, they do vary significantly as the system evolves from FP to LC, becoming orders of magnitude larger for the latter.

In this system, the emergence of a single very slow timescale signals metastability [70]. The metastability of the system can be calculated from the ratio of the largest (least negative) eigenvalues

$$M = \frac{\text{Re}[\lambda_2^{(0)}]}{\text{Re}[\lambda_1^{(0)}]}. \quad (4.22)$$

M is much larger than unity when there is a wide separation of timescales. The behaviour of M is shown in Fig. 4.4b, where a rough, if somewhat arbitrary, threshold for metastability $M = 10$ is shown in white. Although the region where

M is large is much smaller than the bistable region in Fig. 4.2, it does match up well with the peak in $\mu_{(2)}$.

4.4.2 Quantum jump trajectories

We can get more of an insight into the dynamical properties of the system by looking at quantum jump trajectories obtained by unravelling the master equation [89]. The system is evolved in time with a non-Hermitian Hamiltonian and, at each time step, a quantum jump (the 1-phonon loss, 2-phonon gain, or 3-phonon loss process) may occur with a certain probability.

The wavefunction $|\psi(t)\rangle$ is evolved from $t \rightarrow t + \delta t$ according to a randomly generated number c which determines whether a jump process occurs or the state is instead evolved by the non-hermitian Hamiltonian $\hat{H}_{MC} = -\frac{i}{2} \left[\kappa_1 \hat{a}^\dagger \hat{a} + \kappa_2 \hat{a}^2 (\hat{a}^\dagger)^2 + \kappa_3 (\hat{a}^\dagger)^3 \hat{a}^3 \right]$. Each jump process occurs at a probability dependent on the evolution timestep and expectation value of that operator at that time, e.g. the probability that the two-phonon gain process $(\hat{a}^\dagger)^2$ occurs is $p_2 = \kappa_2 \langle \psi(t) | (\hat{a}^\dagger)^2 | \psi(t) \rangle \delta t$. Repeating this process for many time steps produces a trajectory of the dynamics. A sufficient number of such trajectories will average to the steady state of the system.

The properties of typical trajectories for the different dynamical states of the system are illustrated in Fig. 4.5. The FP oscillator has a very low phonon number and so all jump processes are heavily suppressed, seen as a low activity (i.e. low rate of jump events) shown in blue in Fig. 4.5, especially the three-phonon loss. The LC has a large number of phonons and so all processes are likely, shown in red in Fig. 4.5, with the the single-phonon loss being slightly reduced in comparison to the other two. In the bistable regime, green in Fig. 4.5, the oscillator can be seen to spend a period of time exhibiting one level of activity before switching to the

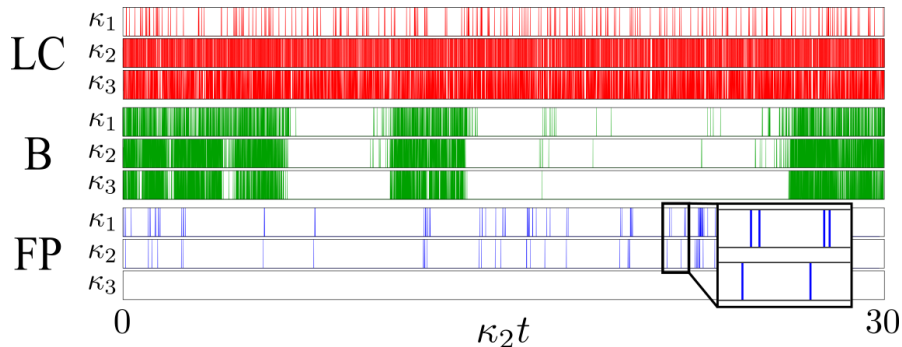


Figure 4.5: Reproduced from Jessop et al. [53]. Sample quantum trajectories for each of the oscillator states illustrating the frequency of the different jump processes for (top) limit-cycle ($\kappa_1 = \kappa_2 \times 10^{1/2}$), (middle) bistable ($\kappa_1 = \kappa_2 \times 10^{5/4}$), and (bottom) fixed-point ($\kappa_1 = \kappa_2 \times 10^{7/4}$) states (with $\kappa_3 = \kappa_2 \times 10^{-7/4}$ throughout). The individual jump processes involving one-phonon loss (rate κ_1), two-phonon gain (rate κ_2), and three-phonon loss (rate κ_3) are indicated. The bistable oscillator can be seen to flip intermittently between LC-like and FP-like behaviour. In the FP state, the one-phonon loss jumps occur in pairs soon after each two-phonon gain jump (see magnified portion of the lower panel).

other. The system continues to switch between these distinct regimes indefinitely, never settling in one state or the other. This intermittency in the dynamics of the trajectories provides clear evidence of metastability in the system [70].

4.5 Synchronisation of two coupled 321 oscillators

We now explore how phase ordering occurs when two identical 321 oscillators are coupled via a phonon exchange interaction of the form [49, 61, 118] $\hat{H}_J = J (\hat{a}_1^\dagger \hat{a}_2 + \hat{a}_1 \hat{a}_2^\dagger)$ with subsequent dynamics described by the master equation

$$\dot{\hat{\rho}} = -i [\hat{H}_J, \hat{\rho}] + \sum_{j=1,2} \mathcal{L}_j \hat{\rho}, \quad (4.23)$$

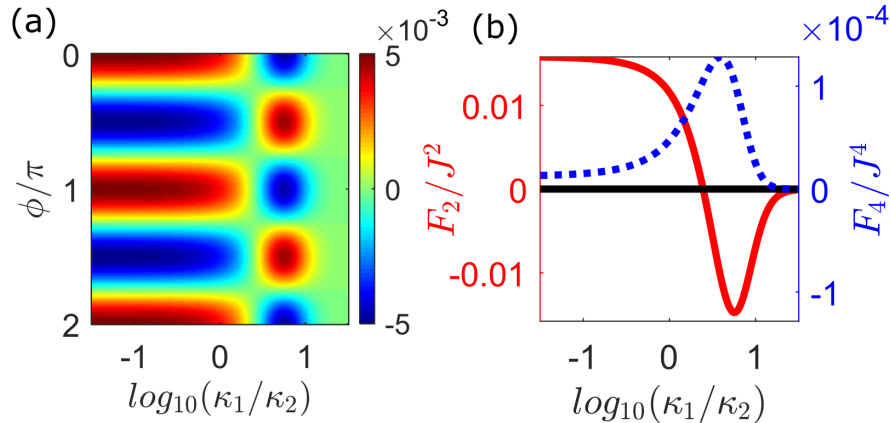


Figure 4.6: Reproduced from Jessop et al. [53]. (a) The predominantly π -periodic relative phase distribution of the two-oscillator system with weak coherent coupling ($J/\kappa_2 = 10^{-2}$) and three-phonon loss $\kappa_3 = \kappa_2 \times 10^{-1}$, spanning the three motional states (FP, B, and LC) calculated with perturbation theory. Weak single-phonon loss ($\kappa_1 < \kappa_2$) produces the case of coupled limit-cycles and has peaks at 0 and π . As the single-phonon loss rate is increased, the pattern vanishes then reappears with peaks at $\frac{\pi}{2}$ and $\frac{3\pi}{2}$. Very strong single-phonon loss ($\kappa_1 \gg \kappa_2$) suppresses synchronisation. (b) The dominant Fourier coefficient F_2 (red), explained in Eq. 3.23, that accounts for the π -periodic form and whose sign determines the peak position. The fourth Fourier coefficient F_4 (blue) is the next largest, though is negligible in comparison for all parameter regimes except for the region in which $F_2 \approx 0$ where a four-peak, $\frac{\pi}{2}$ -periodic distribution can be observed.

where the subscript j denotes the first or second oscillator and the dissipation terms follow from Eq. 4.1.

By considering a relatively weak coupling strength, the phonon state can be assumed to be predominantly determined by κ_1 , κ_2 , and κ_3 , as with the uncoupled oscillator. The phase of each oscillator, however, is expected to be strongly affected by the coupling process and a nontrivial relative phase distribution is indeed produced. As the P_n transitions from limit-cycle to bistability to fixed point (by increasing the loss rates, κ_1 or κ_3), the relative phase distribution changes from having peaks at 0 and π to $\frac{\pi}{2}$ and $\frac{3\pi}{2}$, as seen in Fig. 4.6a. The relative phase of 0 and π for the coupled limit-cycles (LHS of Fig. 4.6a) are expected [61] and can be predicted by a simple mean field argument (see Sec. 3.4.2). The peaks at

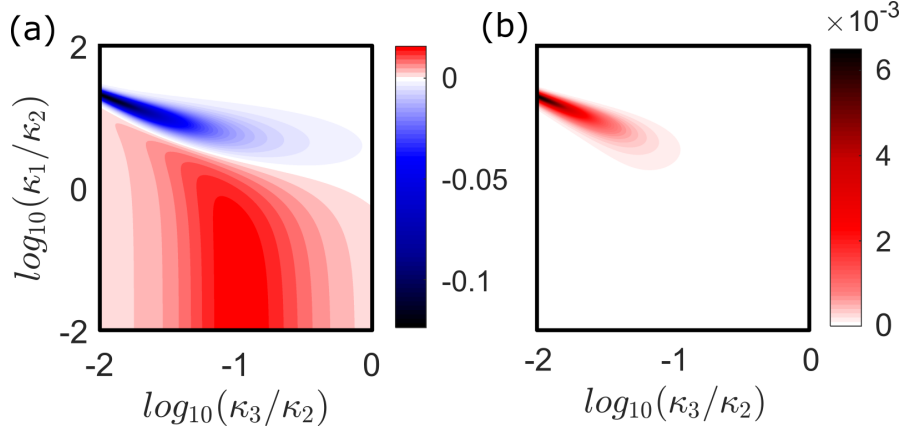


Figure 4.7: Reproduced from Jessop et al. [53]. (a) F_2/J^2 and (b) F_4/J^4 , the two most dominant Fourier coefficients of the relative phase distribution scaled with coupling strength (Eq. 3.23) showing the parameter regimes that have a π -periodic form where positive F_2 (red) produces peaks at 0 and π and negative F_2 produces peaks at $\frac{\pi}{2}$ and $\frac{3\pi}{2}$. When F_2 switches from positive to negative, it travels through zero and the small but nonzero F_4 becomes the dominant term producing a $\frac{\pi}{2}$ -periodic relative phase distribution with peaks at 0, $\frac{\pi}{2}$, π , and $\frac{3\pi}{2}$.

$\frac{\pi}{2}$ and $\frac{3\pi}{2}$ for the coupled fixed point oscillators (RHS of Fig. 4.6a), however, are unusual, but as we have seen do arise for the bistable coupled ion system discussed in Chapter 3.

Solving the coupled system numerically is computationally taxing but possible with sufficient state space truncation. To avoid this limitation, perturbation theory can be used to accurately describe the system in the limit of weak coupling strength and can probe parameter regimes that drive the system to far larger phonon numbers, leading to the results shown in Fig. 4.7 (see App. B).

To try and understand the origin of the peaks that appear at $\frac{\pi}{2}$ and $\frac{3\pi}{2}$, we can exploit the fact that they already start to appear in the regime where $\langle n \rangle$ is very low (i.e., $\kappa_1/\kappa_2 \gg 1$). Hence, we can take the perturbation theory further (see App. B), and derive analytic results by truncating the system to the lowest 3 states (maximum phonon number of $N = 2$). This results in a relative phase distribution

of the form

$$P(\phi) = \frac{1}{2\pi} + S \cos 2\phi \quad (4.24)$$

where the sign of S , and therefore the relative phase preference, simply depends on the state of both oscillators

$$\text{sgn}(S) = \text{sgn} \left(P_1^{(1)} P_1^{(2)} - P_0^{(1)} P_2^{(2)} \right). \quad (4.25)$$

An oscillator with a thermal distribution would obey $P_2/P_1 = P_1/P_0$ and so two thermal oscillators would be unsynchronised $P(\phi) = \frac{1}{2\pi}$. The vdP oscillator driven with a single phonon process only ever produces states with $P_2 P_0 < P_1^2$ which results in the usual phase preference of 0 and π [61], these states are also accessible by the 321 oscillator. Producing a negative S value is impossible for a thermal or vdP oscillator thus they will never achieve a relative phase preference of $\frac{\pi}{2}$ and $\frac{3\pi}{2}$. The two-phonon gain process in the 321 oscillator, however, generates a large population in the third state ($n = 2$) by bypassing the second ($n = 1$) which allows for the production of states where $P_2 P_0 > P_1^2$. This specific phonon distribution produces a negative S value in Eq. 4.25 and thus a relative phase distribution in Eq. 4.24 with peaks at $\frac{\pi}{2}$ and $\frac{3\pi}{2}$. This relative phase distribution was found in the coupled ions in Chapter 3. With the 321 oscillator model, we were able to carry out a much more detailed analysis that revealed the relative phase preference of $\frac{\pi}{2}$ and $\frac{3\pi}{2}$ is caused by the two-phonon gain process and that this can be achieved without the cumbersome spin degree of freedom of the ions. The simplicity of the 321 oscillator has allowed us to determine that the interesting phase distributions of bistable oscillators is directly due to the two-phonon gain, a far stronger conclusion than was possible with the ion system in Chapter 3. As shown in Chapter 3, we find that the periodic nature of the relative phase

distribution allows for the Fourier decomposition shown in Eq. 3.24. The F_{odd} are always zero and, in general, the F_k terms become negligibly small as k is increased. The distribution is predominantly π -periodic, this is seen in Fig. 4.6b with a dominant F_2 term (blue). The position of the two peaks is determined by the sign of F_2 . As F_2 passes through zero, the normally negligible F_4 term becomes dominant and a $\frac{\pi}{2}$ -periodic distribution is observed. The relative phase distribution can then be succinctly displayed for the full parameter space as shown in Fig. 4.7. A positive F_2 (red Fig. 4.7a) corresponds to relative phase peaks at 0 and π . The parameter regime with negative F_2 (blue Fig. 4.7a), however, shows a relative phase preference of $\frac{\pi}{2}$ and $\frac{3\pi}{2}$. The F_4 term (Fig. 4.7b) is normally 3 orders of magnitude smaller than F_2 and so only becomes significant in the small parameter regime where F_2 passes through zero. F_4 is always positive and therefore produces a relative phase distribution with peaks at 0, $\frac{\pi}{2}$, π , and $\frac{3\pi}{2}$. Interestingly, the peak in F_4 is most pronounced (and the change between positive and negative F_2 values is most rapid) in the metastable region.

Curiously, in the limit-cycle regime ($\kappa_1 < \kappa_2$), synchronisation is seen to weaken as κ_3 is reduced (see Fig. 4.7) and the phonon number is increased (see Fig. 4.2b). This is in contrast to the QvdP oscillator in which the synchronisation effects are enhanced by increasing phonon number, as shown in Eq. 2.28. This can be explained by realising that the synchronisation strength depends sensitively on the rate of phase diffusion in the oscillator [25, 105]. In our system, the phase diffusion can be shown to increase with increasing drive strength (see App. C) which explains why the phase locking is in fact weakened by larger phonon numbers.

4.6 Conclusion

We have introduced a simple oscillator model with a two-phonon gain process balanced by one- and three-phonon losses that can be used to engineer a bistable oscillator state. The bistability occurs when the gain/loss rates are tuned between a large phonon, limit-cycle regime and a low occupation number, fixed state regime. Quantum jump simulations reveal trajectories with intermittent activities in the bistable regime, signalling that the bistable state is also metastable.

The relative phase distribution of two coherently coupled 321 oscillators displays a rich pattern of behaviours that are dependent on the phonon state of the oscillators. When strongly driven, the coupled oscillators have the usual, predominantly π -periodic distribution with peaks at 0 and π as found for coupled van der Pol oscillators. If, instead, the loss process dominates, phase peaks are found at $\frac{\pi}{2}$ and $\frac{3\pi}{2}$. Between these two regimes, where the bistability arises, the distribution is shown to become $\frac{\pi}{2}$ -periodic.

In the limit-cycle regime, mean-field theory tells us that the form of the relative phase distribution is determined by the form of the coupling between the oscillators, as found in classical models. The phase distribution in the fixed-point regime, however, is determined by the form of the nonlinear gain/loss terms which determines the number distribution. In our model, the two-phonon gain process produces a fixed-point number distribution that results in preferred phases $\frac{\pi}{2}$ and $\frac{3\pi}{2}$, something not seen for thermal distributions or QvdP oscillators.

Our goal in this work was to explore the properties of the relative phase distribution and its connection to the underlying oscillator dynamics in the simplest possible model system displaying limit-cycles and bistability. The 321 oscillator proved to be both considerably simpler than the trapped ion model in Chapter 3, allowing us to carry out more accurate analysis and explore a greater parameter

range, whilst still being able to display the bistable state we aimed to study.

Chapter 5

Synchronisation in spin-1 networks

The last two chapters focused on oscillators that can occupy a large number of energy levels and so can accurately describe large amplitude oscillations. However, simulations of such systems require state spaces that can become computationally expensive, limiting our research to a maximum of two coupled oscillators. In this chapter, we will instead look at minimising the size of the Hilbert space of the system undergoing limit-cycle oscillations to facilitate research on synchronisation in larger networks of coupled oscillators.

Recent studies have concluded that the smallest quantum system capable of sustaining a limit-cycle and subsequently synchronise is a spin-1 oscillator [100, 101]. This, however, remains an area of controversy [84]. Nevertheless, spin-1 oscillators are certainly a useful platform to study synchronisation in the quantum regime and, in fact, map directly to a QvdP oscillator deep in this limit [57]. Additionally, this model has been recently realised experimentally in chains of trapped ions [22, 106], nitrogen-vacancy centres [109], and noisy intermediate-scale quantum computers [56].

In this chapter, we aim to study how synchronisation manifests in different networks of coupled spin-1 oscillators. In Sec. 5.1, we describe the limit-cycle in the context of the spin-1 oscillator and explain how to visualise the state with the Husimi-Q function. Section 5.2 will introduce interactions between oscillators along with a minimal synchronisation measure that proves particularly applicable to spin-1 networks. We begin Sec. 5.3 by studying two coupled oscillators and find a rich variety of synchronisation features, including a relative phase preference between identical oscillators, contradicting recent work [100]. Adding a third oscillator to the system allows us to compare features of an all-to-all coupled network to a chain geometry. Surprisingly, we find a strengthening of the next-nearest neighbour synchronisation in the chain network. Working with larger networks, of 4 and 5 spins, we study the effects of increasing system size as well as compare all-to-all, chain, and ring geometries. We find simple, but exact, equations to describe the relative phase distributions between each pair of oscillators in networks of varying geometry and size.

5.1 The spin-1 oscillator

The spin-1 oscillator is in stark contrast to the trapped ion model in Chapter 3, whose complexity often meant we had to rely on slow numerical integration methods to reach the steady state. As we simplified that model to the 321 oscillator in Chapter 4, we will simplify our system again, rather extremely. Since the spin-1 oscillator consists of just three energy levels, $|-\rangle$, $|0\rangle$, and $|+\rangle$, we are able to model networks of multiple coupled oscillators with ease. Interestingly, this model can describe a van der Pol oscillator operating deep in the quantum regime [57]. For these reasons, the spin-1 oscillator network is both an exciting leap and a natural progression of our previous research.

5.1.1 The smallest limit-cycle

Though some work has been carried out on the synchronisation of spin- $\frac{1}{2}$ qubits [56], we will follow the rationale of Ref. [100] and work with the spin-1 oscillator due to its well defined limit-cycle and direct correspondence to the QvdP oscillator (see Chapter 2). To understand the states of the spin-1 oscillator, we utilise a pseudo-probability function, as we did in previous chapters. Recent research on the spin-1 oscillator has employed the Husimi-Q function as a phase portrait [57, 100, 101]; we will follow suit. The Husimi-Q function is found by extending the Bloch sphere to accommodate a third energy level [57, 100, 101]. Spin coherent states [7, 93] follow from a two-angle rotation of the extremal state

$$\begin{aligned} |\theta, \varphi\rangle &= e^{-i\varphi\hat{S}^z} e^{-i\theta\hat{S}^y} |+\rangle \\ &= \frac{1}{2}(1 + \cos\theta)e^{-i\varphi} |+\rangle + \frac{1}{\sqrt{2}} \sin\theta |0\rangle + \frac{1}{2}(1 - \cos\theta)e^{i\varphi} |-\rangle \end{aligned} \quad (5.1)$$

with $\hat{\sigma}^z = |+\rangle\langle+| - |-\rangle\langle-|$ and $\hat{\sigma}^y = 1i(|-\rangle\langle+| - |+\rangle\langle-|)$.

The Husimi-Q function (Eq. 5.2) for the spin-1 oscillator is then a sphere defined by θ and φ

$$Q(\theta, \varphi) = \frac{3}{4\pi} \langle \theta, \varphi | \hat{\rho} | \theta, \varphi \rangle, \quad (5.2)$$

with $\theta \in [0, \pi]$ and $\varphi \in (-\pi, \pi]$. We visualise the distribution with the Winkel tripel earth projection [42], much like a map of the globe, where θ runs from the north to the south pole, 0 to π , and φ from west to east, $-\pi$ to π .

A selection of states of the oscillator, $|-\rangle\langle-|$, $|0\rangle\langle 0|$, and $|+\rangle\langle+|$, are illustrated in Fig. 5.1a-c, respectively. The Husimi-Q function for the $|0\rangle\langle 0|$ state is found analytically from Eq. 5.2,

$$Q_0(\theta, \varphi) = \frac{3}{8\pi} \sin^2 \theta \quad (5.3)$$

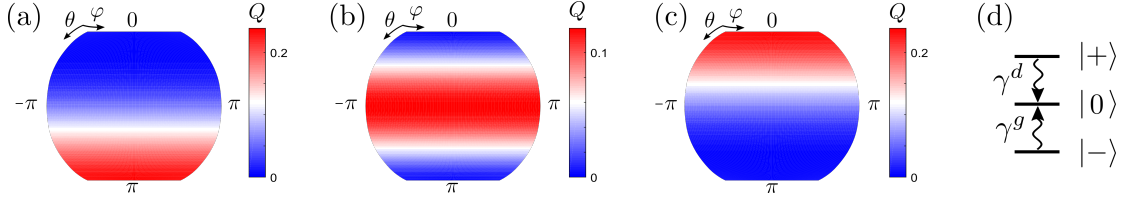


Figure 5.1: The Husimi-Q function, Eq. 5.2, acting as a phase portrait of the (a) $|-\rangle\langle -|$, (b) $|0\rangle\langle 0|$, and (c) $|+\rangle\langle +|$ states represented using the Winkel tripele earth projection [42]. For $\hat{\rho} = |0\rangle\langle 0|$, it takes the form in Eq. 5.3 showing a φ independence and a maximal value of $\theta = \frac{\pi}{2}$. (d) The dissipative processes (see Eq. 5.5) that drive our spin-1 oscillator from the extremal states, $|+\rangle$ and $|-\rangle$, to the limit-cycle state $|0\rangle$, at rates γ^d and γ^g , respectively.

and is shown in Fig. 5.1b. This state is independent of φ and is maximal at $\theta = \frac{\pi}{2}$, forming a ring structure around the equator which is reminiscent of the undefined phase and stable amplitude of the classical limit-cycle. Taking the freely rotating angle φ to be the phase of the spin-1 oscillator, we find our limit-cycle state which is analogous to those of larger oscillators (see Sec. 2.2.2 and Chapters 3 and 4).

For other two states, $|\pm\rangle\langle \pm|$, the Husimi-Q function has the form

$$Q_{\pm}(\theta, \varphi) = \frac{3}{16\pi} (\cos \theta \pm 1)^2. \quad (5.4)$$

These are also independent of φ , but lie on the poles of the sphere (at $\theta = 0$ and π , respectively) where φ becomes undefined. Therefore, we cannot associate a meaningful phase to the extremal states consequently they cannot form a limit-cycle state.

Next, we devise an open system dynamics that will relax to our spin-1 limit-cycle state $|0\rangle\langle 0|$. The state must be stabilised to perturbations without the introduction of a phase preference (see Sec. 2.1). This is achieved with the dissipation channels shown in Fig. 5.1d which independently relax populations in the extremal states, $|\pm\rangle$, to the limit-cycle with gain and damping rates γ^g and γ^d , respectively. The master equation that governs these dynamics is $\dot{\hat{\rho}} = \mathcal{L}\hat{\rho}$ in the interaction picture,

with the Lindblad superoperator

$$\mathcal{L}\hat{\rho} = \frac{1}{2} (\gamma^g \mathcal{D} [\hat{\sigma}^+ \hat{\sigma}^z] \hat{\rho} + \gamma^d \mathcal{D} [\hat{\sigma}^- \hat{\sigma}^z] \hat{\rho}), \quad (5.5)$$

where $\hat{\sigma}$ are the spin-1 raising and lowering operators $\hat{\sigma}^\pm = |0\rangle\langle\mp| + |\pm\rangle\langle 0|$ and $\hat{\sigma}^z = |+\rangle\langle+| - |-\rangle\langle-|$. To quantify the extent to which the state of our system deviates from the limit-cycle in what follows, we use a deformation measure [57]

$$p_{max} = \max_{s \in \{-, 0, +\}} |\langle s | (\hat{\rho} - |0\rangle\langle 0|) |s\rangle|. \quad (5.6)$$

This measure calculates the maximum change of populations $\langle s | \hat{\rho} |s\rangle$, where $s \in \{-, 0, +\}$, of the state $\hat{\rho}$ from the limit-cycle state, $|0\rangle\langle 0|$, and can be thought of as a simplified fidelity [54].

The phase distribution of a state of the system can be found by integrating the Husimi-Q function (Eq. 5.2) over the angle θ [101]

$$p(\varphi) = \int_0^\pi d\theta \sin \theta Q(\theta, \varphi) - \frac{1}{2\pi}. \quad (5.7)$$

Note that for the unsynchronised system, this measure vanishes; the true probability would be a flat distribution at $P(\varphi) = \frac{1}{2\pi}$ that obeys $\int_0^{2\pi} d\varphi P(\varphi) = 1$, as was the case in previous chapters. However, the constant term included in Eq. 5.7 shifts this distribution to $p(\varphi) = P(\varphi) - \frac{1}{2\pi} = 0$ for the limit-cycle with no preferred phase.

Although the steady state Q -function is independent of γ^g and γ^d , the way in which the oscillator reacts to perturbations is determined by the ratio of these rates $R = \gamma^g/\gamma^d$.

5.2 Coupled spin-1 oscillators

In this Section, we consider networks of coupled spin-1 oscillators. We start by discussing coherent coupling between spins and then show how synchronisation can be observed with a relative phase distribution calculated from a two-spin Husimi-Q function. We analyse the set of relative phase distributions of each pair of oscillators to explore how synchronisation manifests in a variety of network geometries and sizes.

5.2.1 Coupling geometries

We consider a set of N spin-1 oscillators coupled via a coherent interaction [100]. The dynamics of this network is described by the master equation

$$\dot{\hat{\rho}} = \sum_{j=1}^N \left(\mathcal{L}_j \hat{\rho} - i \sum_{k>j}^N \left[\hat{H}_{jk}, \hat{\rho} \right] \right), \quad (5.8)$$

where the dissipation term \mathcal{L}_j for each oscillator j follows from Eq. 5.5 and the exchange Hamiltonian between the j^{th} and k^{th} oscillator is

$$\hat{H}_{jk} = \frac{\epsilon_{jk}}{2} \left(\hat{S}_j^+ \hat{S}_k^- + \text{h.c.} \right), \quad (5.9)$$

where ϵ_{jk} are the (real) elements of the coupling matrix and we now use operators \hat{S}_j^α that are the spin-1 operators $\hat{\sigma}^\alpha$ acting on the j^{th} oscillator in the network.

As the coupling strength between two spins can be engineered to be distance dependent, the coupling matrix can be thought of in terms of the geometry of the network, i.e. the oscillators close enough to each other have nonzero coupling of the form Eq. 5.9. We consider three equilateral network geometries, schematics of which are illustrated in Fig. 5.2, which we label *chain*, *ring*, and *all-to-all*.

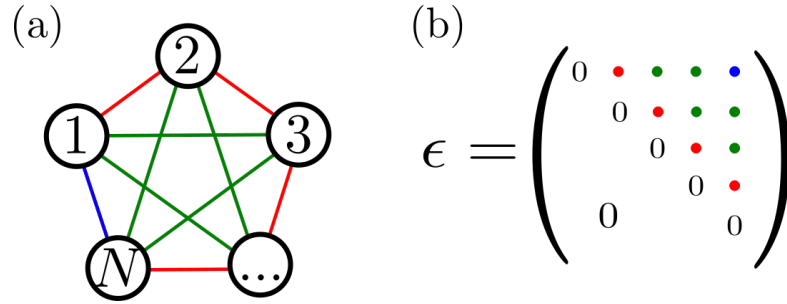


Figure 5.2: (a) The coloured links defining different network geometries with (b) associated coupling matrix in Eq. 5.9 for the three geometries that we consider for our network of N spin-1 oscillators. A chain configuration couples oscillators (a) linked by red lines with (b) nonzero coupling strengths shown in red, $\epsilon_{j,j+1} > 0$, $\forall j$. A ring geometry is a chain with the additional (a) blue link that closes the loop and so (b) the blue coupling term is nonzero ϵ_{1N} . The all-to-all geometry couples each oscillator with every other oscillator and is shown with (a) the red, blue, and green lines and consequently (b) the red, green, and blue nonzero coupling strengths, $\epsilon_{j,k}$, $\forall j < k$.

Including only couplings between oscillators j and $j + 1$ (red lines) creates a chain geometry, where the only nonzero elements of the coupling matrix are on the first off-diagonal $\epsilon_{j,j+1} \neq 0$. A ring geometry adds one more link to the chain, between the first and N th oscillator (blue line) $\epsilon_{1N} \neq 0$. Finally, the all-to-all network couples every oscillator with every other oscillator (red, blue and green lines), filling the upper triangle of the coupling matrix $\epsilon_{jk} \neq 0$ where $k > j$.

5.2.2 Husimi-Q relative phase distribution

There are many quantities that we could analyse to explore synchronisation in a network of coupled spins. In previous chapters, we have concentrated on the relative phase distribution; for two weakly coupled spin-1 oscillators, this is often π - or 2π -periodic, as shown in Fig. 5.3a. If we aim to explore networks of many spins, though, attempting to analyse a collection of distributions, one for each pair of oscillators, would be difficult; a simpler measure is required.

We previously described the visibility (Eq. 2.3), a single value parameter, shown for

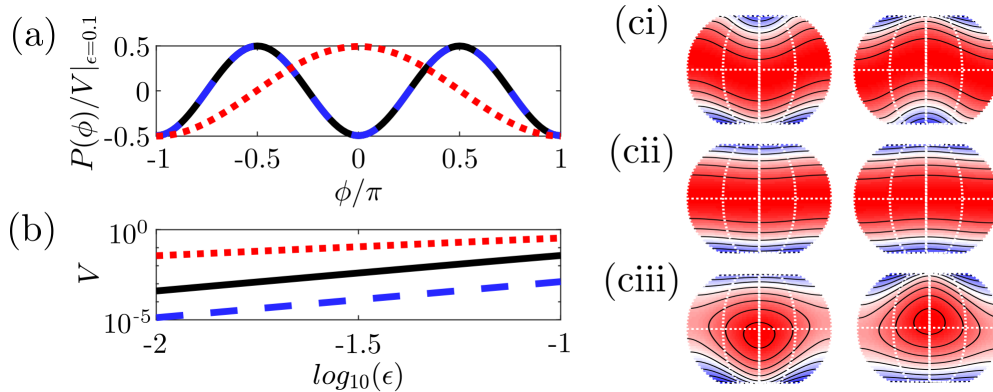


Figure 5.3: (a) Relative phase distributions (scaled with visibility) of two weakly coupled ($\epsilon = 0.1$) spin-1 oscillators. (b) The visibility (Eq. 2.3) of distributions for a range of coupling strengths ϵ . (c) Husimi-Q functions of both oscillators with (ci) $R_1 = R_2 = 1$, (cii) $R_1 = R_2 = 10$, and (ciii) $R_1 = R_2^{-1} = 10$ which correspond to the curves in (a) and (b) in solid black, dashed blue, and dotted red, respectively.

a range of coupling strengths in Fig. 5.3b. However, the visibility only measures the strength of the synchronisation, and loses all information on the phase preference. The Husimi-Q function (see Eq. 5.2) can analytically describe the phase of each of the oscillators, as shown in Fig. 5.3c. The problem is that we are interested in the *relative* phase; additionally, this measure is even more complicated than the relative phase distribution. We now show that we can find a simple form of the relative phase distribution by integrating a two-spin version of the Husimi-Q function.

The Husimi-Q function (Eq. 5.2) for a pair of oscillators j and k [100]

$$Q(\theta_j, \theta_k, \varphi_j, \varphi_k) = \left(\frac{3}{4\pi}\right)^2 \langle \theta_j, \theta_k, \varphi_j, \varphi_k | \hat{\rho}_{jk} | \theta_j, \theta_k, \varphi_j, \varphi_k \rangle, \quad (5.10)$$

where the two spin coherent state $|\theta_j, \theta_k, \varphi_j, \varphi_k\rangle = |\theta_j, \varphi_j\rangle \otimes |\theta_k, \varphi_k\rangle$ is obtained from Eq. 5.1. The reduced density matrix $\hat{\rho}_{jk}$ describe any pair of oscillators by

tracing out the remaining $N - 2$ spins

$$\hat{\rho}_{jk} = \text{Tr}_{jk}[\hat{\rho}]. \quad (5.11)$$

We then substitute the relative phase, $\phi = \varphi_j - \varphi_k$ where the subscripts are inferred through context, into Eq. 5.10. By then integrating over all other angles, we find an analytical expression for the relative phase distribution $P_{jk} = P(\phi) = P(\varphi_j - \varphi_k)$ (see App. D for details)

$$P_{jk} = -\frac{1}{2\pi} + \int_0^{2\pi} d\varphi_k \int_0^\pi d\theta_j \int_0^\pi d\theta_k \sin\theta_j \sin\theta_k Q(\theta_j, \theta_k, \phi + \varphi_k, \varphi_k) \quad (5.12)$$

$$\begin{aligned} &= \pi \left(\frac{3}{16}\right)^2 \left(\langle \hat{\sigma}_+ \otimes \hat{\sigma}_- \rangle e^{-i\phi} + \langle \hat{\sigma}_- \otimes \hat{\sigma}_+ \rangle e^{i\phi} \right) \\ &\quad + \frac{1}{8\pi} \left(\langle \hat{\sigma}_+^2 \otimes \hat{\sigma}_-^2 \rangle e^{-2i\phi} + \langle \hat{\sigma}_-^2 \otimes \hat{\sigma}_+^2 \rangle e^{2i\phi} \right). \end{aligned} \quad (5.13)$$

$$= \pi \left(\frac{3}{16}\right)^2 \left\langle \hat{S}_j^+ \hat{S}_k^- \right\rangle e^{-i\phi} + \frac{1}{8\pi} \left\langle \hat{S}_j^+ \hat{S}_j^+ \hat{S}_k^- \hat{S}_k^- \right\rangle e^{-2i\phi} + \text{c.c.} \quad (5.14)$$

Note that Eq. 5.14 is written in terms of \hat{S} operators that act on the full density matrix $\hat{\rho}$ and not the tensor product of two σ operators that act on the reduced density matrix $\hat{\rho}_{jk}$. This means that the relative phase distribution between two spins can be calculated directly from the full density matrix of the network. A similar technique has been used in the context of harmonic oscillators [25, 49] and can be calculated with a different scaling by truncating to the lowest 3 states [53]. By rewriting the exponentials in Eq. 5.13 in trigonometric form, we arrive at an analytical equation for the relative phase distribution between any two oscillators j and k

$$P_{jk} = A_{jk}^r \cos \phi + A_{jk}^i \sin \phi + B_{jk}^r \cos 2\phi + B_{jk}^i \sin 2\phi \quad (5.15)$$

with complex Fourier coefficients

$$A_{jk} = A_{jk}^r + iA_{jk}^i = 2\pi \left(\frac{3}{16}\right)^2 \langle \hat{S}_j^+ \hat{S}_k^- \rangle, \quad (5.16)$$

$$B_{jk} = B_{jk}^r + iB_{jk}^i = \frac{1}{4\pi} \langle (\hat{S}_j^+ \hat{S}_k^-)^2 \rangle. \quad (5.17)$$

This result is particularly useful for two reasons. The Fourier coefficients in Eq. 5.17 can be calculated directly from the full density matrix without requiring a partial trace which greatly speeds up computation times. Also, the relative phase distribution in Eq. 5.15 can be fully characterised by four real numbers (per oscillator) which allows us to visualise a full parameter space of distributions in a small number of figures. The value these Fourier coefficients take is determined by the ratio of the individual oscillator rates $R_j = \gamma_j^g/\gamma_j^d$, the geometry of the network, and the coupling strengths ϵ_{jk} ($j \neq k$).

This Fourier coefficient form of the relative phase distribution is similar to our calculations in previous chapters but proved far simpler in the spin-1 case. With this simple but exact measure, we go beyond the recent work on spin-1 oscillators that utilised first order perturbation theory [57], and find novel synchronisation regimes.

5.3 Spin-1 networks

Having established techniques to measure the synchronisation of a pair of spin-1 oscillators within an N -spin network, we start analysing networks. We will describe the relative phase distributions by analysing the behaviour of A_{12} and B_{12} , revealing a rich variety of synchronisation regimes. We will also explore entanglement and the limit-cycle deformation in these regimes. Increasing the number of oscillators in the network then allows us to explore the effect network

geometry has on the synchronisation.

5.3.1 Two oscillators

The smallest network, consisting of just two oscillators, can only be coupled in one unique geometry where the coupling matrix in Eq. 5.9 includes a single, nonzero term $\epsilon_{12} = \epsilon$. Nevertheless, the spectrum of synchronisation features found is incredibly rich. By tuning the system parameters, the peaks of the relative phase distribution can be moved to any value, i.e. any desired relative phase preference can be engineered in the coupled spin-1 system. Generally, the relative phase distribution is 2π -periodic, though π -periodic regimes are also found.

As synchronisation effects are perturbative [86] and appear for arbitrarily small coupling strengths, we again begin in the limit of weak coupling $\epsilon = 0.1$ and vary the gain/damp rates $R_j = \gamma_j^g/\gamma_j^d$ for each of the two oscillators $j = 1, 2$. To ensure that the coupling can be considered weak, we will observe the states of the oscillators to check if the interaction is perturbative. Analysing the real and imaginary parts of the Fourier coefficients Eq. 5.17 reveals $A_{12}^r, B_{12}^i = 0$ for any choice of parameters which is a consequence of the form of the interaction in Eq. 5.9 following the same reasoning as in Chapter 4 (see App. B). A_{12} is therefore purely imaginary and, as shown in Fig. 5.4a, reaches magnitudes of $\max(|A_{12}|) \approx 3 \times 10^{-2}$. Similarly, B_{12} is purely real, positive definite, and reaches magnitudes of $\max(|B_{12}|) \approx 10^{-3}$, as shown in Fig. 5.4b. These results reduce the relative phase distribution in Eq. 5.15 to

$$P_{12} = A_{12}^i \sin \phi + |B_{12}^r| \cos 2\phi \quad (5.18)$$

for the two weakly coupled spin-1 oscillators. Note that the modulus sign in Eq. 5.18 is to emphasise that the $\cos 2\phi$ will never invert since B_{12}^r is positive

definite.

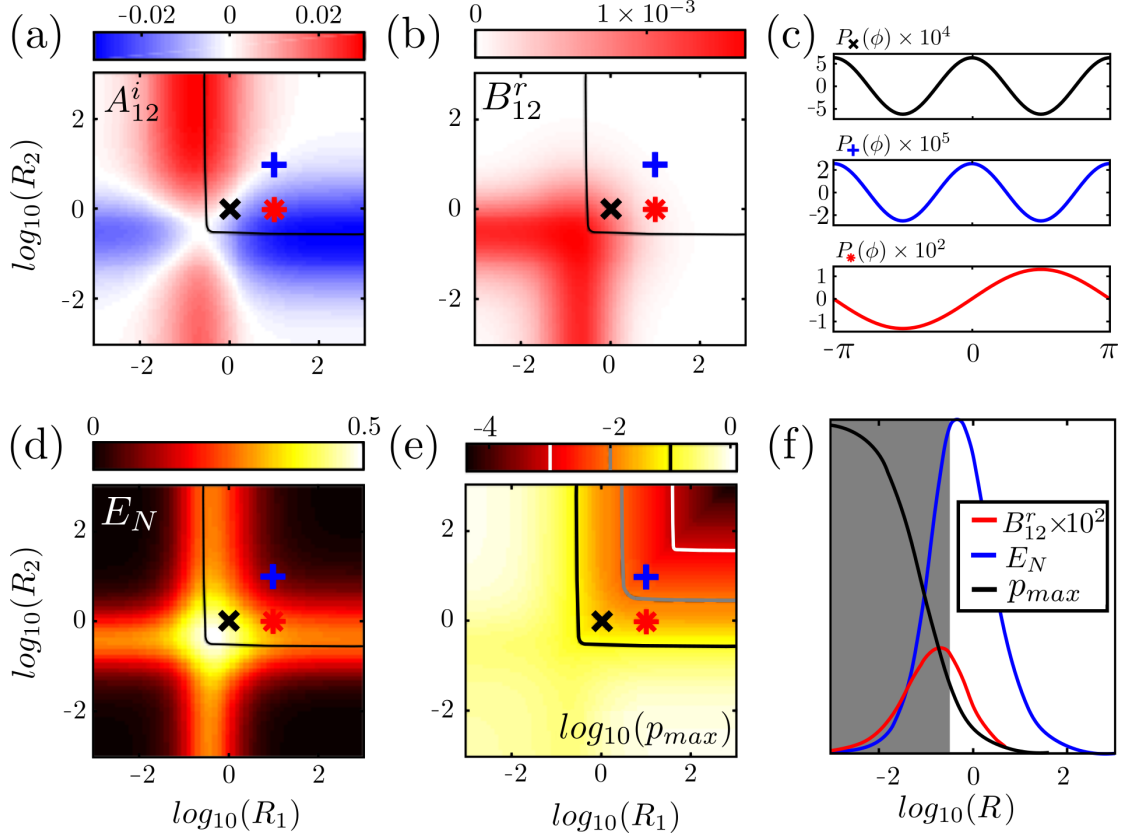


Figure 5.4: The nonzero Fourier coefficients (a) A_{12}^i and (b) B_{12}^r that determine the relative phase distribution of two weakly coupled ($\epsilon = 0.1$), spin-1 oscillators. (c) The relative phase distributions corresponding to the parameters indicated by a black cross ($R_1 = R_2 = 1$), blue plus ($R_1 = R_2 = 10$), and red star ($R_1 = 10$, $R_2 = 1$). (d) The logarithmic negativity (Eq. 2.6) acting as an entanglement witness and (e) the limit-cycle deformation measure Eq. 5.6 with contours at $p_{max} = 0.1$ (black, also shown on other figures), 0.01 (grey), and 0.001 (white). (f) For the identical oscillator case ($R = R_1 = R_2$), the synchronisation strength (B_{12}^r red) and entanglement Eq. 2.6 (blue) are shown to appear before the limit-cycle deformation Eq. 5.6 (black) is large. The strongly deformed regime $p_{max} \geq 0.1$ is highlighted in grey.

Figures 5.4a and b show that arbitrarily chosen R_1 and R_2 generally leads to $|A_{12}^i| \gg |B_{12}^r|$ and therefore Eq. 5.18 simplifies to $P_{12} = A_{12}^i \sin \phi$ which is 2π -periodic a peak at $-\frac{\pi}{2}$ or $\frac{\pi}{2}$ for positive or negative A_{12}^i , respectively. For example, the parameters $R_1 = 10$ and $R_2 = 1$ (red star) produce a distribution with $A_{12}^i =$

-0.01 , shown in the bottom panel of Fig. 5.4c, and a relative phase preference of $\frac{\pi}{2}$. Exchanging the two oscillators, $R_1 \leftrightarrow R_2$, simply changes the sign of A_{12} leading to a relative phase preference of $-\frac{\pi}{2}$.

There are some notable regions in Fig. 5.4a where the 2π -periodic term passes through zero (white area) and $|A_{12}| \ll |B_{12}|$, where the relative phase distribution becomes π -periodic, $P_{12} = |B_{12}^r| \cos 2\phi$. Since $B_{12} \geq 0$, this regime always exhibits a relative phase preference of 0 and π . Interestingly, identical oscillators $R_1 = R_2$ fall into this regime; a somewhat overlooked case if only first order synchronisation effects are measured [60, 61]. Two examples are shown in the top and middle panels of Fig. 5.4c (with parameters indicated by the black cross and blue plus, respectively) where the choice of parameters only changes the amplitude of the relative phase distribution and not the location of its peaks. It is important to note that the visibility (Eq. 2.3) of the identical oscillator distributions (black and blue) in Fig. 5.4c are at least two orders of magnitude smaller than those possible with $R_1 \neq R_2$ (red).

We find entanglement in this network (see Sec. 2.1.2) in similar regions that produce strong synchronisation effects, shown in Fig. 5.4d, possibly indicating a link between the two phenomena. However, the logarithmic negativity reaches its maximum in a parameter regime with particularly weak synchronisation ($R_1 = R_2 \approx 0.44$). This result supports the view that entanglement and synchronisation are not necessarily tightly linked (see Sec. 2.1.2) and, in this system, we cannot use entanglement as a synchronisation measure.

The limit-cycle deformation Eq. 5.6 is shown in Fig. 5.4e with contours at 10% (solid), 1% (dashed), and 0.1% (dotted) deformation. The first contour is also included on the other phase diagrams to suggest a boundary at which the limit-cycles of each oscillator are significantly damaged by the coupling. Figure 5.4f

shows that the synchronisation (red) and entanglement (blue) generation for the identical oscillators $R = R_1 = R_2$, i.e. the diagonal of Figs. 5.4a-d, as well as the deformation (black). Though all three quantities grow in the same region, synchronisation and entanglement are seen to appear before the limit-cycle becomes significantly deformed (grey region indicates $p_{max} \geq 10^{-1}$).

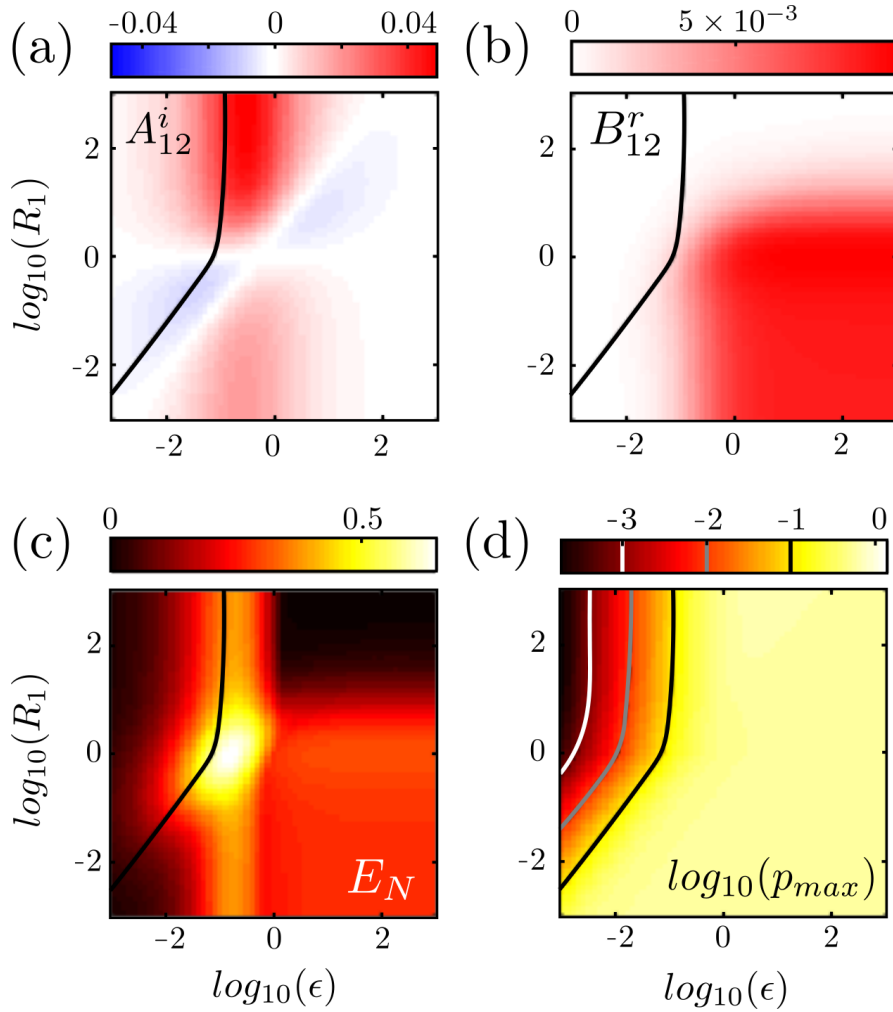


Figure 5.5: Two coupled spin-1 oscillators with the second dissipation ratio fixed to $R_2 = 1$. The nonzero Fourier coefficients (a) A_{12}^i and (b) B_{12}^r that determine the relative phase distribution in Eq. 5.18. (c) The entanglement (logarithmic negativity) and (d) limit-cycle deformation measures are also included. All figures have the contour of 10% deformation in black.

Next we turn our attention to the impact of the coupling strength on the two-

spin system. Figure 5.5 shows A_{12}^i , B_{12}^r , E_N , and p_{max} as a function of the coupling strength, ϵ , and the oscillator ratio R_1 while keeping the other fixed at $R_2 = 1$. The results are similar to Fig. 5.4, $A_{12}^r, B_{12}^i = 0$ and $B_{12}^r \geq 0$, thus the predicted relative phase distribution is of the form Eq. 5.18. Unlike the previous case (Fig. 5.4a), however, there is no symmetry along the diagonal of Fig. 5.5a. This is because ϵ and R_1 control the rates of a *coherent* exchange process and a *dissipative* relaxation process, respectively, therefore we do not expect a 1:1 correspondence. Again, A_{12}^i dominates for the majority of parameter choices, but there exist regimes where B_{12} dominates (e.g., the line where $R_1 = 1 = R_2$). The logarithmic negativity, Eq. 2.6, is shown in Fig. 5.5c. Again, entanglement is predicted for the synchronised regimes, but is maximal for identical oscillators with $\epsilon \approx 0.15$ where synchronisation is weak. All four figures include the contour indicating 10% limit-cycle deformation (solid black line) with the full range of values shown in Fig. 5.5d.

Finally, we focus on the case of two identical oscillators and vary the coupling strength ϵ and the common oscillator ratio $R = R_1 = R_2$. Although other parameter regimes produce a larger synchronisation effect, this regime is particularly interesting as previous research stopped at first order perturbation effects [100] and so failed to identify the features we measure. As found in the previous two cases, the normally dominant (in most $R_1 \neq R_2$ regimes) A_{12} is zero for any choice of ϵ and R . Therefore, only one term in Eq. 5.13 is nonzero, the positive definite B_{12}^r , which takes the values shown in Fig. 5.6a and results in a relative phase distribution of

$$P_{12} = |B_{12}^r| \cos 2\phi \quad (5.19)$$

with relative phase preference of 0 and π .

The logarithmic negativity, Eq. 2.6, shows (see Fig. 5.6b) that the emergence of

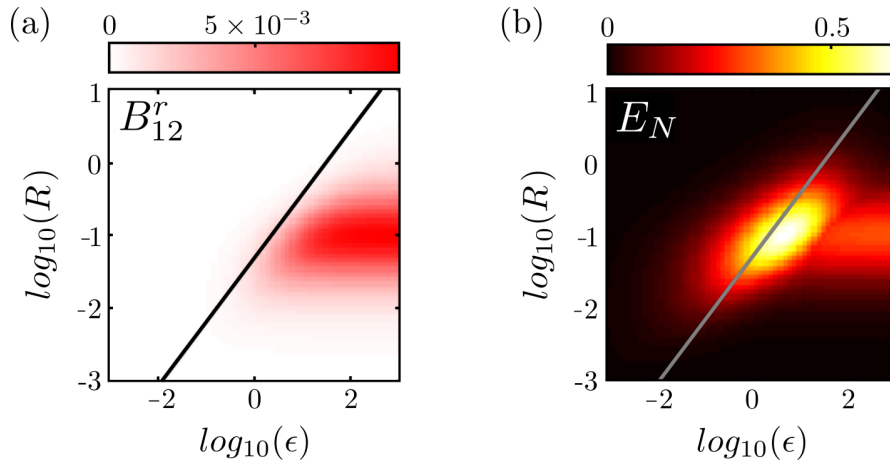


Figure 5.6: (a) The only nonzero Fourier coefficient B_{12}^r of the relative phase distribution Eq. 5.19 of two identical spin-1 oscillators, with common oscillator ratio $R = R_1 = R_2$ coherently coupled with strength ϵ . (b) The logarithmic negativity (entanglement witness) showing some correspondence with the emergence of synchronisation, though certainly not identical. The solid line indicates the 10% limit-cycle deformation contour (Eq. 5.6).

synchronisation is often accompanied by entanglement and both appear in regimes where the limit-cycle is relatively well preserved (the black line shows the 10% deformation contour). However, we again find that entanglement cannot be used as a measure of synchronisation as the two measures are far from identical.

Now that we have an understanding of the features of coupled spin-1 oscillators, we increase the size of the network.

5.3.2 Three oscillators

Introducing a third spin-1 oscillator allows us to begin exploring how network geometry affects synchronisation. We will now have three relative phase distributions to analyse, P_{12} , P_{23} , and P_{13} (by tracing out the third, first, and second oscillator, respectively). Though, in principal a network consisting of N oscillators will have N oscillator ratios and $(N - 1)!$ coupling strengths, we simplify the problem and reduce this to just two system parameters. First, we consider

identical oscillators by defining a single common oscillator ratio $R_j = R \forall j$. This regime is particularly interesting to us as the small synchronisation features found between two identical oscillators may develop into more significant effects with the introduction of more oscillators. Secondly, we restrict the networks to have equidistant nodes, i.e. every nonzero coupling strength (defined by the geometry of the network) between each pair of oscillators takes the same value ϵ . This aids us in reducing the number of unique results brought about by the inherent symmetries of the equilateral geometries. A network of three oscillators can be configured in the two geometries shown in Fig. 5.7.

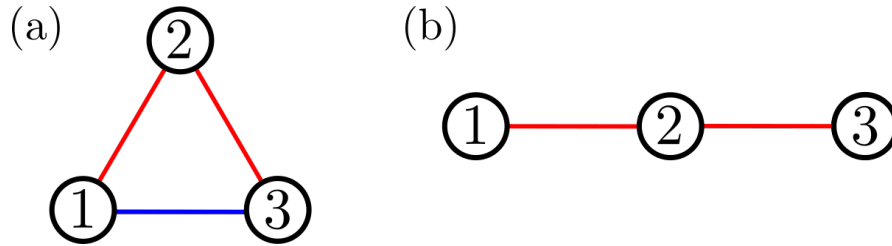


Figure 5.7: The (a) all-to-all (or ring), and (b) chain geometries of the three spin-1 oscillator network. The coloured lines indicate which of the oscillators are directly coupled by the interaction Hamiltonian in Eq. 5.9. The only nonzero terms in the coupling matrix are (a) the upper triangle ($\epsilon_{12} = \epsilon_{23} = \epsilon_{13} = \epsilon$) or (b) the first off diagonal ($\epsilon_{12} = \epsilon_{23} = \epsilon$).

The simplest equilateral geometry to consider is a network with *all-to-all* coupling (in this case, equivalent to the ring network), shown in Fig. 5.7a, where each node is coupled to every other node with the same strength. This geometry leads to an inherent symmetry in the network where each oscillator should behave identically, thus producing identical A_{jk} and B_{jk} values $\forall j, k$.

Varying the oscillator ratio R and coupling strength ϵ reveals that a network of three identical spin-1 oscillators are able to strongly synchronise with a symmetric

relative phase distribution

$$P_{jk} = A_{12}^r \cos \phi + |B_{12}^r| \cos 2\phi \quad (5.20)$$

for any pair of oscillators $j < k$. We do indeed find the expected symmetry and therefore only show one pair of coefficients A_{12}^r and B_{12}^r in Fig. 5.8. An important result is immediately found in the nonzero A_{12}^r component, shown in Fig. 5.8a, which contrasts the results of the two identical spin-1 oscillators where this value was always 0. A rich range of different regimes can be found, including cases where peaks in the relative phase distribution occur at 0 (dominant $A_{12}^r > 0$, e.g. plus), π (dominant $A_{12}^r < 0$, e.g. cross), 0 and π (dominant $B_{12}^r > 0$, e.g. star), though many other values are possible when both terms contribute significantly. Not only do we find synchronisation between the identical oscillators, but the visibility (Eq. 2.3) is comparable to that found in the system of just two oscillators, even with very different gain/loss ratios $R_1 \gg 100R_2$, shown in Fig. 5.5. We again find that the synchronisation and entanglement (Fig. 5.8d) emerge in the system before the limit-cycles deform significantly (Fig. 5.8e). Though, as usual, they do not follow precisely the same pattern.

The other possible geometry of the $N = 3$ network is the chain, where we remove the third coupling term $\epsilon_{13} = 0$, as shown in Fig. 5.7b. We now expect a symmetry between P_{12} and P_{23} and possibly a different P_{13} distribution.

We find a relative phase distribution between nearest neighbours

$$P_{12} = P_{32} = A_{12}^i \sin \phi + |B_{12}^r| \cos 2\phi \quad (5.21)$$

with the behaviour of the coefficients shown in Fig. 5.9a-b, and between the next-

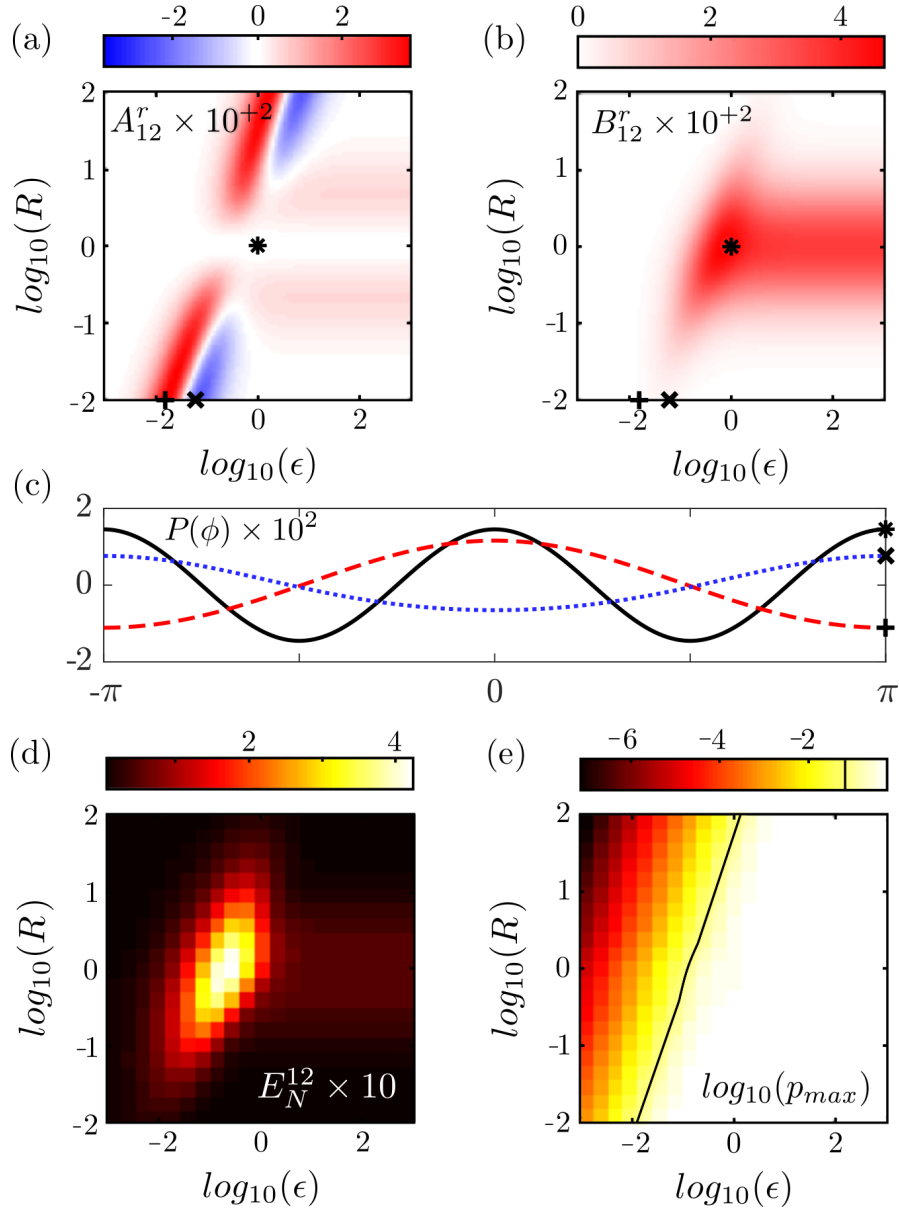


Figure 5.8: The nonzero Fourier coefficients (a) $A_{12}^r = A_{23}^r = A_{13}^r$ and (b) $B_{12}^r = B_{23}^r = B_{13}^r$ of the relative phase distribution Eq. 5.20 between any two spin-1 oscillators in a three spin-1, all-to-all (or ring) network with common dissipation ratios R and coupling strengths ϵ . (c) Example relative phase distributions for parameters given by (black solid curve) star, (red dashed curve) plus, and (blue dotted curve) star. Also shown is (d) the logarithmic negativity Eq. 2.6 which predicts entanglement when $E_N > 0 \forall \epsilon, R$ and (e) the limit-cycle deformation Eq. 5.6 with contour at 0.1.

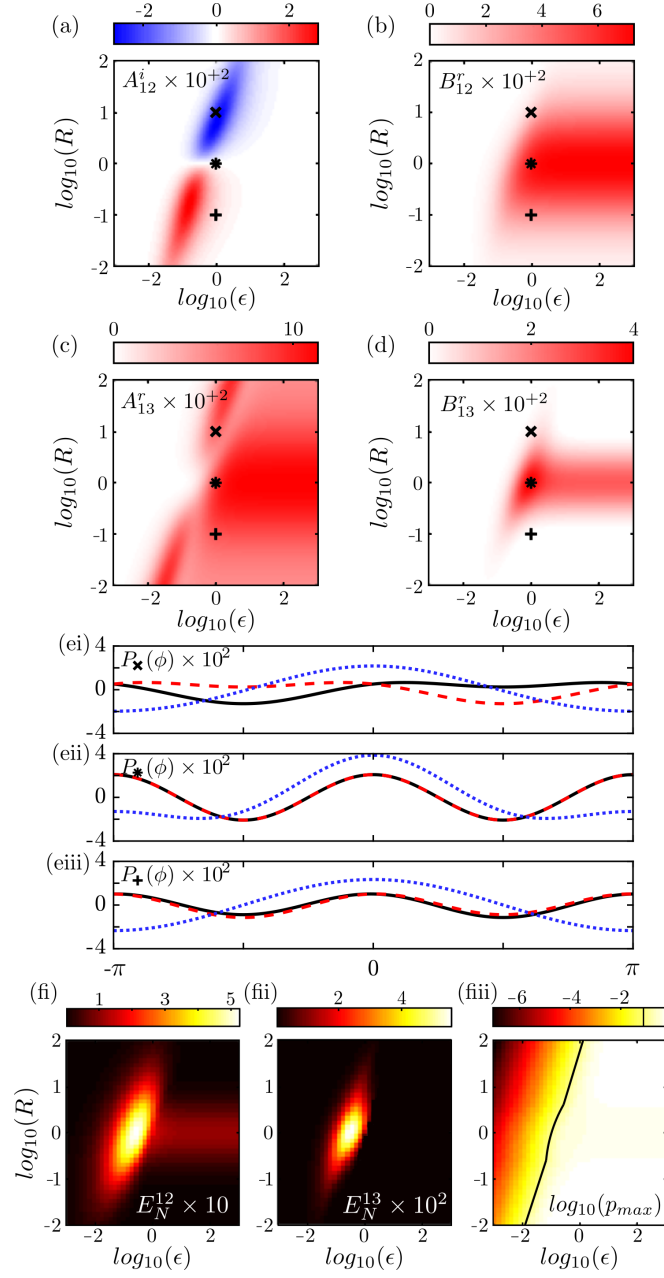


Figure 5.9: Three spin-1, chain coupled network. The nonzero Fourier coefficients (a) $A_{12}^i = -A_{23}^i$, (b) $B_{12}^r = B_{23}^r$, (c) A_{13}^r , (d) B_{13}^r . (e) Shows example relative phase distributions (black solid curve) P_{12} , (red dashed curve) P_{23} , and (blue dotted curve) P_{13} of two spin-1 oscillators with common dissipation ratios R and coupling strengths ϵ with parameters indicated with (ei) a cross, (eii) a star, and (eiii) a plus. The entanglement (Eq. 2.6) between (fi) nearest neighbours $E_N^{12} = E_N^{23}$, and (fii) chain ends E_N^{13} , along with (fiii) the largest limit-cycle deformation in the network (Eq. 5.6) with contour at 0.1.

nearest neighbours

$$P_{13} = [|A_{13}^r| \cos \phi + |B_{13}^r| \cos 2\phi] \quad (5.22)$$

with coefficients' behaviour shown in in Fig. 5.9c-d. Again, the neighbouring identical oscillators have comparable synchronisation strength to the non-identical oscillator case. Surprisingly, synchronisation in the $N = 3$ network is stronger between the ends of the chain than between neighbouring spins with maximum visibilities, from Eq. 2.3, $\max(V_{13}) > \max(V_{12}, V_{23})$, despite not being directly coupled. This reveals that the geometry of the network has a profound effect on the dynamics and suggests that synchronisation effects can be altered and even amplified by intelligent engineering.

5.3.3 Larger networks

With a network of 4 oscillators or more, all three configurations are possible, as shown in Fig. 5.10; an (a) all-to-all, (b) ring, or (c) chain network. As we consider larger and larger networks, we expect the number of Fourier coefficients to quickly become unmanageable and the results will be harder to interpret. Regardless of

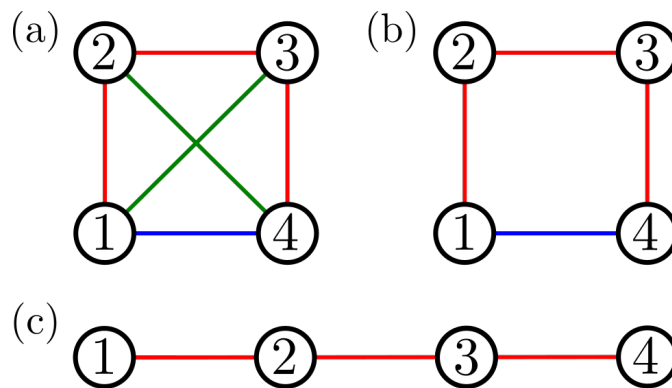


Figure 5.10: Schematic of an $N = 4$ network configured with (a) all-to-all, (b) ring, or (c) chain geometry. The coloured lines indicate which oscillators are directly coupled; just the red lines for the chain, add the blue line for the ring, and finally include the green lines for the all-to-all.

the number of spins, however, we still expect only one, unique set of A_{jk} and B_{jk} complex values in the all-to-all network, due to the inherent symmetries of the system.

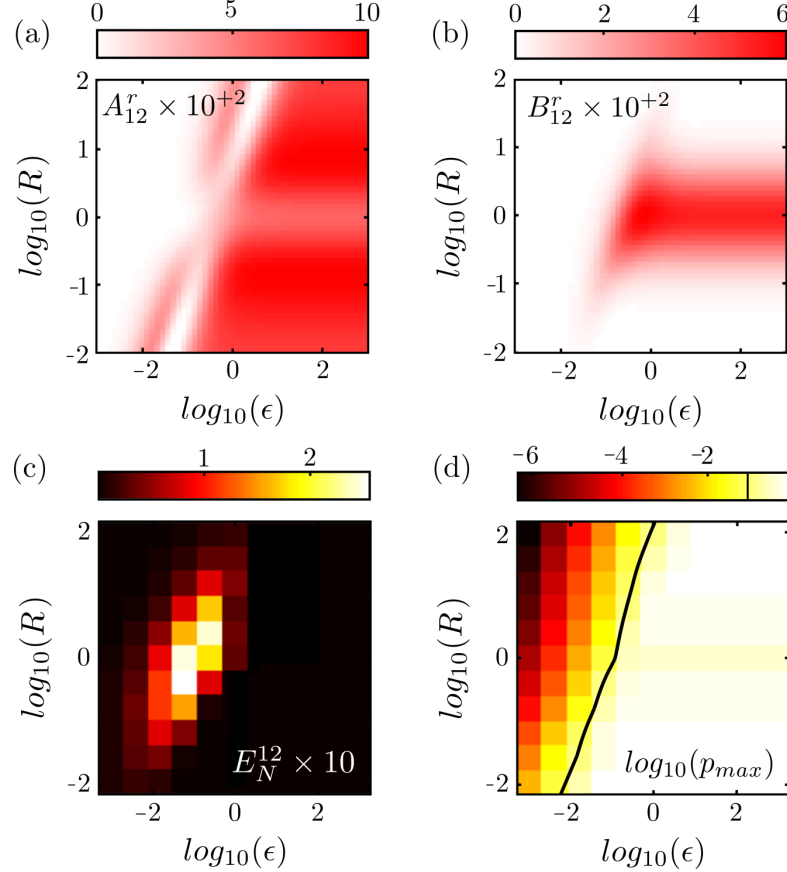


Figure 5.11: The only unique, nonzero Fourier components (a) $A_{j,k} = A_{12}$ and (b) $B_{j,k} = B_{12}$ for the four spin-1, all-to-all network. Each pair of oscillators has the same relative phase distribution, Eq. 5.23, with peaks at either $\phi = 0$ or at 0 and π , depending on which component dominates. Also shown are (c) the logarithmic negativity and (d) limit-cycle deformation with contour at 0.1.

Again, we find strong synchronisation between each pair of oscillators in the all-to-all network, with relative phase distribution

$$P_{jk} = [|A_{12}^r| \cos \phi + |B_{12}^r| \cos 2\phi], \quad (5.23)$$

with terms shown in Fig. 5.11. The relative phase distribution in Eq. 5.23 reaches

a maximum visibility with $\max(A_{12}^r) \approx 0.1$ and is symmetric with a peak at 0 and, in regimes when B_{12}^r is large, another peak at π .

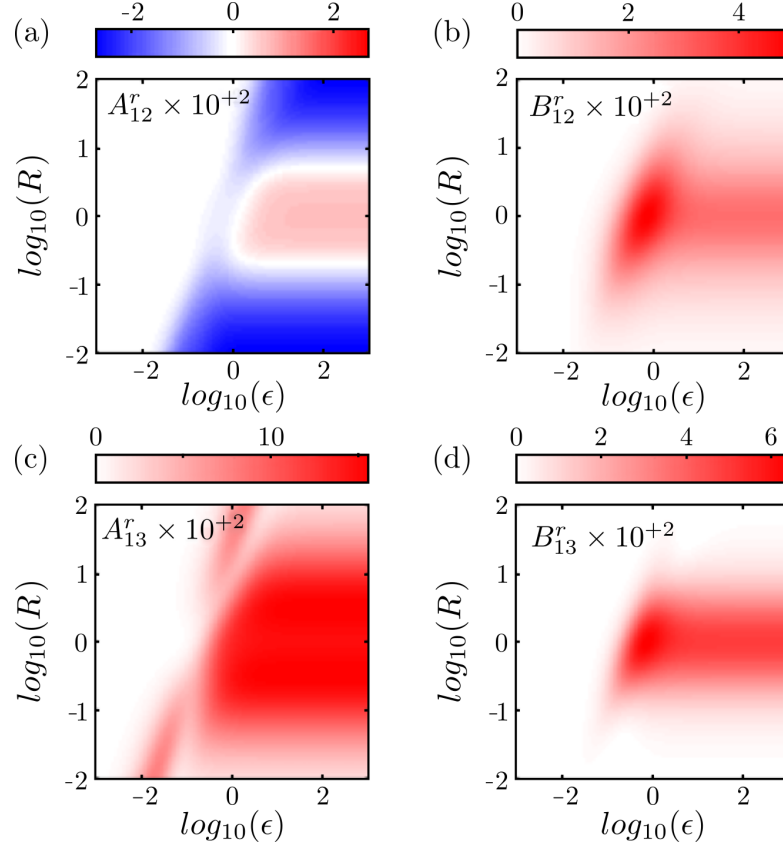


Figure 5.12: The four spin-1, ring coupled network has a relative phase distribution between two neighbouring oscillators (Eq. 5.24) with nonzero Fourier coefficients (a) A_{12}^r and (b) B_{12}^r . Between next-nearest neighbours, the relative phase distribution is given by Eq. 5.25 with (c) A_{13}^r and (d) B_{13}^r .

Considering the $N = 4$ network with ring geometry (Fig. 5.10b) leads to symmetric distributions between each pair of oscillators that depend on the distance between them. The nearest neighbour oscillators have a relative phase

$$P_{j,j+1} = [A_{12}^r \cos \phi + |B_{12}^r| \cos 2\phi] \quad (5.24)$$

with values of the coefficients behaving as shown in Fig. 5.12a-b. The next-nearest

neighbours, however, have a relative phase

$$P_{j,j+2} = [|A_{13}^r| \cos \phi + |B_{13}^r| \cos 2\phi] \quad (5.25)$$

with the behaviour of the coefficients shown in Fig. 5.12c-d. Again, we find the strongest synchronisation between next-nearest neighbours, even though they are not directly coupled.

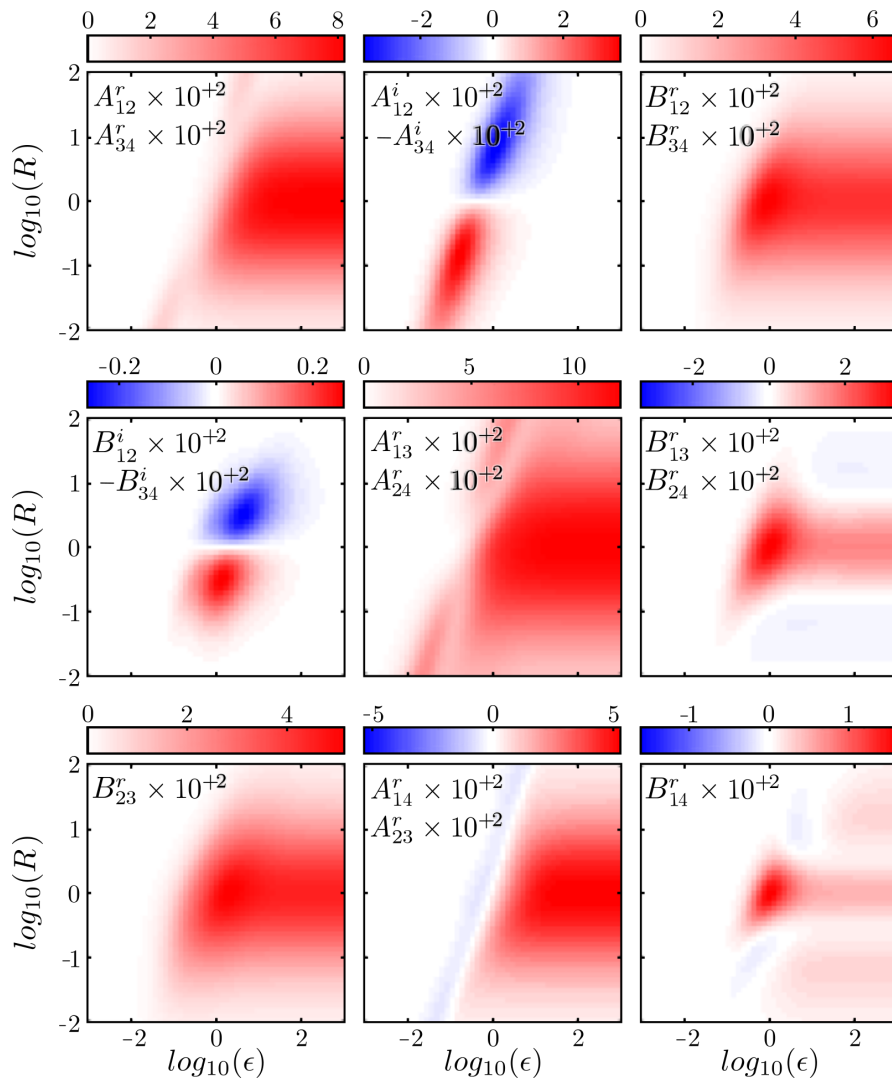


Figure 5.13: Four spin-1, chain coupled network. There are many nonzero Fourier components corresponding to many different relative phase distributions P_{jk} in Eq. 5.15.

As we begin exploring more complex networks, such as the $N = 4$ chain in Fig. 5.10c, the reduction in symmetry works in tandem with the increased size to substantially inflate the number of terms in Eq. 5.13 required to describe the relative phases of the oscillators. There are so many different distributions in the 4-spin chain that analysing all the Fourier coefficients in Fig. 5.13 makes it difficult to see the wood for the trees.

In the following we focus on what seem to be the most important features. The visibilities (Eq. 2.3), estimated by simply reading off Fourier component magnitudes in Fig. 5.13, tell us that synchronisation is strongest between next-nearest neighbours (between oscillator j and $j + 2$), where A_{13}^r and A_{24}^r can be larger than 0.1. A qualitative statement we can make for the chain is that there is still a symmetry between the first and last oscillators, as was the case for 3 oscillators (see Fig. 5.9a-d), so that $P_{12} = P_{43}$.

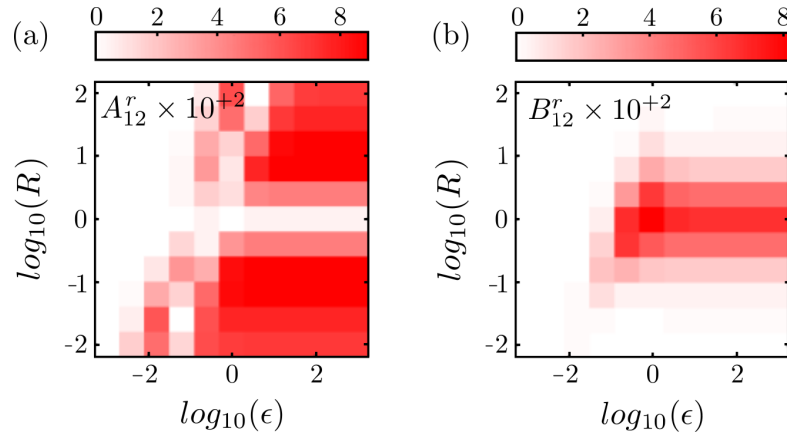


Figure 5.14: Five spin-1, all-to-all coupled network. Any two oscillators have identical relative phase distributions (Eq. 5.23) with peaks at either 0 or 0 and π , depending on which of the two nonzero components, (a) A_{12}^r or (b) B_{12}^r , dominates.

Five spins can also be arranged in the three scenarios of Fig. 5.10, though the set of relative phase distributions for the chain network becomes too large to interpret. The all-to-all coupling produces similar results to the four spin network, with identical relative phase distributions (given by Eq. 5.23) with coefficients that

have slightly smaller values than the 4-spin case, as shown in Fig. 5.14. We expect that increasing the number of oscillators in the all-to-all network will always result in a relative phase distribution defined by Eq. 5.23 with strengths reducing with network size.

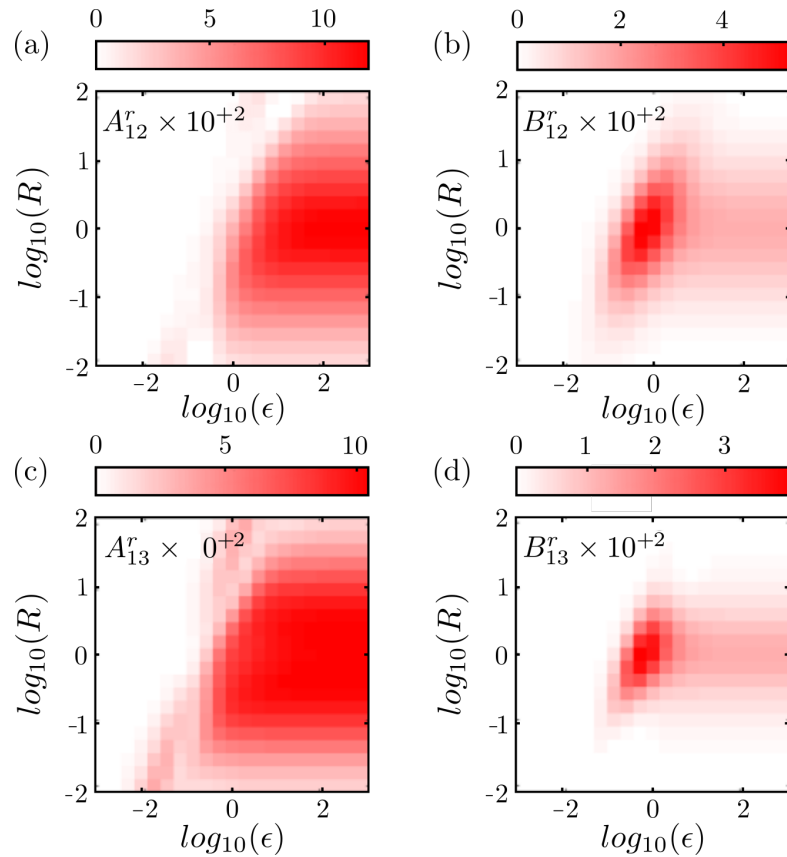


Figure 5.15: Relative phase distributions for the five spin-1 ring network, between two neighbouring oscillators have the form Eq. 5.24 with (a) A_{12}^r and (b) B_{12}^r . Next-nearest neighbours have a different distribution of Eq. 5.25 with (c) A_{13}^r and (d) B_{13}^r .

Similarly, the $N = 5$ ring has the same relative phase distributions as the $N = 4$ ring (Eqs. 5.24-5.25) but with positive definite A_{12}^r and the Fourier coefficients in this case are shown in Fig. 5.15.

The strength of the nearest and next-nearest neighbour synchronisation is shown in Fig. 5.16, in blue and red respectively. The synchronisation strength for each ge-

ometry initially grows with increasing network size N , before dropping or plateauing. Some networks, such as the $N = 4$ chain in Fig. 5.16b and the $N = 3$ and 4 chains in Fig. 5.16c, show stronger synchronisation for (red) next-nearest neighbours compared to (blue) nearest neighbours.

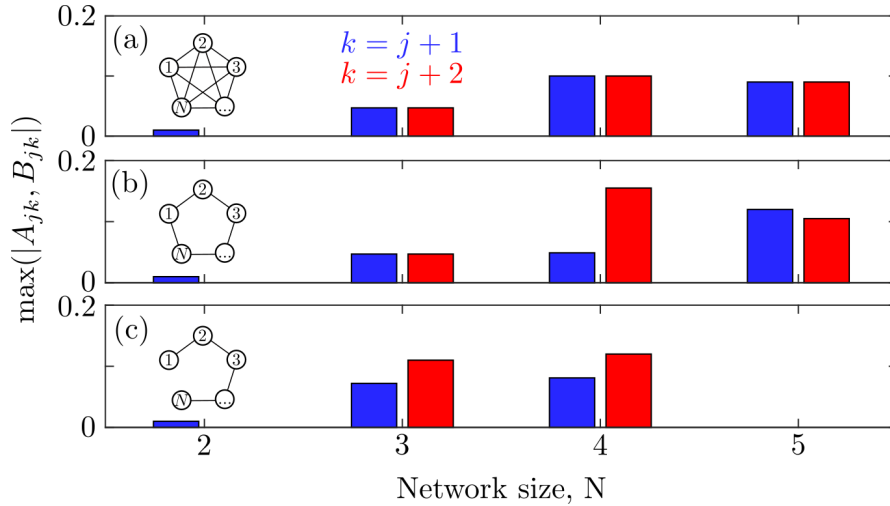


Figure 5.16: The maximum magnitude Fourier coefficient A_{jk} or B_{jk} of (blue) the nearest neighbours, $k = j + 1$, and (red) next-nearest neighbours, $k = j + 2$, for networks of N spin-1 oscillators in (a) all-to-all, (b) ring, and (c) chain geometries.

5.4 Conclusion

In this chapter, we developed exact relations that describe the relative phase distributions between pairs of spin-1 oscillators in large networks. We gained a deep understanding of how synchronisation emerges in a large variety of networks through use of a novel form of the relative phase distribution that makes a previously cumbersome data set far more manageable. We derived an analytic form of the relative phase distribution that depends on only two complex values. This was used to show that two identical spin-1 oscillators do synchronise, though very weakly.

Increasing the size of the network to include 3 oscillators strengthens synchronisation and showed differences resulting from geometry choice. In a 3-spin chain, we found that synchronisation between the uncoupled ends was stronger than between the directly coupled neighbours. This synchronisation strengthening for next-nearest neighbours was also found in some of the larger ring and chain networks. We also presented exact equations for the relative phase distributions for every network size and geometry and found a single form that describes any all-to-all network of more than 3 oscillators.

Future work could tackle larger networks and a comparison might be made to the limit of many spins with a mean field argument. More complex geometries or regimes of non-identical oscillators could also be considered, though this would increase the number of parameters which tends to increase the number of results making interpretation difficult. Another direction could be to explore different types of coupling; for example, we only consider real coupling strengths, we expect that imaginary or complex coupling strengths would produce different synchronisation features.

Chapter 6

Summary

Chapters 1 and 2 outline the structure of the thesis and introduce the theoretical concepts and measures that were developed in previous studies of synchronisation that we would utilise in our research with novel models.

In Chapter 3, we began exploring quantum synchronisation beyond the usual limit-cycle regime by first focussing on a trapped ion system that was driven to a bistable state via a novel two-phonon resonant interaction. The high driving regime produces a relative phase preference of 0 and π which corresponds to coupled limit-cycles, as seen in the literature. New results were found in the low driving regime where a relative phase distribution with peaks at $\frac{\pi}{2}$ and $\frac{3\pi}{2}$ was observed. Furthermore, for intermediate driving strengths that produced a bistability, 4-peaked distributions were found (with maxima at 0, $\frac{\pi}{2}$, π , and $\frac{3\pi}{2}$). Similar relative phase distributions were produced by the coupling of a limit-cycle oscillator with a non-lasing oscillator, but a clear link between the two scenarios was difficult to find due to the complexity of the system. This motivated us to develop a simplified model that still produced the interesting relative phase features of the trapped ion system that would allow us to explore how the features originated.

In Chapter 4, we introduced the 321 oscillator; a simple oscillator model with a

two-phonon gain process balanced by one- and three-phonon losses that developed a bistable oscillator state. Quantum jump simulations revealed trajectories with intermittent activities in the bistable regime, signalling that the bistable state is also metastable. The relative phase distribution of two coherently coupled 321 oscillators displayed similar features to those found in the trapped ion model. Specifically, we showed that the preferred phases of $\frac{\pi}{2}$ and $\frac{3\pi}{2}$ originated from particular phonon number distributions that could only develop due to the two-phonon driving process. The 321 oscillator proved to be both considerably simpler than the trapped ion model, allowing us to carry out more accurate analysis and explore a greater parameter range, whilst still being able to display the bistable state we aimed to study.

In Chapter 5, we moved our attention away from pairs of bistable oscillators and instead explored larger networks of significantly smaller, spin-1 oscillators. We gained a deep understanding of how synchronisation emerges in a large variety of networks through use of a novel relative phase measure that makes a previously cumbersome data set far more manageable. We derived an analytic form of the relative phase distribution and with it found weak synchronisation between two identical spin-1 oscillators. We explored the effects of network size and geometry on the synchronisation developing between pairs of spins for chain, ring, and all-to-all networks of various sizes. An interesting strengthening of synchronisation was observed between next-nearest neighbours (compared to nearest neighbours) in chain and ring networks.

Appendix A

Two-phonon resonant driving

The novel two-phonon resonance Hamiltonian in our model is derived from the interaction of the trapped ion with a standing wave laser (Eq. 3.1). Working in the Lamb-Dicke regime [121] assumes that the confining potential of the ion is tight $\eta \ll 1$. This allows us to expand the cos in Eq. 3.1 in orders of η and remove negligible terms. We then move to a rotating frame with the unitary operator $\hat{U} = e^{it(\omega_0 \hat{a}^\dagger \hat{a} + \frac{\Delta}{2} \hat{\sigma}^z)}$. Appropriately choosing the laser detuning $\Delta = -2\omega_0$ and ion position $\chi = 0$ reveals the Hamiltonian

$$\hat{H} = \frac{\Omega}{2} (\cos \chi \cos k\hat{q} - \sin \chi \sin k\hat{q}) \quad (\text{A.1})$$

$$= \frac{\Omega}{4} \left\{ \left[2 + \eta^2 \left((\hat{a}^\dagger)^2 e^{2i\omega_0 t} + \hat{a}^2 e^{-2i\omega_0 t} + 2\hat{a}^\dagger \hat{a} \right) \right] \cos \chi - 2\eta \left(\hat{a}^\dagger e^{i\omega_0 t} + \hat{a} e^{-i\omega_0 t} \right) \sin \chi \right\} (\hat{\sigma}^+ e^{i\Delta t} + \hat{\sigma}^- e^{-i\Delta t}) \quad (\text{A.2})$$

with rescaled driving strength $\Omega = \eta^2 \tilde{\Omega}$. This Hamiltonian is of the anti-Jaynes-Cummings type, as the phonon gain accompanies spin excitation. However, by this precise design, the interaction involves the creation (and annihilation) of two phonons simultaneously.

Appendix B

Perturbation theory for coupled 321 oscillators

B.1 General Method

Perturbation theory provides a convenient method of calculating the way in which the relative phase distribution behaves for weak coupling. The steady state of the uncoupled ($J = 0$), two 321-oscillator system (Eq. 4.23) only has diagonal terms. Treating the coupling as a perturbation [57, 66] allows us to calculate the terms in the first off-diagonal as a function of the uncoupled oscillator terms. Each subsequent off-diagonal can, in turn, be calculated from the previous ones [25].

Writing Eq. 4.23 in the number state basis, with $\rho_{n,m}^{(p)} = \langle n+p, m | \rho | n, m+p \rangle$, leads to a set of simultaneous equations

$$\begin{aligned} \dot{\rho}_{n,m}^{(p)} = & iJ\Delta_{n,m}^{(p)} - (G_n^{(p)} + G_m^{(p)}) \rho_{n,m}^{(p)} \\ & + A_{n+1}^{(p)} \rho_{n+1,m}^{(p)} + B_{n-2}^{(p)} \rho_{n-2,m}^{(p)} + C_{n+3}^{(p)} \rho_{n+3,m}^{(p)} \\ & + A_{m+1}^{(p)} \rho_{n,m+1}^{(p)} + B_{m-2}^{(p)} \rho_{n,m-2}^{(p)} + C_{m+3}^{(p)} \rho_{n,m+3}^{(p)}, \end{aligned} \quad (\text{B.1})$$

with

$$\begin{aligned} \Delta_{n,m}^{(p)} = & -\sqrt{(n+1)(m+p)}\rho_{n+1,m}^{(p-1)} + \sqrt{(m+1)(n+p)}\rho_{n,m+1}^{(p-1)} \\ & -\sqrt{n(m+p+1)}\rho_{n-1,m}^{(p+1)} + \sqrt{m(n+p+1)}\rho_{n,m-1}^{(p+1)}, \end{aligned} \quad (\text{B.2})$$

$$\begin{aligned} G_n^{(p)} = & \frac{1}{2} \left\{ \kappa_1(2n+p) + \kappa_2[(n+p+1)(n+p+2) + (n+1)(n+2)] \right. \\ & \left. + \kappa_3[(n+p)(n+p-1)(n+p-2) + n(n-1)(n-2)] \right\}, \end{aligned} \quad (\text{B.3})$$

$$A_{n+1}^{(p)} = \kappa_1 \sqrt{(n+1)(n+p+1)}, \quad (\text{B.4})$$

$$B_{n-2}^{(p)} = \kappa_2 \sqrt{n(n-1)(n+p)(n+p-1)}, \quad (\text{B.5})$$

$$C_{n+3}^{(p)} = \kappa_3 \sqrt{(n+1)(n+2)(n+3)(n+p+1)(n+p+2)(n+p+3)}. \quad (\text{B.6})$$

In the steady state, this reduces to sets of simultaneous equations with the coupling term, $\Delta_{n,m}^{(p)}$, linking together terms with different p -values. The zeroth-order terms are the diagonal ($p = 0$) elements, the uncoupled probabilities $\rho_{n,m}^{(0)} = P_n P_m$, which necessarily sum to unity. The first-order terms are obtained by substituting the zeroth-order terms into the expression for $\Delta_{n,m}^{(p)}$, leading to nonzero contributions for $p = 1$. This process is continued to higher order in J recursively.

The first-order terms obey the relation $\rho_{m,n}^{(1)} = -\rho_{n,m}^{(1)}$ and hence sum to zero [25], which means that they make no contribution to the relative phase distribution (Eq. 2.2) since it depends on *sums* of the off-diagonal elements. The sum of the $p = 2$ terms, however, is real and finite and so does contribute resulting in a π -periodic relative phase distribution. Continuing to higher orders, we find that all of the odd- p terms sum to zero, and so only the even- p sums contribute to the relative phase distribution. In particular, the $p = 4$ terms, lead to a $\pi/2$ -periodic contribution which can dominate the phase distribution when the π -periodic terms vanish.

B.2 Low Occupation-Number Regime

This calculation can be simplified and solved analytically in the limit of very low phonon numbers. We proceed by assuming only the lowest three phonon states are appreciably occupied, i.e. $P_{n>2} = 0$, and hence truncate the state space to include only $|0\rangle$, $|1\rangle$, and $|2\rangle$. Due to the size of the Hilbert space, only a single term contributes to the relative phase distribution, $P(\phi) = \frac{1}{2\pi} + \frac{1}{\pi} \text{Re} \left[e^{2i\phi} \rho_{0,0}^{(2)} \right]$. In the steady state, Eq. B.1 with $p = 2$ leads to

$$\rho_{0,0}^{(2)} = \frac{-iJ\sqrt{2}}{\kappa_1 + 7\kappa_2} \rho_{1,0}^{(1)}, \quad (\text{B.7})$$

using the relation $\rho_{m,n}^{(1)} = -\rho_{n,m}^{(1)}$. Equation B.1 with $p = 1$ gives

$$\rho_{1,0}^{(1)} = \frac{iJ\sqrt{2}(P_1^2 - P_0P_2)}{2\kappa_1 + 13\kappa_2}. \quad (\text{B.8})$$

This results in the relative phase distribution

$$P(\phi) = \frac{1}{2\pi} + \frac{2J^2(P_1^2 - P_0P_2) \cos 2\phi}{\pi(\kappa_1 + 7\kappa_2)(2\kappa_1 + 13\kappa_2)}. \quad (\text{B.9})$$

This is a π -periodic distribution with the position of the peaks determined by the steady state of the uncoupled oscillators. The two-phonon driving in our model ensures $P_2P_0 > P_1^2$, which leads to peaks at $\frac{\pi}{2}$ and $\frac{3\pi}{2}$.

Appendix C

Phase diffusion of a 321 oscillator

In this Appendix, we return to the case of a single oscillator and obtain an estimate for the phase diffusion rate in the semiclassical limit where phonon numbers are large. The strength of synchronisation of limit-cycles was shown to increase with phonon number in Sec. 2.2.2 for the QvdP oscillator. To study how the phase of our 321 oscillator diffuses with time, we again consider the single oscillator phase distribution with Eq. 2.19 and quantify the amount of phase coherence with $\Phi^{(k)}$ (Eq. 2.20) and, this time, scale our master equation

$$\mathcal{L}(\cdot) = \mathcal{D}\left[(\hat{a}^\dagger)^2\right](\cdot) + \gamma\mathcal{D}[\hat{a}](\cdot) + \Gamma\mathcal{D}[\hat{a}^3](\cdot), \quad (\text{C.1})$$

with $\gamma = \kappa_1/\kappa_2$ and $\Gamma = \kappa_3/\kappa_2$. It is important to note that we scale time with the κ_2 , the two-phonon gain rate (in the QvdP oscillator, κ_2 is the two-phonon *loss* rate).

Written in the Fock basis,

$$\dot{\rho}_n^{(k)} = -G_n^{(k)} \rho_n^{(k)} + A_{n+1}^{(k)} \rho_{n+1}^{(k)} + B_{n-2}^{(k)} \rho_{n-2}^{(k)} + C_{n+3}^{(k)} \rho_{n+3}^{(k)} \quad (\text{C.2})$$

$$G_n^{(k)} = \frac{1}{2} \left\{ (n+k+1)(n+k+2) + (n+1)(n+2) + \gamma(2n+k) \right. \\ \left. + \Gamma[(n+k)(n+k-1)(n+k-2) + n(n-1)(n-2)] \right\} \quad (\text{C.3})$$

$$A_n^{(k)} = \gamma \sqrt{n(n+k)} \quad (\text{C.4})$$

$$B_n^{(k)} = \sqrt{(n+1)(n+2)(n+k+1)(n+k+2)} \quad (\text{C.5})$$

$$C_n^{(k)} = \Gamma \sqrt{n(n-1)(n-2)(n+k)(n+k-1)(n+k-2)}. \quad (\text{C.6})$$

From Eq. C.2, it is trivial to show that

$$\dot{\Phi}^{(k)} = \sum_{n=0}^{\infty} \left(-G_n^{(k)} + A_n^{(k)} + B_n^{(k)} + C_n^{(k)} \right) \Phi^{(k)}. \quad (\text{C.7})$$

We can obtain a simple approximate description in the semiclassical limit, $\gamma = \kappa_1/\kappa_2 \ll 1$ and $\Gamma = \kappa_3/\kappa_2 \ll 1$, where the density matrix is tightly peaked around a large average phonon occupation number $\langle n \rangle \gg 1$ [25, 105]. We expand the square-roots appearing in Eqs. C.4-C.6, treating $\langle n \rangle^{-1}$ together with Γ and γ

as small quantities [25, 103, 105] to find

$$G_n^{(k)} = \frac{5 \langle n \rangle^2}{3} + (\gamma + 2k + 1) \langle n \rangle + \left(\frac{10}{3} + \frac{3k^2}{2} + \frac{\gamma k}{2} - \frac{k}{2} \right) + \left(\frac{k^3}{3} - k^2 + \frac{2k}{3} \right) \frac{1}{\langle n \rangle} \quad (\text{C.8})$$

$$A_n^{(k)} = \gamma \left[\langle n \rangle + \frac{k}{2} - \frac{k^2}{8 \langle n \rangle} + \frac{k^3}{16 \langle n \rangle^2} + \mathcal{O}(\langle n \rangle^{-3}) \right] \quad (\text{C.9})$$

$$B_n^{(k)} = \left[\langle n \rangle^2 + (k + 3) \langle n \rangle + \left(\frac{3k}{2} + 2 \right) - \frac{k^2}{8 \langle n \rangle^2} + \mathcal{O}(\langle n \rangle^{-3}) \right] \quad (\text{C.10})$$

$$C_n^{(k)} = \Gamma \left[\frac{2 \langle n \rangle^2}{3} + (k - 2) \langle n \rangle + \left(\frac{k^2}{4} - 2k + \frac{4}{3} \right) + \left(\frac{2k}{3} - \frac{k^2}{4} - \frac{k^3}{24} \right) + \mathcal{O}(\langle n \rangle^{-3}) \right]. \quad (\text{C.11})$$

This leads to the simplified equation for the 321 oscillator

$$\dot{\Phi}^{(k)} = \kappa_2 \left[-\frac{5}{4} k^2 + \mathcal{O}(\langle n \rangle^{-1}, \Gamma, \gamma) \right] \Phi^{(k)}. \quad (\text{C.12})$$

Hence, to leading order, the relaxation timescale for the k -th component, $\Phi^{(k)}$, is simply proportional to κ_2^{-1} , $\tau_k^{LC} \kappa_2 \approx \frac{4}{5k^2}$. The slowest timescales τ_k associated with the matrices $\mathcal{M}^{(k)}$ in Eq. 4.2 are shown to plateau in the limit of $\kappa_1/\kappa_2 \ll 1$ and $\kappa_3/\kappa_2 \ll 1$ in Fig. 4.4a. Numerically, we find $\tau_1 \kappa_2 \approx 0.8$ and $\tau_2 \kappa_2 \approx 0.2$ in this regime, matching up very well with τ_1^{LC} and τ_2^{LC} , respectively. Finally, using the definition Eq. 2.19 and Eq. C.12, we see that within this approximation the phase distribution obeys a diffusion equation [25, 103]

$$\dot{P}(\phi) = \frac{5\kappa_2}{4} \frac{\partial^2 P(\phi)}{\partial \phi^2}. \quad (\text{C.13})$$

Larger phonon numbers $\langle n \rangle$, from a larger drive strength κ_2 , results in faster phase diffusion and therefore a weakening of synchronisation. This is very different to

the QvdP oscillator (in Sec. 2.2.2) or the laser [105], where larger phonon/photon numbers lead to weaker phase diffusion and hence stronger synchronisation.

Appendix D

Analytic form of spin-1 relative phase distribution

In this appendix, we derive the analytical form of the relative phase distribution of two spin-1 oscillators in Eq. 5.13 from the two-spin Husimi-Q function in Eq. 5.10. First, we write out a simplified form for the spin coherent state

$$|\theta_j, \varphi_j\rangle = A_j e^{-i\varphi_j} |+\rangle + B_j |0\rangle + C_j e^{i\varphi_j} |-\rangle, \quad (\text{D.1})$$

where A_j , B_j , and C_j follow from Eq. 5.1 with $\theta \rightarrow \theta_j$. Explicitly writing the two-spin coherent state, $|\theta_1, \theta_2, \varphi_1, \varphi_2\rangle = |\theta_1, \varphi_1\rangle \otimes |\theta_2, \varphi_2\rangle$ with the change of variables $\varphi_1 = \phi + \varphi_2$ yields

$$\begin{aligned} |\theta_1, \theta_2, \phi + \varphi_2, \varphi_2\rangle = & A_1 A_2 e^{-i\phi} e^{-2i\varphi_2} |++\rangle + A_1 B_2 e^{-i\phi} e^{-i\varphi_2} |+0\rangle + A_1 C_2 e^{-i\phi} |+-\rangle \\ & + B_1 A_2 e^{-i\varphi_2} |0+\rangle + B_1 B_2 |00\rangle + B_1 C_2 e^{i\varphi_2} |0-\rangle \\ & + C_1 A_2 e^{i\phi} |-\rangle + C_1 B_2 e^{i\phi} e^{i\varphi_2} | -0\rangle + C_1 C_2 e^{i\phi} e^{2i\varphi_2} |--\rangle. \end{aligned} \quad (\text{D.2})$$

To derive the relative phase distribution in Eq. 5.13, it is easiest to carry out the φ_2 integral first. This leaves only terms that are independent of φ_2 , since

$$\int_0^{2\pi} d\varphi_2 e^{in\varphi_2} = \begin{cases} 2\pi, & \text{if } n = 0 \\ 0, & \text{otherwise,} \end{cases} \quad (\text{D.3})$$

which reduces the number of terms significantly. The integrals over both θ_1 and θ_2 are trivial, and result in three sets of terms: the probabilities on the diagonal, the $e^{\pm i\phi}$ terms, and the $e^{\pm 2i\phi}$ terms. The probabilities sum to unity and cancel with the $-\frac{1}{2\pi}$ in Eq. 5.13. The ϕ dependent terms produce the relative phase distribution

$$P(\phi) = \pi \left(\frac{3}{16} \right)^2 \left(\langle -0 | \rho | -+ \rangle + \langle 0- | \rho | -0 \rangle + \langle +0 | \rho | 0+ \rangle + \langle +- | \rho | 00 \rangle \right) e^{i\phi} \\ + \frac{1}{8\pi} \langle +- | \rho | -+ \rangle e^{2i\phi} + \text{c.c.} \quad (\text{D.4})$$

where c.c. is the complex conjugate. This can then be rewritten in terms of the spin-1 operators which recovers Eq. 5.13.

Bibliography

- [1] Acebrón J.A., Bonilla L.L., Vicente C.J. et al., 2005. *The Kuramoto model: A simple paradigm for synchronization phenomena*. Reviews of Modern Physics, 77, 1, 137–185. ISSN 00346861.
- [2] Agarwal G.S., Chaturvedi S., Tara K. et al., 1992. *Classical phase changes in nonlinear processes and their quantum counterparts*. Physical Review A, 45, 7, 4904–4910. ISSN 10502947.
- [3] Ameri V., Eghbali-Arani M., Mari A. et al., 2015. *Mutual information as an order parameter for quantum synchronization*. Physical Review A - Atomic, Molecular, and Optical Physics, 91, 1, 012301. ISSN 10941622.
- [4] Appleton E. & van der Pol B., 1921. *XXV. On the form of free triode vibrations*. The London, Edinburgh, and Dublin Philosophical Magazine and Journal of Science, 42, 248, 201–220. ISSN 1941-5982.
- [5] Arenas A., Díaz-Guilera A., Kurths J. et al., 2008. *Synchronization in complex networks*. Physics Reports, 469, 3, 93–153. ISSN 03701573.
- [6] Arnold V.I., 1988. *Geometrical Methods in the Theory of Ordinary Differential Equations*. Springer Berlin Heidelberg, Berlin, Heidelberg. ISBN 978-3-540-78038-0.
- [7] Arrechi F.T., 1972. *Phenomena at the Boundary of Two Phases*. IEEE Journal of Quantum Electronics, 8, 6, 570. ISSN 15581713.
- [8] Balanov A., 2009. *Synchronization : from simple to complex*. Springer, Berlin. ISBN 9783540721277 3540721274.
- [9] Barak R. & Ben-Aryeh Y., 2005. *Non-orthogonal positive operator valued measure phase distributions of one- and two-mode electromagnetic fields*. Journal of Optics B: Quantum and Semiclassical Optics, 7, 5, 123–134. ISSN

14644266.

- [10] Barnett S.M. & Pegg D.T., 1986. *Phase in quantum optics*. Journal of Physics A: Mathematical and General, 19, 18, 3849–3862. ISSN 0305-4470.
- [11] Barnett S.M. & Pegg D.T., 1990. *Quantum theory of optical phase correlations*. Physical Review A, 42, 11, 6713–6720. ISSN 10502947.
- [12] Blasius B., Huppert A. & Stone L., 1999. *Complex dynamics and phase synchronization in spatially extended ecological systems*. Nature, 399, 6734, 354–359. ISSN 00280836.
- [13] Bose, 1924. *Plancks Gesetz und Lichtquantenhypothese*. Zeitschrift für Physik, 26, 1, 178–181. ISSN 1434-6001.
- [14] Braunstein L.S. & Van Loock P., 2005. *Quantum information with continuous variables*. Reviews of Modern Physics, 77, 2, 513–577. ISSN 00346861.
- [15] Buck J., 1988. *Synchronous rhythmic flashing of fireflies. II*. Quarterly Review of Biology, 63, 3, 265–289. ISSN 00335770.
- [16] Buck J. & Buck E., 1976. *Synchronous fireflies*. Scientific American, 234, 5, 74–79, 82. ISSN 00368733.
- [17] Carmichael H.J., 1999. *Statistical Methods in Quantum Optics 1*. Springer Berlin Heidelberg, Berlin, Heidelberg. ISBN 978-3-642-08133-0.
- [18] Chagnac-Amitai Y. & Connors B.W., 1989. *Horizontal spread of synchronized activity in neocortex and its control by GABA-mediated inhibition*. Journal of Neurophysiology, 61, 4, 747–758. ISSN 00223077.
- [19] Chagnac-Amitai Y. & Connors B.W., 1989. *Synchronized excitation and inhibition driven by intrinsically bursting neurons in neocortex*. Journal of Neurophysiology, 62, 5, 1149–1162. ISSN 00223077.
- [20] Chu Y., Kharel P., Yoon T. et al., 2018. *Creation and control of multiphonon Fock states in a bulk acoustic-wave resonator*. Nature, 563, 7733, 666–670. ISSN 14764687.
- [21] Cirac J.I., Blatt R., Zoller P. et al., 1992. *Laser cooling of trapped ions in a standing wave*. Physical Review A, 46, 5, 2668–2681. ISSN 10502947.

- [22] Cohen I. & Retzker A., 2014. *Proposal for Verification of the Haldane Phase Using Trapped Ions*. Physical Review Letters, 112, 4, 040503. ISSN 0031-9007.
- [23] Cresser J.D., Louisell W.H., Meystre P. et al., 1982. *Quantum noise in ring-laser gyros. I. Theoretical formulation of problem*. Physical Review A, 25, 4, 2214–2225. ISSN 10502947.
- [24] Cross M.C., Zumdieck A., Lifshitz R. et al., 2004. *Synchronization by Non-linear Frequency Pulling*. Physical Review Letters, 93, 22, 224101. ISSN 0031-9007.
- [25] Davis-Tilley C. & Armour A.D., 2016. *Synchronization of micromasers*. Physical Review A, 94, 6, 063819. ISSN 24699934.
- [26] DeLuca J., 1993. *Predicting Neurobehavioral Patterns Following Anterior Communicating Artery Aneurysm*. Cortex, 29, 4, 639–647. ISSN 00109452.
- [27] DeVries P.L. & Hamill P., 1995. *A First Course in Computational Physics*. American Journal of Physics, 63, 3, 283–285. ISSN 0002-9505.
- [28] Diamant N.E. & Bortoff A., 1969. *Nature of the intestinal low-wave frequency gradient*. The American journal of physiology, 216, 2, 301–307. ISSN 00029513.
- [29] Dirac P.a.M., 1927. *The quantum theory of the emission and absorption of radiation*. Proceedings of the Royal Society of London. Series A, Containing Papers of a Mathematical and Physical Character, 114, 767, 243–265. ISSN 0950-1207.
- [30] Dykman M., 2012. *Fluctuating Nonlinear Oscillators*, volume 9780199691. Oxford University Press. ISBN 9780199691388.
- [31] Dykman M.I., Bruder C., Lörch N. et al., 2018. *Interaction-induced time-symmetry breaking in driven quantum oscillators*. Physical Review B, 98, 19, 195444. ISSN 2469-9950.
- [32] Ferrari F., Viana R., Lopes S. et al., 2015. *Phase synchronization of coupled bursting neurons and the generalized Kuramoto model*. Neural Networks, 66, 107–118. ISSN 08936080.

- [33] Fukuda H., Nakamichi N., Hisatsune M. et al., 2007. *Synchronization of plant circadian oscillators with a phase delay effect of the vein network*. Physical Review Letters. ISSN 00319007.
- [34] Galve F., Luca Giorgi G. & Zambrini R., 2017. *Quantum Correlations and Synchronization Measures*. Springer, Cham.
- [35] Gardiner C.W. & Zoller P., 2000. *Quantum noise : a handbook of Markovian and non-Markovian quantum stochastic methods with applications to quantum optics*. Springer. ISBN 3540665714 (hardcover alk. paper)\r0172-7389.
- [36] Garlaschelli D., Di Matteo T., Aste T. et al., 2007. *Interplay between topology and dynamics in the World Trade Web*. The European Physical Journal B, 57, 2, 159–164. ISSN 1434-6028.
- [37] Genway S., Li W., Ates C. et al., 2014. *Generalized Dicke nonequilibrium dynamics in trapped ions*. Physical Review Letters, 112, 2, 023603. ISSN 00319007.
- [38] Gerry C. & Knight P., 2004. *Introductory Quantum Optics*. Cambridge University Press. ISBN 9780521527354.
- [39] Gilles L., Garraway B.M. & Knight P.L., 1994. *Generation of nonclassical light by dissipative two-photon processes*. Physical Review A, 49, 4, 2785–2799. ISSN 1050-2947.
- [40] Giorgi G.L., Galve F., Manzano G. et al., 2012. *Quantum correlations and mutual synchronization*. Physical Review A - Atomic, Molecular, and Optical Physics, 85, 5, 052101. ISSN 10502947.
- [41] Glauber R.J., 1963. *Coherent and incoherent states of the radiation field*. Physical Review, 131, 6, 2766–2788. ISSN 0031899X.
- [42] Goldberg D.M. & Gott J.R., 2007. *Flexion and Skewness in Map Projections of the Earth*. Cartographica: The International Journal for Geographic Information and Geovisualization, 42, 4, 297–318. ISSN 0317-7173.
- [43] Gorini V., 1976. *Completely positive dynamical semigroups of N-level systems*. Journal of Mathematical Physics, 17, 5, 821. ISSN 00222488.
- [44] Gray C.M. & Di Prisco G.V., 1997. *Stimulus-dependent neuronal oscilla-*

- tions and local synchronization in striate cortex of the alert cat.* Journal of Neuroscience, 17, 9, 3239–3253. ISSN 02706474.
- [45] Haroche S. & Raimond J.M., 2006. *Exploring the Quantum.* Oxford University Press. ISBN 9780198509141.
- [46] Heisenberg W., 1927. *Über den anschaulichen Inhalt der quantentheoretischen Kinematik und Mechanik.* Zeitschrift für Physik, 43, 3-4, 172–198. ISSN 14346001.
- [47] Heisenberg W., 1931. *Die Rolle der Unbestimmtheitsrelationen in der modernen Physik.* Monatshefte für Mathematik und Physik, 38, 1, 365–372. ISSN 00269255.
- [48] Hoppensteadt F.C. & Izhikevich E.M., 1997. *Weakly Connected Neural Networks*, volume 126 of *Applied Mathematical Sciences.* Springer New York, New York, NY. ISBN 978-1-4612-7302-8.
- [49] Hush M.R., Li W., Genway S. et al., 2015. *Spin correlations as a probe of quantum synchronization in trapped-ion phonon lasers.* Physical Review A - Atomic, Molecular, and Optical Physics, 91, 6, 061401. ISSN 1050-2947.
- [50] Husimi K., 1940. *Some formal properties of the density matrix.* Proc. Phys. Math. Soc. Jpn., 22, 4, 264.
- [51] Huygens C., 1888. *Oeuvres complètes de Christiaan Huygens. Publiées par la Société hollandaise des sciences.*, volume t.4. M. Nijhoff, La Haye.
- [52] James D., 1998. *Quantum dynamics of cold trapped ions with application to quantum computation.* Applied Physics B: Lasers and Optics, 66, 2, 181–190. ISSN 0946-2171.
- [53] Jessop M.R., Li W. & Armour A.D., 2020. *Phase synchronization in coupled bistable oscillators.* Physical Review Research, 2, 1, 013233. ISSN 2643-1564.
- [54] Jozsa R., 1994. *Fidelity for mixed quantum states.* Journal of Modern Optics, 41, 12, 2315–2323. ISSN 13623044.
- [55] Knünz S., Herrmann M., Batteiger V. et al., 2010. *Injection locking of a trapped-ion phonon laser.* Physical Review Letters, 105, 1. ISSN 00319007.

- [56] Koppenhöfer M., Bruder C. & Roulet A., 2020. *Quantum synchronization on the IBM Q system*. Physical Review Research, 2, 2, 023026. ISSN 2643-1564.
- [57] Koppenhöfer M. & Roulet A., 2019. *Optimal synchronization deep in the quantum regime: Resource and fundamental limit*. Physical Review A, 99, 4, 043804. ISSN 2469-9926.
- [58] Kuznetsov A.P., Stankevich N.V. & Turukina L.V., 2009. *Coupled van der Pol-Duffing oscillators: Phase dynamics and structure of synchronization tongues*. Physica D: Nonlinear Phenomena, 238, 14, 1203–1215. ISSN 01672789.
- [59] Lading B., Mosekilde E., Yanchuk S. et al., 2000. *Chaotic Synchronization between Coupled Pancreatic β -Cells*. Progress of Theoretical Physics Supplement, 139, 139, 164–177. ISSN 0375-9687.
- [60] Lee T.E., Chan C.K. & Wang S., 2014. *Entanglement tongue and quantum synchronization of disordered oscillators*. Physical Review E, 89, 2, 022913. ISSN 1539-3755.
- [61] Lee T.E. & Sadeghpour H.R., 2013. *Quantum synchronization of quantum van der Pol oscillators with trapped Ions*. Physical Review Letters, 111, 23, 234101. ISSN 00319007.
- [62] Leibfried D., Meekhof D.M., King B.E. et al., 1996. *Experimental Determination of the Motional Quantum State of a Trapped Atom*. Physical Review Letters, 77, 21, 4281–4285. ISSN 0031-9007.
- [63] Li W., Li C. & Song H., 2016. *Quantum synchronization in an optomechanical system based on Lyapunov control*. Physical Review E, 93, 6, 062221. ISSN 2470-0045.
- [64] Lindblad G., 1976. *On the generators of quantum dynamical semigroups*. Communications in Mathematical Physics, 48, 2, 119–130. ISSN 00103616.
- [65] Lörch N., Amitai E., Nunnenkamp A. et al., 2016. *Genuine Quantum Signatures in Synchronization of Anharmonic Self-Oscillators*. Physical Review Letters, 117, 7, 073601. ISSN 10797114.
- [66] Lörch N., Nigg S.E., Nunnenkamp A. et al., 2017. *Quantum Synchroniza-*

- tion Blockade: Energy Quantization Hinders Synchronization of Identical Oscillators*. Physical Review Letters, 118, 24, 243602. ISSN 10797114.
- [67] Lörch N., Zhang Y., Bruder C. et al., 2019. *Quantum state preparation for coupled period tripling oscillators*. Physical Review Research, 1, 2, 023023. ISSN 2643-1564.
- [68] Ludwig M. & Marquardt F., 2013. *Quantum Many-Body Dynamics in Optomechanical Arrays*. Physical Review Letters, 111, 7, 073603. ISSN 0031-9007.
- [69] Luis A., Sánchez-Soto L.L., Luis et al., 1996. *Probability distributions for the phase difference*. Physical Review A - Atomic, Molecular, and Optical Physics, 53, 1, 495–501. ISSN 1050-2947.
- [70] Macieszczak K., Guţă M., Lesanovsky I. et al., 2016. *Towards a Theory of Metastability in Open Quantum Dynamics*. Physical Review Letters, 116, 24, 240404. ISSN 0031-9007.
- [71] Manneville P., 1990. *Dissipative Structures and Weak Turbulence*. In P. Manneville, editor, *Dissipative Structures and Weak Turbulence*, pages xv – xvii. Elsevier, Boston. ISBN 9780080924458.
- [72] Manzano G., Galve F., Giorgi G.L. et al., 2013. *Synchronization, quantum correlations and entanglement in oscillator networks*. Scientific Reports, 3, 1, 1439. ISSN 20452322.
- [73] Mari A., Farace A., Didier N. et al., 2013. *Measures of quantum synchronization in continuous variable systems*. Physical Review Letters, 111, 10, 103605. ISSN 00319007.
- [74] Michaels D.C., Matyas E.P. & Jalife J., 1987. *Mechanisms of sinoatrial pacemaker synchronization: a new hypothesis*. Circulation Research, 61, 5, 704–714. ISSN 0009-7330.
- [75] Navarrete-Benlloch C., 2015. *Open systems dynamics: Simulating master equations in the computer*. arXiv preprint arXiv: 1504.05266v2, pages 1–18.
- [76] Nielsen J.R. & Kittel C., 2006. *Elementary Statistical Physics*. The American Mathematical Monthly, 66, 10, 928. ISSN 00029890.

- [77] Nieto M.M., 1993. *Quantum phase and quantum phase operators: some physics and some history*. Physica Scripta, T48, 5–12. ISSN 0031-8949.
- [78] Nigg S.E., 2018. *Observing quantum synchronization blockade in circuit quantum electrodynamics*. Physical Review A, 97, 1. ISSN 24699934.
- [79] Nirmal M., Dabbousi B.O., Bawendi M.G. et al., 1996. *Fluorescence intermittency in single cadmium selenide nanocrystals*. Nature, 383, 6603, 802–804. ISSN 00280836.
- [80] Ong F.R., Boissonneault M., Mallet F. et al., 2011. *Circuit QED with a nonlinear resonator: Ac-stark shift and dephasing*. Physical Review Letters, 106, 16. ISSN 00319007.
- [81] Ong F.R., Boissonneault M., Mallet F. et al., 2013. *Quantum Heating of a Nonlinear Resonator Probed by a Superconducting Qubit*. Physical Review Letters, 110, 4, 047001. ISSN 0031-9007.
- [82] Onnela J.P., Chakraborti A., Kaski K. et al., 2003. *Dynamics of market correlations: Taxonomy and portfolio analysis*. Physical Review E, 68, 5, 056110. ISSN 1063-651X.
- [83] Osipov G.V., Kurths J. & Zhou C., 2009. *Complex Systems and Self-organization Modelling*. Understanding Complex Systems. Springer Berlin Heidelberg, Berlin, Heidelberg. ISBN 978-3-540-88072-1.
- [84] Parra-López Á. & Bergli J., 2020. *Synchronization in two-level quantum systems*. Physical Review A, 101, 6, 062104. ISSN 2469-9926.
- [85] Pegg D.T. & Barnett S.M., 1989. *Phase properties of the quantized single-mode electromagnetic field*. Physical Review A, 39, 4, 1665–1675. ISSN 0556-2791.
- [86] Pikovsky A., Rosenblum M. & Kurths J., 2003. *Synchronization: A Universal Concept in Nonlinear Sciences*. Cambridge University Press, Cambridge. ISBN 978-0521533522.
- [87] Pitt J.C., 2009. *Paolo Palmieri. Reenacting Galileo's Experiments: Rediscovering the Techniques of Seventeenth-Century Science . 304 pp., apps., bibl., indexes. Lewiston, N.Y.: Edwin Mellen Press, 2008*. Isis, 100, 3, 661–662. ISSN 0021-1753.

- [88] Planck M. & Masius M., 1914. *The Theory of Heat Radiation*. Blakiston.
- [89] Plenio M.B. & Knight P.L., 1998. *The quantum-jump approach to dissipative dynamics in quantum optics*. *Reviews of Modern Physics*, 70, 1, 101–144. ISSN 0034-6861.
- [90] Pluchino A., Latora V. & Rapisarda A., 2004. *Changing Opinions in a Changing World: a New Perspective in Sociophysics*. *International Journal of Modern Physics C*, 16, 04, 515–531. ISSN 0129-1831.
- [91] Postnov D.E., Balanov A.G., Janson N.B. et al., 1999. *Homoclinic bifurcation as a mechanism of chaotic phase synchronization*. *Physical Review Letters*, 83, 10, 1942–1945. ISSN 10797114.
- [92] Puri S., Andersen C.K., Grimsmo A.L. et al., 2017. *Quantum annealing with all-to-all connected nonlinear oscillators*. *Nature Communications*, 8, 1, 15785. ISSN 2041-1723.
- [93] Radcliffe J.M., 1971. *Some properties of coherent spin states*. *Journal of Physics A: General Physics*, 4, 3, 313–323. ISSN 0022-3689.
- [94] Rayleigh J.W.S., 1896. *The Theory of Sound Vol. II*. Macmillan.
- [95] Repp B.H. & Su Y.H., 2013. *Sensorimotor synchronization: A review of recent research (2006–2012)*. *Psychonomic Bulletin & Review*, 20, 3, 403–452. ISSN 1069-9384.
- [96] Restrepo J.G., Ott E. & Hunt B.R., 2005. *Onset of synchronization in large networks of coupled oscillators*. *Physical Review E*, 71, 3, 036151. ISSN 1539-3755.
- [97] Risken H., Savage C., Haake F. et al., 1987. *Quantum tunneling in dispersive optical bistability*. *Physical Review A*, 35, 4, 1729–1739. ISSN 0556-2791.
- [98] Rodrigues D.A., Imbers J. & Armour A.D., 2007. *Quantum Dynamics of a Resonator Driven by a Superconducting Single-Electron Transistor: A Solid-State Analogue of the Micromaser*. *Physical Review Letters*, 98, 6, 067204. ISSN 0031-9007.
- [99] Rota R., Minganti F., Ciuti C. et al., 2019. *Quantum Critical Regime in a Quadratically Driven Nonlinear Photonic Lattice*. *Physical Review Letters*,

- 122, 11, 110405. ISSN 0031-9007.
- [100] Roulet A. & Bruder C., 2018. *Quantum Synchronization and Entanglement Generation*. Physical Review Letters, 121, 6, 063601. ISSN 0031-9007.
- [101] Roulet A. & Bruder C., 2018. *Synchronizing the Smallest Possible System*. Physical Review Letters, 121, 5, 053601. ISSN 10797114.
- [102] Scarlatella O., Clerk A.A. & Schiro M., 2019. *Spectral functions and negative density of states of a driven-dissipative nonlinear quantum resonator*. New Journal of Physics, 21, 4, 043040. ISSN 1367-2630.
- [103] Schieve W.C. & McGowan R.R., 1993. *Phase distribution and linewidth in the micromaser*. Physical Review A, 48, 3, 2315–2323. ISSN 10502947.
- [104] Schuster H.G. & Wagner P., 1989. *Mutual Entrainment of Two Limit Cycle Oscillators with Time Delayed Coupling*. Progress of Theoretical Physics, 81, 5, 939–945. ISSN 0033-068X.
- [105] Scully M.O. & Zubairy M.S., 1997. *Quantum Optics*. Cambridge University Press, Cambridge. ISBN 9780521435956.
- [106] Senko C., Richerme P., Smith J. et al., 2015. *Realization of a quantum integer-spin chain with controllable interactions*. Physical Review X, 5, 2. ISSN 21603308.
- [107] Sherman A., Rinzel J. & Keizer J., 1988. *Emergence of organized bursting in clusters of pancreatic beta-cells by channel sharing*. Biophysical Journal, 54, 3, 411–425. ISSN 00063495.
- [108] Singer W. & Gray C.M., 1995. *Visual Feature Integration and the Temporal Correlation Hypothesis*. Annual Review of Neuroscience, 18, 1, 555–586. ISSN 0147-006X.
- [109] Stark A., Aharon N., Huck A. et al., 2018. *Clock transition by continuous dynamical decoupling of a three-level system*. Scientific Reports, 8, 1, 14807. ISSN 2045-2322.
- [110] Susskind L. & Glogower J., 1964. *Quantum mechanical phase and time operator*. Physics Physique Fizika, 1, 1, 49–61. ISSN 0554-128X.

- [111] Tass P.A., 1999. *Phase Resetting in Medicine and Biology*, volume 49 of *Springer Series in Synergetics*. Springer Berlin Heidelberg, Berlin, Heidelberg. ISBN 978-3-540-38159-4.
- [112] Temple G. & Dirac P.A.M., 1935. *The Principles of Quantum Mechanics*. *The Mathematical Gazette*, 19, 235, 301. ISSN 00255572.
- [113] Torre V., 1976. *A theory of synchronization of heart pace-maker cells*. *Journal of Theoretical Biology*, 61, 1, 55–71. ISSN 10958541.
- [114] Vahala K., Herrmann M., Knünz S. et al., 2009. *A phonon laser*. *Nature Physics*, 5, 9, 682–686. ISSN 17452481.
- [115] van der Pol B., 1926. *LXXXVIII. On “relaxation-oscillations”*. *The London, Edinburgh, and Dublin Philosophical Magazine and Journal of Science*, 2, 11, 978–992. ISSN 1941-5982.
- [116] Vidal G. & Werner R.F., 2002. *Computable measure of entanglement*. *Physical Review A*, 65, 3, 032314. ISSN 1050-2947.
- [117] Walker T.J., 1969. *Acoustic Synchrony: Two Mechanisms in the Snowy Tree Cricket*. *Science*, 166, 3907, 891–894. ISSN 0036-8075.
- [118] Walter S., Nunnenkamp A. & Bruder C., 2014. *Quantum Synchronization of a Driven Self-Sustained Oscillator*. *Physical Review Letters*, 112, 9, 094102. ISSN 10797114.
- [119] Wang Z., Pechal M., Wollack E.A. et al., 2019. *Quantum Dynamics of a Few-Photon Parametric Oscillator*. *Physical Review X*, 9, 2, 021049. ISSN 2160-3308.
- [120] Weiss T., Kronwald A. & Marquardt F., 2016. *Noise-induced transitions in optomechanical synchronization*. *New Journal of Physics*, 18, 1, 013043. ISSN 13672630.
- [121] Wineland D., Monroe C., Itano W. et al., 1998. *Experimental issues in coherent quantum-state manipulation of trapped atomic ions*. *Journal of Research of the National Institute of Standards and Technology*, 103, 3, 259. ISSN 1044677X.
- [122] Xu M., Tieri D.A., Fine E.C. et al., 2014. *Synchronization of Two Ensembles*

- of Atoms*. Physical Review Letters, 113, 15, 154101. ISSN 0031-9007.
- [123] Yoder J.G., 2005. *Christiaan Huygens, book on the pendulum clock (1673)*. In *Landmark Writings in Western Mathematics 1640-1940*, pages 33–45. Elsevier. ISBN 9780444508713.
- [124] Zhang Y., Gosner J., Girvin S.M. et al., 2017. *Time-translation-symmetry breaking in a driven oscillator: From the quantum coherent to the incoherent regime*. Physical Review A, 96, 5, 052124. ISSN 2469-9926.
- [125] Zhirov O.V. & Shepelyansky D.L., 2006. *Quantum synchronization*. The European Physical Journal D, 38, 2, 375–379. ISSN 1434-6060.
- [126] Zhu B., Schachenmayer J., Xu M. et al., 2015. *Synchronization of interacting quantum dipoles*. New Journal of Physics, 17, 8, 083063. ISSN 13672630.